Dissertation presented to the Instituto Tecnológico de Aeronáutica, in partial fulfillment of the requirements for the degree of Master of Science in the Graduate Program of Aeronautical and Mechanical Engineering, Field of Aeronautical Design, Structures and Aerospace Systems.

Lucas Garcia de Sampaio Lobianco

BUCKLING ANALYSIS OF STIFFENED COMPOSITE PANELS WITH CUTOUTS USING THE DISCRETE RITZ METHOD

Dissertation approved in its final version by signatories below:

Maurício Vicente Donadon

Prof. Dr. Maurício Vicente Donadon
Advisor

Campo Montenegro
São José dos Campos, SP - Brazil
2024

BIBLIOGRAPHIC REFERENCE

LOBIANCO, Lucas Garcia de Sampaio. **Buckling analysis of stiffened composite panels with cutouts using the discrete Ritz method**. 2024. 129f. Dissertation of Master of Science – Instituto Tecnológico de Aeronáutica, São José dos Campos.

CESSION OF RIGHTS

BUCKLING ANALYSIS OF STIFFENED COMPOSITE PANELS WITH CUTOUTS USING THE DISCRETE RITZ METHOD

Lucas Garcia de Sampaio Lobianco

Thesis Committee Composition:

Prof. Dr.	Mariano Andrés Arbelo	President	-	ITA
Prof. Dr.	Maurício Vicente Donadon	Advisor	-	ITA
Prof. Dr.	Eliseu Lucena Neto	Internal member	-	ITA
Prof. Dr.	Flaminio Levy Neto	External member	-	UnB

ITA

Dedico este trabalho à minha esposa,
minha eterna fonte de amor e inspiração.

Acknowledgments

Gostaria de expressar minha mais profunda gratidão à minha esposa, cujo papel foi fundamental durante todo o período do meu mestrado. Seu apoio incondicional em todos os momentos, tanto nos previsíveis quanto nos imprevisíveis, foi essencial para a realização deste trabalho. Tenho plena certeza de que todo nosso esforço valerá a pena.

Aos meus pais, agradeço profundamente por todos os ensinamentos e por sempre priorizarem minha educação. Ao meu irmão, minha gratidão por ser meu exemplo na infância e por seu constante apoio. Agradeço também às minhas sobrinhas, que me enchem de esperança em um futuro melhor.

Sou imensamente grato ao meu orientador, Prof. Dr. Maurício Vicente Donadon, por desempenhar seu papel de forma excepcional, com incansável apoio e paciência. Sua orientação foi essencial para a realização deste trabalho, sempre me motivando a dar o meu melhor e proporcionando a liberdade necessária para exercer minha criatividade.

Agradeço sinceramente ao Prof. Dr. Mariano Andrés Arbelo por sua prestatividade e disposição exemplar em esclarecer minhas dúvidas durante as atividades de laboratório e disciplinas da pós-graduação, além de fornecer valiosas dicas para melhorar meu trabalho.

Agradeço aos parceiros do Projeto FINEP SPIRIT FLY pela manufatura e disponibilização do material ensaiado. Também expresso minha gratidão à equipe do Laboratório de Estruturas do ITA, cuja competência e boa vontade foram essenciais para a realização dos experimentos deste trabalho.

Minha gratidão também se estende ao Prof. Dr. Zhao Jing, por sua paciência e dedicação ao esclarecer minhas dúvidas sobre sua metodologia, que desempenhou um papel fundamental neste trabalho.

Ao meu orientador técnico da Marinha do Brasil, Capitão-Tenente (EN) Alexandre Alli Pereira, agradeço pela confiança no meu trabalho e pelos valiosos conselhos.

Por fim, agradeço à Marinha do Brasil e à Força Aérea Brasileira por me proporcionarem a oportunidade de aprimorar minhas competências técnicas.

"Success is the sum of small efforts,
repeated day in and day out."
— Robert Collier

Resumo

A idealização da seção crítica de um componente estrutural de uma aeronave é uma abordagem estratégica na engenharia aeroespacial, equilibrando a necessidade de análise detalhada com as praticidades de projeto e a melhoria do desempenho numérico do modelo. Assim, é possível concentrar esforços nos aspectos mais cruciais do projeto da aeronave, garantindo a segurança, o desempenho e a eficiência do produto final. Nesse contexto, este trabalho apresenta o desenvolvimento de um modelo semianalítico utilizando o software MATLAB® e empregando o Método de Ritz Discreto e o princípio da energia potencial total estacionária para conduzir análises de pré-flambagem e determinar a carga crítica de flambagem de placas com recortes circulares e reforçadores. Uma metodologia é proposta para minimizar o esforço computacional requerido pelo modelo. Além disso, com o uso de polinômios hierárquicos, pode-se simular diversas condições de contorno de borda, com a realização de apenas um *set* de integrações. O modelo desenvolvido é validado através de comparações com a literatura existente, análise de elementos finitos utilizando o software Abaqus® e testes experimentais envolvendo a flambagem de painéis de um estabilizador horizontal de uma aeronave sob a condição de carregamento de cisalhamento puro, utilizando-se uma configuração de teste do tipo *picture frame*, conforme previsto em (SINGER *et al.*, 1998). Os resultados numéricos e experimentais demonstram excelente concordância, indicando a robustez e precisão do modelo. A pesquisa destaca a eficiência do método proposto na redução do custo computacional, mantendo alta precisão, tornando-o uma ferramenta valiosa para analisar o comportamento de flambagem em aplicações de engenharia aeroespacial, naval, mecânica, dentre outras. Os estudos aqui apresentados sugerem que a combinação de polinômios hierárquicos e integração numérica via quadratura de Gauss-Legendre oferece vantagens significativas em termos de eficiência computacional e precisão. Apesar de pequenas discrepâncias observadas nas correlações com resultados experimentais, principalmente devido a variações nas condições de fixação e processos de manufatura do material, o estudo fornece uma estrutura abrangente para futuras pesquisas e implementação prática.

Abstract

The idealization of the critical section of a structural component of an aircraft is a strategic approach in aerospace engineering, balancing the need for detailed analysis, addressing particular issues related to the engineering design and improvement on numerical performance of the model. Thus, it is possible to focus efforts on the most crucial aspects of aircraft design, ensuring safety, performance, and efficiency in the final product. In this context, this work presents the development of a semi-analytical model using MATLAB® software and employing the Discrete Ritz Method and the principle of stationary total potential energy to conduct prebuckling analyses and determine the critical buckling load of plates with circular cutouts and stiffeners. A methodology is proposed to minimize the computational effort required by the model. Additionally, with the use of hierarchical polynomials, various edge boundary conditions can be simulated with only one set of integrations. The developed model is validated through comparisons with existing literature, finite element analysis using Abaqus® software, and experimental tests involving the buckling of panels of an aircraft's horizontal stabilizer under pure shear loading conditions, using a picture frame testing jig, as outlined in (SINGER et al., 1998). The numerical and experimental results demonstrate excellent agreement, indicating the robustness and accuracy of the model. The research highlights the efficiency of the proposed method in reducing computational cost while maintaining high precision, making it a valuable tool for analyzing buckling behavior in aerospace, naval, mechanical engineering applications, among others. The findings presented herein suggest that the combination of hierarchical polynomials and numerical integration via Gauss-Legendre quadrature offers significant advantages in terms of computational efficiency and precision. Despite minor discrepancies observed between experimental and numerical correlations, mainly due to variations in clamping conditions and material manufacturing processes, the study provides a comprehensive framework for future research and practical implementation.

List of Figures

List of Tables

List of Abbreviations and Acronyms

BC	Bending Curvature
CLT	Classical Lamination Theory
DIC	Digital Image Correlation
DRM	Discrete Ritz Method
ITA	Instituto Tecnológico de Aeronáutica
FEM	Finite Element Model
FSDT	First-Order Shear Deformation Theory
MD	Membrane Deformation
SE-FSM	Semi-Energy Finite Strip Method
SG	Strain Gauges
VAT	Variable Angle Tow

List of Symbols

$\mathbf{A}$ Extensional stiffness matrix

A_{st} Cross-sectional area of the stiffener

a Plate length

$\mathbf{B}$ Bending-extension coupling stiffness matrix

b Plate width

$\mathbf{D}$ Bending stiffness matrix

E_1 Elasticity modulus in the 1-direction of the lamina

E_2 Elasticity modulus in the 2-direction of the lamina

E_y^s Effective elasticity modulus of the stiffener in the y-direction

G_{12} Shear modulus in the 1-2 plane of the lamina

G_{13} Shear modulus in the 1-3 plane of the lamina

G_{23} Shear modulus in the 2-3 plane of the lamina

G_{xz}^s Effective shear modulus in the $x - z$ plane of the stiffener

$\mathbf{H}$ Transverse shear stiffness matrix

h Plate thickness

J Saint-Venant torsional constant of the stiffener

$\mathbf{M}$ Vector of moments per unit length on the plate

$\mathbf{N}$ Vector of in-plane forces per unit length on the plate

$\mathbf{S}$ Vector of transverse shear forces per unit length on the plate

u Displacement along x-direction

v Displacement along y-direction

w Displacement along z-direction

ε Normal strain component

γ Shear strain component

Γ Warping torsional constant of the stiffener

$\boldsymbol{\kappa}$ Vector of middle plane curvature

σ Normal stress component

τ Shear stress component

θ Fiber orientation

φ_u Projection of the rotation in the $x - z$ plane

φ_v Projection of the rotation in the $y - z$ plane

Contents

1 Introduction

In engineering design, laminated composite materials have become indispensable, particularly in applications where a balance between lightweight and structural strength is crucial, such as in the aerospace and marine industries. These composites are highly valued for their exceptional specific strength and stiffness, which surpass traditional metallic materials, as documented in the literature (WANG; QIAO, 2021).

To ensure the stability of these composite structures, various modeling techniques have been developed and applied, including numerical, semi-analytical, and analytical solutions. Among these, semi-analytical methods, particularly the Ritz method, have been prominently utilized for buckling analysis due to their efficiency and effectiveness (DHURIA et al., 2024). The Ritz method, developed over a century ago, is a fundamental tool in solid mechanics. It approximates the displacement function through a series of trial functions that satisfy essential boundary conditions (MORENO-GARCÍA et al., 2017). In buckling analysis, this method is distinguished by its ability to select displacement functions that accurately reflect specific edge conditions. However, its application has been somewhat limited to a select range of scenarios due to the unique characteristics of these displacement functions (NI et al., 2005).

The complexities of structural design in aerospace, civil, marine, and mechanical engineering require careful analysis of various factors, including natural frequencies, mode shapes, stresses, moments, and especially critical buckling loads (KUMAR, 2018). To enhance structural efficiency and buckling resistance, thin-walled composite plates often incorporate stiffening elements. These elements are crucial in addressing stability challenges and are widely used in composite stiffened plates. Their design and stiffness parameters significantly influence their buckling behavior, which can manifest in both global and local modes. By strategically allowing the skin or stiffeners to buckle before complete structural failure, engineers can design structures that redistribute stress and maintain load-carrying capacity in the post-buckling phase, an approach extensively used in optimizing lightweight aerospace structures for enhanced post-buckling load-carrying capacity (STAMATELOS et al., 2011).

The influence of different shapes and sizes of cutouts on the buckling behavior of plates

is also significant. Buckling analysis helps in understanding how various geometries affect the critical buckling load and the mode shapes. This understanding is crucial for making well-founded design decisions, ensuring that the cutouts do not significantly compromise the plate's load-carrying capacity.

Moreover, idealizations in aerospace engineering for performing buckling analysis are motivated by several critical factors that enhance the design and optimization process. Many structures are composed of numerous intricate components, making comprehensive analysis challenging. Idealization mitigates this complexity, enabling engineers to focus on critical sections that substantially influence the component's performance. This approach makes the analysis more manageable and comprehensible.

By enhancing our understanding of how stiffeners and cutouts influence structural stability, this work supports the design of more efficient, lightweight, and robust structures. This has significant implications for improving the safety, performance, and cost-effectiveness of engineering applications in aeronautics, naval, mechanical, and other fields.

Buckling analysis can be applied to aircraft wings, submarine control surfaces, ship rudders, among others. An example of an application in the aeronautical field is the evaluation of the dimensions of a stiffener to ensure it compensates for the inclusion of a cutout in a rib of an aircraft's horizontal stabilizer, as represented in Figure 1.1. This analysis is crucial for maintaining structural integrity and performance and will also be thoroughly evaluated throughout this study.
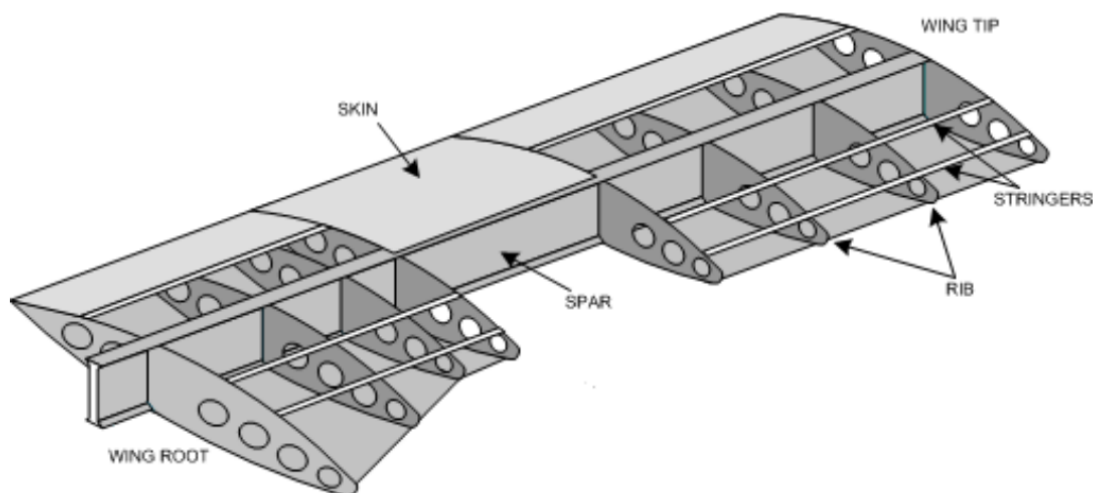
FIGURE 1.1 – Representative figure of the parts of a horizontal stabilizer, including a rib and spar configuration. Source: (HALEY, 2012)

Furthermore, a rib of a horizontal stabilizer, for example, can be idealized by its critical section in an aircraft, as shown in Figure 1.2.
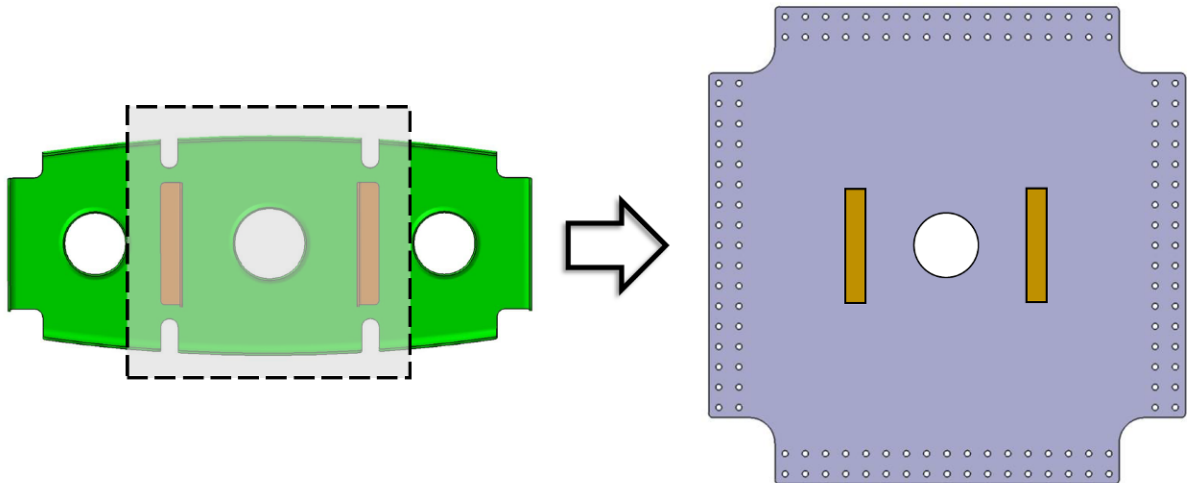
FIGURE 1.2 – Representation of the idealization of a rib contained in a horizontal stabilizer.

Additionally, an experimental buckling analysis under pure shear conditions can be performed using a picture frame testing jig, as illustrated in Figure 1.3. This technique is validated by the equivalence of the force vector applied to the plate and has shown satisfactory results by (SINGER *et al.*, 1998) and (SILVA, 2021).

The plate is clamped along all its edges.
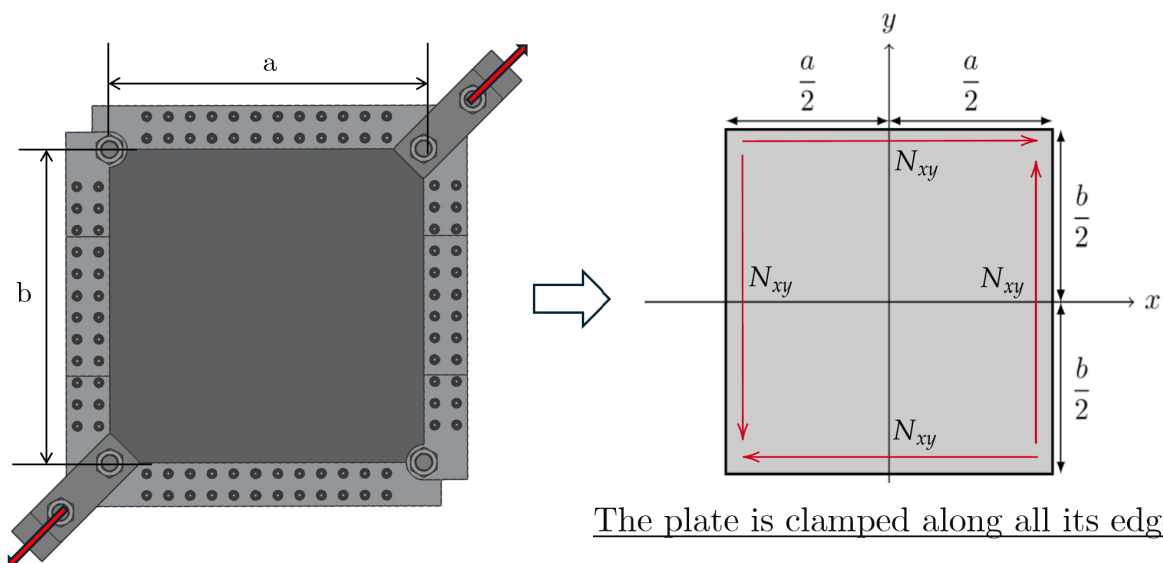
FIGURE 1.3 – Representative figure illustrating the equivalence between pure shear loading and diagonal tensile loading configurations.

1.1 Objectives

In this context, the primary objectives of this research are:

- **Semi-analytical model development**:

- To utilize the Discrete Ritz Method to conduct prebuckling analysis and determine the critical buckling load of a plate with a circular cutout and stiffeners under various loading conditions. This explores the use of the total energy potential principle and hierarchical polynomials, as well as computational integration techniques using the Gauss quadrature method.

- To assess the effectiveness of hierarchical polynomials as trial shape functions for analyzing stiffened plates with cutouts, using the Discrete Ritz Method.

- To verify the implemented semi-analytical model by comparing it with existing literature for plates without cutouts (NARITA, 1990) and for plates with circular cutouts as described in (NIMA; GANESAN, 2021) and (JING; DUAN, 2023), as well as with finite element analysis.

- **Numerical improvement on the simulation performance of the model**:

  - To develop a methodology for applying hierarchical polynomials to minimize the number of simulations required for various edge boundary conditions of a plate.

  - To maximize the use of limited computational resources by calculating critical buckling for lower indices of hierarchical polynomials using the same number of Gauss-Legendre quadrature points, eliminating the need for additional sets of integration and facilitating reliable convergence studies.

  - To improve computational efficiency by implementing methods that significantly reduce computational time and effort through the use of hierarchical polynomials and Gauss-Legendre quadrature for numerical integration.

- **Semi-analytical model validation**:

  - To conduct experimental tests involving three idealized configurations of a rib of a horizontal stabilizer: one considering only the plate, another with the plate with a circular cutout, and another considering a stiffened plate with a cutout.

  - To verify the adherence of the idealized model through the implementation of the semi-analytical model and finite element analysis.

  - To observe the change in behavior of the mode shapes after the inclusion of the cutout and the stiffener.

  - To verify if the buckling load of the stiffened panel with a cutout compensates for the inclusion of the cutout in the plate in the experimental cases performed.

1.2   Dissertation Layout

This dissertation is organized into eight chapters. Chapter 1 provides an introduction and outlines the objectives of the research topic. Chapter 2 offers a literature review concerning buckling studies in laminated panels, including plates, plates with cutouts, and stiffened plates with cutouts. Chapter 3 outlines the development and formulation of the semi-analytical model, employing the Discrete Ritz Method (DRM) and the First-Order Shear Deformation Theory (FSDT). It also covers the use of hierarchical polynomials, the Gauss-quadrature integration method, and the analysis of prebuckling and buckling. Chapter 4 describes the numerical improvements on the simulation performance of the model, including the simulation of various boundary conditions using a single set of integrations and a methodology to address initially unsuccessful numerical integrations, along with other enhancements. Chapter 5 presents the verification and convergence of the proposed model for plates and plates with cutouts. Chapter 6 details the experimental setup and procedures, including the experimental determination of critical buckling. Chapter 7 discusses the results obtained and provides a comprehensive analysis. Finally, Chapter 8 concludes the dissertation with a summary of findings and suggestions for future research.

2 Literature Review

2.1 Buckling Studies in Laminated Panels

In the field of laminated composite materials, the determination of the critical buckling load is essential for ensuring structural stability under various loading conditions. Detailed numerical results for the critical buckling loads of simply supported, rectangular laminated composite plates under five loading scenarios, using the Ritz method with double sine series displacement assumptions, are provided by (NARITA, 1990). Convergence studies and contour plots of buckled mode shapes confirm the accuracy of these findings.

An examination of ten boundary conditions for plate analysis, including free edges and point supports, demonstrating how frequency varies with the aspect ratio and Poisson's ratio, is presented by (BARDELL, 1991). The Hierarchical Finite Element Method (HFEM) demonstrates precision across various plate aspect ratios and boundary conditions, proving its versatility and robustness compared to other methods.

A method using hierarchical trigonometric functions for modeling plate bending at medium frequencies was introduced by (BESLIN; NICOLAS, 1997). This approach efficiently handles very high orders and offers better accuracy and convergence rates for predicting bending modes and high-order natural flexural modes of rectangular plates with any boundary conditions.

A comparison of the Generalized Differential Quadrature Rules (GDQR) with the Ritz method for analyzing laminated composite plates was conducted by (DARVIZEH *et al.*, 2004). GDQR showed reliable and precise results, proving more computationally efficient than the Ritz method.

A buckling analysis for rectangular laminated composite plates with arbitrary edge supports under biaxial compression using Higher-Order Shear Deformation Theory was detailed by (NI *et al.*, 2005). This approach, integrated into the Ritz method, effectively analyzes composite plates with diverse edge supports, yielding precise buckling loads and modes.

Polynomial and trigonometric hierarchical sets for constructing Ritz bases to solve

the linear buckling of anisotropic Kirchhoff plates were examined by (YSHII *et al.*, 2018). Both sets provided upper bounds on the buckling load, with the polynomial Ritz basis proving more efficient and accurate for orthotropic and anisotropic plates compared to the trigonometric set and Nastran models.

A buckling solution considering prebuckling stress field heterogeneities due to edge constraints was developed by (NIMA; GANESAN, 2021). Using eigenvalue buckling analysis based on a calculated prebuckling in-plane stress field, this method effectively examines the impact of in-plane constraints and geometric configurations on the buckling behavior of anisotropic laminate plates.

These studies highlight significant advancements and diverse methodologies in the buckling analysis of laminated composite plates, emphasizing the importance of methodological accuracy, computational efficiency, and addressing complex boundary conditions for optimal structural design and stability.

2.2 Buckling Studies in Laminated Panels with Cutouts

A new design concept for composite panels under compression, featuring panels with two different concentric layups, was introduced by (KASSAPOGLOU, 2008). Using a Ritz-based approach, this study models rectangular panels to determine buckling loads and in-plane stresses, closely matching finite element models except in cases with significant twisting–bending coupling. The method also applies to plates with rectangular cutouts and terminated stiffeners.

The Ritz method with suitable admissible functions for accurately determining nondimensional frequencies of thick, cracked rectangular plates was demonstrated by (HUANG *et al.*, 2011). These functions effectively model stress singularities and discontinuities around cracks, with convergence studies confirming their efficiency.

A technique for modeling laminates with circular and elliptical holes, focusing on post-buckling and nonlinear behaviors under uniaxial compressive load, was introduced by (GHANNADPOUR; MEHRPARVAR, 2018). Using First-Order Shear Deformation Plate Theory and von Kármán's assumptions, the method approximates displacement fields with the Ritz method and Chebyshev polynomials, validated against finite element analyses.

An analytical solution for stress distribution in finite elastic plates with circular or square holes under biaxial partial loading was developed by (DEHGHANI, 2018). The method maps circular holes in rectangular plates, using Airy stress functions and Muskhelishvili's complex variable method to derive stress factors, showing significant effects of plate dimensions, hole size, and loading length on von Mises stress.

A Semi-Energy Finite Strip Method (SE-FSM) for analyzing buckling in laminated composites with a circular notch was presented by (SHOJAEE *et al.*, 2019). Combining the strengths of FEM and the Ritz method, SE-FSM showed high accuracy and efficiency compared to the full-energy FSM and FEM in examining specimen thickness, hole diameter, and stiffener thickness.

An investigation into the stress concentration effects at composite laminate openings was conducted by (ZHANG *et al.*, 2020), highlighting the effectiveness of local reinforcement and curvilinear laying schemes in enhancing stiffness and load-bearing capacities.

The impact of in-plane constraints on composite panel buckling was investigated by (NIMA; GANESAN, 2021). The study found that these constraints significantly affect critical buckling behavior, especially in laminates with shearing-stretching coupling. Oscillations in stress resultants, influenced by the plate's aspect ratio, were mitigated by increasing terms in the Ritz method. This research aids in optimizing composite structures by enhancing the understanding of in-plane constraints' effects on buckling.

A semi-analytical tool using the Ritz method for analyzing Variable Angle Tow (VAT) laminates with cutouts was developed by (JANSSENS, 2020), reducing computational costs while accurately predicting behavior near cutouts, prebuckling stresses, and buckling modes, validated against existing models and finite element solutions.

The Discrete Ritz Method (DRM) for buckling analysis of perforated plates with various geometries was introduced by (JING; DUAN, 2023). Utilizing Legendre polynomials for different boundary conditions and variable stiffness within a rectangular domain, the DRM effectively simulates the shapes of plates and cutouts. Numerical examples for isotropic and orthotropic materials demonstrate its effectiveness and stability, showing good agreement with previous results.

2.3   Buckling Studies in Stiffened Laminated Panels

An analysis method for stiffened plate systems supported by steel girders, focusing on ribbed and grid plate systems, was presented by (KUKRETI; CHERAGHI, 1993). Using energy principles, the deflection function combines polynomial and trigonometric series, with computed moments under static loading showing good agreement with finite element results.

The local buckling behavior of isotropic and laminated symmetric composite blade-stiffened plates under uniaxial compression was investigated by (STAMATELOS *et al.*, 2011). Using elastic edge supports modeled as springs, Classical Lamination Theory, pb-2 Ritz displacement functions, and the Ritz approach, the study provides an accurate, low-cost

analysis tool. Comparisons with non-linear finite element analysis confirm the method's accuracy for predicting critical buckling loads and post-buckling behavior.

A procedure for analyzing the vibration of stiffened panels with various openings and edge constraints using the assumed mode method was presented by (CHO *et al.*, 2014). Validated against finite element results, this method accurately incorporates stiffeners and openings, showing good agreement in natural frequencies and mode shapes.

A semi-analytical method to study the effects of skin-stiffener bonding flaws on the vibration and buckling of T-stiffened composite panels was introduced by (CASTRO; DON-ADON, 2017). Using hierarchical polynomial functions and a penalty-based approach, the method accurately models debonding lengths, aligning well with finite element analyses.

The buckling analysis of stiffened composite panels with debonding defects was investigated by (SILVA, 2021), underlining the adaptability of the Ritz method. Validated by finite element analyses and experimental tests, this model helps understand the impact of defect size on panel stability, providing a valuable tool for damage-tolerant aerostructure design.

An energy-based solution for calculating the buckling loads of partially anisotropic stiffened plates was detailed in (STAMATELOS; LABEAS, 2023), extending the Ritz method to anisotropic plate buckling solutions. This approach shows accuracy and efficiency over finite element analysis, highlighting its utility in preliminary design phases.

3 Buckling Problem Formulation

This study aims to implement the Discrete Ritz Method (DRM), as introduced by (JING; DUAN, 2023), to analyze the buckling behavior of panels featuring circular cutouts and stiffeners.

The adopted approach is based on a two-step solution for investigating the buckling behavior of laminated composite plates under in-plane constraints, as outlined in (NIMA; GANESAN, 2021) and (JING; DUAN, 2023). The initial step involves solving the in-plane elasticity problem to determine the distribution of stress resultants. The subsequent step uses the results from the first step to derive the linear stability equations. In both stages, the laminate is modeled using the First-Order Shear Deformation Theory (FSDT), and the solutions are obtained via the Ritz method. Hierarchical polynomials are used to formulate an admissible function capable of accommodating various boundary conditions, while avoiding the effects of discontinuities.

By utilizing a global trial function with variable stiffness properties in a virtual design domain, the deformation of arbitrarily shaped plates is accurately assessed through Gauss quadrature numerical integration. Additionally, this method enables the application of boundary conditions and load potential on any plate contour.

The mathematical modeling process initiates with the First-Order Shear Deformation Theory to delineate the relationships between in-plane forces and moments and the derivatives of mid-plane displacements. This step enables the substitution of these relationships into the energy equations, enabling the application of the Ritz method, which yields the buckling loads and corresponding displacement functions.

3.1 Limitations of the Ritz Method

According to (LUCENA NETO, 2021), the fundamental idea of the Ritz method is to reduce a continuous problem, with an infinite number of degrees of freedom, to a discrete problem with a finite number n of degrees of freedom. The coefficients c_i are the generalized coordinates of the discrete problem. By using this method, the direct

solution of differential equations is avoided, and algebraic equations are dealt with instead. However, according to (LUCENA NETO, 2021), in practice, there are several difficulties encountered in the application of the Ritz method:

1. It is a difficult, if not impossible, task to obtain approximations that satisfy the boundary conditions when the domain has an irregular geometry.

2. Changing the boundary conditions or the domain geometry can mean a complete change in the adopted approximation, with no systematic choice of the basis. Any computational implementation of these methods is usually limited to solving a very specific problem.

3. Adding terms to the approximation implies more laborious integrations and often results in an ill-conditioned problem.

4. There are cases where the exact solution of the problem is not given by a single function valid throughout the domain. This situation is clearly observed in the solution of the differential equation

$$au'' + f(x) = 0, \tag{3.1}$$

where $(\ )' = \frac{d(\ )}{dx}$, when the coefficient a or the function $f(x)$ are defined differently in distinct parts of the domain.

5. A solution could be improved by modifying the approximation only in the regions of the domain where it is necessary, such as where the solution varies abruptly. The use of new approximations that unnecessarily extend over the entire domain, as done by the Ritz method, could thus be avoided.

6. The coefficients c_i have no physical meaning. This is not, strictly speaking, a difficulty, but rather something that may be undesirable. There are some formulations of the finite element method that also use coefficients c_i without physical meaning.

3.2   The First-Order Shear Deformation Theory

The First-Order Shear Deformation Theory (FSDT) is an approach used in the structural analysis of laminated composite materials. Given appropriate assumptions, FSDT can predict the stress and strain distributions within each layer of a laminate in response to external loads. Furthermore, in this study, the mathematical modeling will consider the analysis of symmetric laminated composites. Therefore, simplifications consistent with this hypothesis will be made.

Classical Lamination Theory (CLT) is based on Kirchhoff's hypothesis, which assumes that a line segment normal to the mid-surface before deformation remains (LUCENA NETO, 2021):

- straight;

- normal to the deformed surface;

- with constant length.

In contrast, the First-Order Shear Deformation Theory is based on the Reissner-Mindlin hypothesis, which includes the effect of transverse shear deformation. According to this Theory, a line segment normal to the mid-surface before deformation remains straight and of the same length but does not necessarily remain orthogonal to the mid-surface after deformation, as depicted in Figure 3.1.
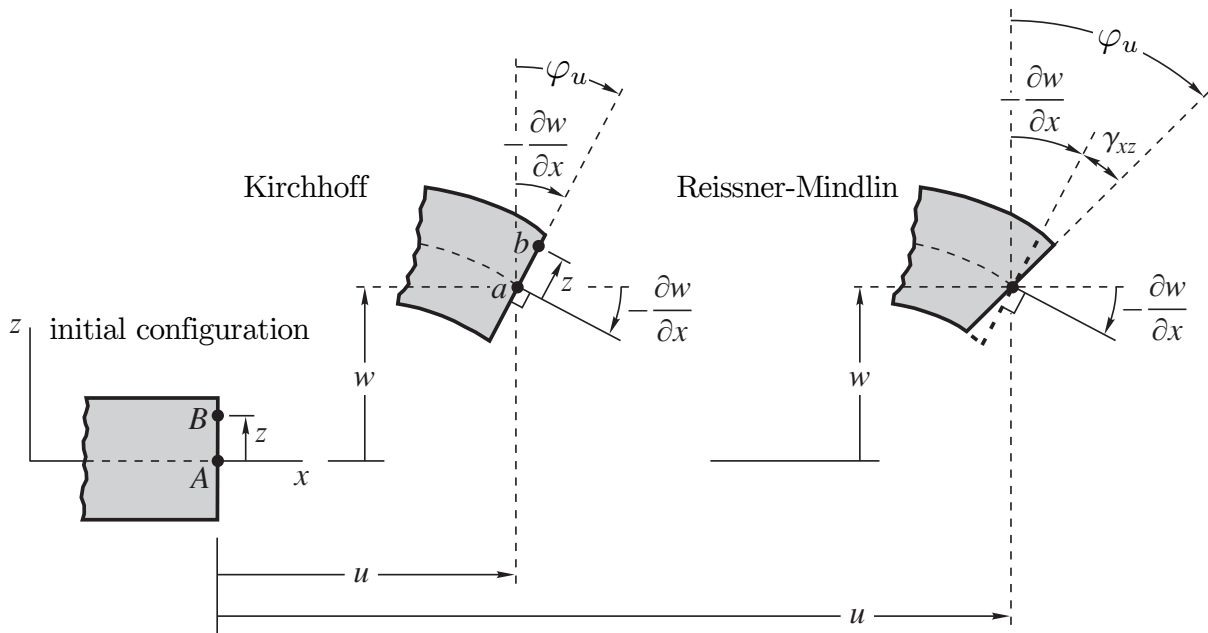
FIGURE 3.1 – Representative figure of the projection of segment AB, at a free edge, on the $x - z$ plane in the initial configuration and in the current configuration, after the plate deforms under small rotations and under the hypothesis of Kirchhoff or Reissner-Mindlin. Source: Adapted from (LUCENA NETO, 2021).

This modification allows the incorporation of transverse shear strains within the theoretical model. The theory stipulates that the displacement function w, representing the out-of-plane displacement, must not vary with the thickness coordinate z, maintaining the inextensibility of the transverse normals (REDDY, 2003). Consistent with the aforementioned premises, the displacement field in the First-Order Shear Deformation Theory can be expressed as:

$$u(x, y, z) = u_0(x, y) + z\varphi_u(x, y) \tag{3.2}$$

$$v(x, y, z) = v_0(x, y) + z\varphi_v(x, y) \tag{3.3}$$

$$w(x, y, z) = w_0(x, y) \tag{3.4}$$

where the functions $(u_0, v_0, w_0, \varphi_u, \varphi_v)$ represent the unknowns of the problem, with u_0, v_0, and w_0 specifically denoting the displacements at the mid-plane $(z = 0)$. It should be noted that:

$$\frac{\partial u}{\partial z} = -\varphi_u \quad \text{and} \quad \frac{\partial v}{\partial z} = -\varphi_v, \tag{3.5}$$

where φ_u and φ_v are, respectively, the rotations of a transverse normal around the y and x axes. Although the use of φ_u and φ_v to denote these rotations might seem unconventional and does not comply with the right-hand rule, this notation is prevalent in the literature (REDDY, 2003).

These parameters $(u_0, v_0, w_0, \varphi_u, \varphi_v)$ are termed the generalized displacements. For thin plates, the rotation functions φ_u and φ_v are expected to approximate the respective slopes of the transverse deflection (REDDY, 2003). Given the aforementioned displacement distribution, the infinitesimal mid-plane strains and curvatures of a laminate are expressed in terms of the displacements as:

$$\boldsymbol{\varepsilon} = \left\{ \begin{array}{c} \varepsilon_x \\ \varepsilon_y \\ \gamma_{xy} \end{array} \right\} = \left\{ \begin{array}{c} \frac{\partial u_0}{\partial x} \\ \frac{\partial v_0}{\partial y} \\ \frac{\partial u_0}{\partial y} + \frac{\partial v_0}{\partial x} \end{array} \right\} + z \left\{ \begin{array}{c} \frac{\partial \varphi_u}{\partial x} \\ \frac{\partial \varphi_v}{\partial y} \\ \frac{\partial \varphi_u}{\partial y} + \frac{\partial \varphi_v}{\partial x} \end{array} \right\} = \boldsymbol{\varepsilon^0} + z\boldsymbol{\kappa} \tag{3.6}$$

where $\boldsymbol{\varepsilon^0}$ and $\boldsymbol{\kappa}$ represent the in-plane strains and curvatures, respectively.

As adopted in (NIMA; GANESAN, 2021), a nonlinear strain definition capable of accommodating moderate rotational effects is used. Within this framework, von Kármán's approximations, represented by $\tilde{\boldsymbol{\varepsilon}}$, are included as additional nonlinear terms to compute the mid-plane strains induced by out-of-plane deflections. These extra nonlinear terms are shown in Equation 3.7. It should be noted that in the adopted model, these nonlinear terms are not used to derive the constitutive model. Instead, they contribute only to the stress stiffening energy in the buckling analysis stage, which will be discussed later.

$$\tilde{\boldsymbol{\varepsilon}} = \left\{ \begin{array}{c} \frac{1}{2}\left(\frac{\partial w_0}{\partial x}\right)^2 \\ \frac{1}{2}\left(\frac{\partial w_0}{\partial y}\right)^2 \\ \frac{\partial w_0}{\partial x}\frac{\partial w_0}{\partial y} \end{array} \right\} \tag{3.7}$$

The transverse shear strains to be incorporated in the First-Order Shear Deformation Theory are defined as:

$$\boldsymbol{\gamma} = \begin{Bmatrix} \gamma_{yz} \\ \gamma_{xz} \end{Bmatrix} = \begin{Bmatrix} \varphi_v + \frac{\partial w_0}{\partial y} \\ \varphi_u + \frac{\partial w_0}{\partial x} \end{Bmatrix} \tag{3.8}$$

The coordinate system that will be adopted in the mathematical modeling, considering a generic lamina k of an orthotropic material, is represented in Figure 3.2. The system $x_1 x_2 x_3$ is obtained from the xyz system, common to all laminas, by a counterclockwise rotation θ of the xy plane around the x_3 axis.
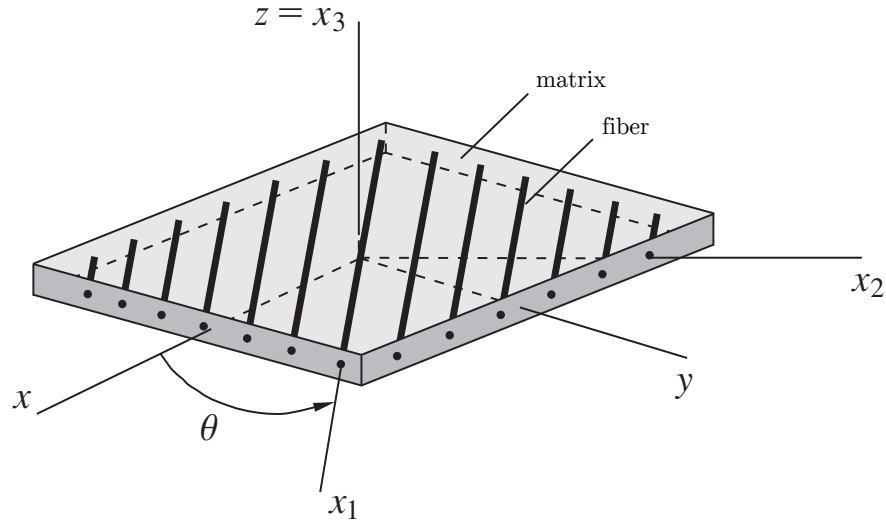
FIGURE 3.2 – Representative figure of a lamina with unidirectional fibers and principal material coordinate system $x_1 x_2 x_3$. Source: Adapted from (LUCENA NETO, 2021).

For a generic lamina k of an orthotropic material, as shown in Figure 3.2, with unidirectional fiber and material axis system $x_1 x_2 x_3$, the stress-strain relationship can be expressed as:

$$\begin{Bmatrix} \sigma_1 \\ \sigma_2 \\ \tau_{12} \end{Bmatrix}^{(k)} = \begin{bmatrix} Q_{11} & Q_{12} & 0 \\ Q_{12} & Q_{22} & 0 \\ 0 & 0 & Q_{66} \end{bmatrix}^{(k)} \begin{Bmatrix} \varepsilon_1 \\ \varepsilon_2 \\ \gamma_{12} \end{Bmatrix}^{(k)} \qquad \begin{Bmatrix} \tau_{23} \\ \tau_{13} \end{Bmatrix}^{(k)} = \begin{bmatrix} Q_{44} & 0 \\ 0 & Q_{55} \end{bmatrix}^{(k)} \begin{Bmatrix} \gamma_{23} \\ \gamma_{13} \end{Bmatrix}^{(k)} \tag{3.9}$$

where

$$Q_{11} = \frac{E_1}{1 - \nu_{21}\nu_{12}} \qquad Q_{12} = \frac{\nu_{12}E_2}{1 - \nu_{21}\nu_{12}} = \frac{\nu_{21}E_1}{1 - \nu_{21}\nu_{12}} \qquad Q_{22} = \frac{E_2}{1 - \nu_{21}\nu_{12}}$$

$$Q_{44} = G_{23} \qquad\qquad Q_{55} = G_{13} \qquad\qquad Q_{66} = G_{12}$$

The relationship between $\boldsymbol{\sigma}^{(k)}$ and $\boldsymbol{\varepsilon}^{(k)}$ in the xyz system can be written as:

$$\begin{Bmatrix} \sigma_x \\ \sigma_y \\ \tau_{xy} \end{Bmatrix}^{(k)} = \begin{bmatrix} \overline{Q}_{11} & \overline{Q}_{12} & \overline{Q}_{16} \\ \overline{Q}_{12} & \overline{Q}_{22} & \overline{Q}_{26} \\ \overline{Q}_{16} & \overline{Q}_{26} & \overline{Q}_{66} \end{bmatrix}^{(k)} \begin{Bmatrix} \varepsilon_x \\ \varepsilon_y \\ \gamma_{xy} \end{Bmatrix}^{(k)} \Leftrightarrow \boldsymbol{\sigma}^{(k)} = \overline{\mathbf{Q}}_b^{(k)} \boldsymbol{\varepsilon}^{(k)} \tag{3.10}$$

where the stiffness matrix $\overline{\mathbf{Q}}_b^{(k)}$ is obtained from the rotation of the stiffness matrix by an angle θ equal to the fiber orientation of the ply, as shown in Equation 3.11.

$$\overline{\mathbf{Q}}_b^{(k)} = \begin{bmatrix} \overline{Q}_{11} & \overline{Q}_{12} & \overline{Q}_{16} \\ \overline{Q}_{12} & \overline{Q}_{22} & \overline{Q}_{26} \\ \overline{Q}_{16} & \overline{Q}_{26} & \overline{Q}_{66} \end{bmatrix}^{(k)} = \mathbf{T}_b^{-1(k)} \begin{bmatrix} Q_{11} & Q_{12} & 0 \\ Q_{12} & Q_{22} & 0 \\ 0 & 0 & Q_{66} \end{bmatrix}^{(k)} \mathbf{T}_b^{-T(k)} \tag{3.11}$$

where

$$\mathbf{T}_b^{(k)} = \begin{bmatrix} \cos^2\theta & \sin^2\theta & 2\cos\theta\sin\theta \\ \sin^2\theta & \cos^2\theta & -2\cos\theta\sin\theta \\ -\cos\theta\sin\theta & \cos\theta\sin\theta & \cos^2\theta - \sin^2\theta \end{bmatrix}^{(k)} \tag{3.12}$$

The relationship between $\boldsymbol{\tau}^{(k)}$ and $\boldsymbol{\gamma}^{(k)}$ in the xyz system can be written as:

$$\begin{Bmatrix} \tau_{yz} \\ \tau_{xz} \end{Bmatrix}^{(k)} = \begin{bmatrix} \overline{Q}_{44} & \overline{Q}_{45} \\ \overline{Q}_{45} & \overline{Q}_{55} \end{bmatrix}^{(k)} \begin{Bmatrix} \gamma_{yz} \\ \gamma_{xz} \end{Bmatrix}^{(k)} \Leftrightarrow \boldsymbol{\tau}^{(k)} = \overline{\mathbf{Q}}_s^{(k)} \boldsymbol{\gamma}^{(k)} \tag{3.13}$$

where the stiffness matrix $\overline{\mathbf{Q}}_s^{(k)}$ is obtained from the rotation of the stiffness matrix by an angle θ equal to the fiber orientation of the ply, as shown in Equation 3.14.

$$\overline{\mathbf{Q}}_s^{(k)} = \mathbf{T}_s^{(k)T} \begin{bmatrix} Q_{44} & 0 \\ 0 & Q_{55} \end{bmatrix}^{(k)} \mathbf{T}_s^{(k)} \tag{3.14}$$

where

$$\mathbf{T}_s^{(k)} = \begin{bmatrix} \cos\theta & -\sin\theta \\ \sin\theta & \cos\theta \end{bmatrix}^{(k)} \tag{3.15}$$

The representation of transverse shear strains as constant through the laminate thickness implies that the transverse shear stresses will also be constant. This inconsistency generates excessive stiffness, especially for relatively thick laminates (NIMA; GANESAN, 2021). However, elementary theory of homogeneous beams indicates that the transverse shear stress varies parabolically through the beam thickness (REDDY, 2003). In composite laminated beams and plates, the transverse shear stresses exhibit at least a quadratic variation through the layer thickness. The discrepancy between the actual stress state and

the constant stress state predicted by the First-Order Shear Deformation Theory necessitates the correction of transverse shear stress resultants by introducing a shear correction coefficient, K_s (REDDY, 2003):

$$\begin{Bmatrix} S_{yz} \\ S_{xz} \end{Bmatrix} = \int_{-h/2}^{h/2} K_s \begin{Bmatrix} \tau_{yz} \\ \tau_{xz} \end{Bmatrix} dz \qquad (3.16)$$

This modification adjusts the plate transverse shear stiffnesses. The shear correction coefficient, K_s, is determined to ensure that the strain energy due to transverse shear stresses equals the strain energy due to the true transverse stresses predicted by three-dimensional elasticity theory (REDDY, 2003).

According to (NIMA; GANESAN, 2021), unlike isotropic materials, no single optimum value can be prescribed for layered composite materials, and the correction factors need to be calculated for each laminate separately. Studies, such as those by (REDDY, 2003), have shown that using $K_s = \frac{5}{6}$ provides an accurate approximation for the transverse shear stiffness in composite laminates, making it a standard choice in structural analysis. This value is derived to equate the shear strain energy in both actual and simplified theories, thereby ensuring accurate modeling of transverse shear effects in composite laminates. However, this is a simplified approach adopted to avoid increased methodological complexity. Various methodologies for determining the shear correction factor are available, including dynamic analysis where this factor depends on the plate material constants and aspect ratio (ZWEBEN; BEAUMONT, 2017). Therefore, the value of $K_s = \frac{5}{6}$ was used in this work. In Figure 3.3, the orientations of the forces and moments per unit width in the mid-plane of a laminate can be observed.
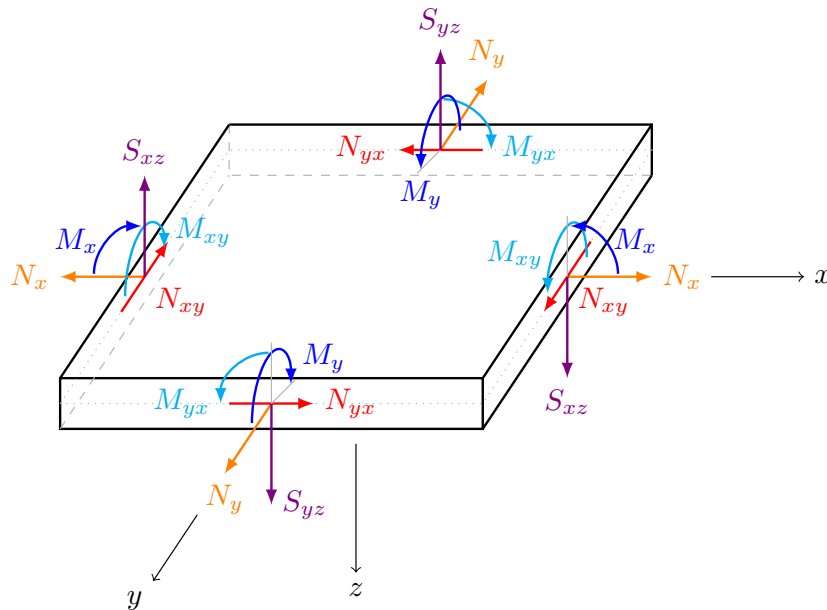
FIGURE 3.3 – Forces and moments per unit width in the mid-plane of a laminate.

In Figure 3.4, the geometric arrangement of the plies of an N_L-layered laminate can be observed.
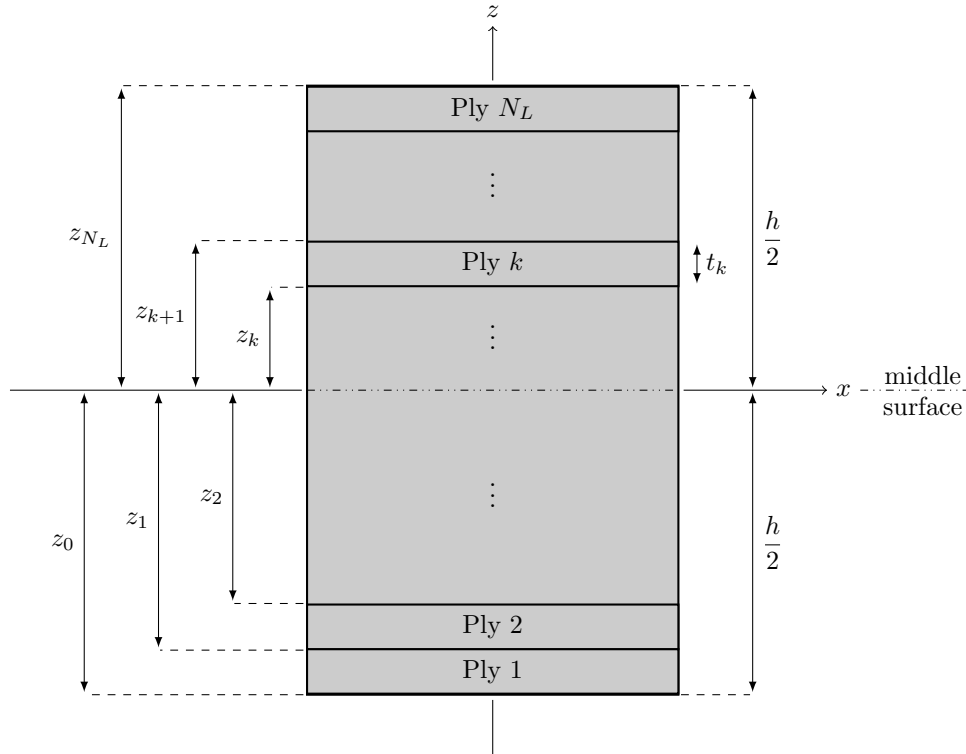
FIGURE 3.4 – Representative figure of the geometric arrangement of the plies of an N_L-layered laminate.

For an N_L-layered laminate of thickness h, with axis orientation such as the one shown in Figure 3.4, the forces and moments per unit width, which are displayed in Figure 3.3, can be calculated as

$$\mathbf{N} = \begin{Bmatrix} N_x \\ N_y \\ N_{xy} \end{Bmatrix} = \int_{-h/2}^{h/2} \begin{Bmatrix} \sigma_x \\ \sigma_y \\ \tau_{xy} \end{Bmatrix} dz = \sum_{k=1}^{N_L} \int_{z_{k-1}}^{z_k} \begin{Bmatrix} \sigma_x \\ \sigma_y \\ \tau_{xy} \end{Bmatrix} dz \qquad (3.17)$$

$$\mathbf{M} = \begin{Bmatrix} M_x \\ M_y \\ M_{xy} \end{Bmatrix} = \int_{-h/2}^{h/2} \begin{Bmatrix} \sigma_x \\ \sigma_y \\ \tau_{xy} \end{Bmatrix} z\,dz = \sum_{k=1}^{N_L} \int_{z_{k-1}}^{z_k} \begin{Bmatrix} \sigma_x \\ \sigma_y \\ \tau_{xy} \end{Bmatrix} z\,dz \qquad (3.18)$$

$$\mathbf{S} = \begin{Bmatrix} S_{yz} \\ S_{xz} \end{Bmatrix} \approx \int_{-h/2}^{h/2} K_s \begin{Bmatrix} \tau_{yz} \\ \tau_{xz} \end{Bmatrix} dz = \sum_{k=1}^{N_L} \int_{z_{k-1}}^{z_k} K_s \begin{Bmatrix} \tau_{yz} \\ \tau_{xz} \end{Bmatrix} dz \qquad (3.19)$$

Substituting the relationship between $\boldsymbol{\sigma}^{(k)}$ and $\boldsymbol{\varepsilon}^{(k)}$ given in Equation 3.10 and the relationship between $\boldsymbol{\tau}^{(k)}$ and $\boldsymbol{\gamma}^{(k)}$ given in Equation 3.13 into Equations 3.17, 3.18, and 3.19, and the following is obtained:

$$\begin{Bmatrix} N_x \\ N_y \\ N_{xy} \end{Bmatrix} = \mathbf{A} \begin{Bmatrix} \varepsilon_x^0 \\ \varepsilon_y^0 \\ \gamma_{xy}^0 \end{Bmatrix} + \mathbf{B} \begin{Bmatrix} \kappa_x \\ \kappa_y \\ \kappa_{xy} \end{Bmatrix} \tag{3.20}$$

$$\begin{Bmatrix} M_x \\ M_y \\ M_{xy} \end{Bmatrix} = \mathbf{B} \begin{Bmatrix} \varepsilon_x^0 \\ \varepsilon_y^0 \\ \gamma_{xy}^0 \end{Bmatrix} + \mathbf{D} \begin{Bmatrix} \kappa_x \\ \kappa_y \\ \kappa_{xy} \end{Bmatrix} \tag{3.21}$$

$$\begin{Bmatrix} S_{yz} \\ S_{xz} \end{Bmatrix} = \mathbf{H} \begin{Bmatrix} \varphi_v + \frac{\partial w_0}{\partial y} \\ \varphi_u + \frac{\partial w_0}{\partial x} \end{Bmatrix} \tag{3.22}$$

where

$$\mathbf{A} = \begin{bmatrix} A_{11} & A_{12} & A_{16} \\ A_{12} & A_{22} & A_{26} \\ A_{16} & A_{26} & A_{66} \end{bmatrix} = \sum_{k=1}^{N_L} (z_k - z_{k-1})\bar{\mathbf{Q}}_b^{(k)} \tag{3.23}$$

$$\mathbf{B} = \begin{bmatrix} B_{11} & B_{12} & B_{16} \\ B_{12} & B_{22} & B_{26} \\ B_{16} & B_{26} & B_{66} \end{bmatrix} = \frac{1}{2}\sum_{k=1}^{N_L} (z_k^2 - z_{k-1}^2)\bar{\mathbf{Q}}_b^{(k)} \tag{3.24}$$

$$\mathbf{D} = \begin{bmatrix} D_{11} & D_{12} & D_{16} \\ D_{12} & D_{22} & D_{26} \\ D_{16} & D_{26} & D_{66} \end{bmatrix} = \frac{1}{3}\sum_{k=1}^{N_L} (z_k^3 - z_{k-1}^3)\bar{\mathbf{Q}}_b^{(k)} \tag{3.25}$$

$$\mathbf{H} = \begin{bmatrix} A_{44} & A_{45} \\ A_{45} & A_{55} \end{bmatrix} = \sum_{k=1}^{N_L} (z_k - z_{k-1})\bar{\mathbf{Q}}_s^{(k)} \tag{3.26}$$

The constitutive relationship for the laminated composite plate is

$$\begin{Bmatrix} \mathbf{N} \\ \mathbf{M} \\ \mathbf{S} \end{Bmatrix} = \begin{bmatrix} \mathbf{A} & \mathbf{B} & \mathbf{0} \\ \mathbf{B} & \mathbf{D} & \mathbf{0} \\ \mathbf{0} & \mathbf{0} & \mathbf{H} \end{bmatrix} \begin{Bmatrix} \boldsymbol{\varepsilon}^0 \\ \boldsymbol{\kappa} \\ \boldsymbol{\gamma} \end{Bmatrix} \tag{3.27}$$

Laminates that are symmetric in both geometry and material properties about the mid-surface have $\mathbf{B} = \mathbf{0}$, indicating that there is no coupling between bending and extension, nor between torsion and in-plane shear (LEVY NETO; PARDINI, 2018). Furthermore, if the layers are specially orthotropic (i.e., principal material directions aligned with the laminate axis), then $A_{16} = A_{26} = 0$, $D_{16} = D_{26} = 0$ and $A_{45} = 0$ (JONES, 1998).

3.3   Discrete Ritz Method

The Discrete Ritz Method (DRM) was introduced by (JING; DUAN, 2023) to overcome the limitations of the traditional Ritz method in handling complex geometric domains. This numerical approach is designed for analyzing the buckling of plates with arbitrary shapes and cutouts. DRM utilizes polynomials to construct admissible functions that can accommodate various boundary conditions. By integrating the principles of variational calculus with the concept of stationary total potential energy, standard energy functionals and computational procedures are developed to determine buckling eigenvalues and mode shapes.

In DRM, the modeling process for perforated plates of arbitrary geometries is standardized. A rectangle that covers the plate's geometric domain is initially constructed, with dimensions matching the plate's maximum dimensions in the x and y directions. This rectangle and the plate geometry are then mapped into a standard square domain in the $\xi \in [-1, 1]$ and $\eta \in [-1, 1]$ directions. Within this virtual rectangular design domain, a global trial function with variable stiffness properties models the deformation of plates with complex geometries through numerical integration via Gauss quadrature.

To accurately represent cutouts in the plate domain, the plate is modeled with variable thickness. Regions corresponding to the cutouts are assigned zero thickness and stiffness. Additionally, boundary conditions and load potentials can be applied to any contour of the plate. Gauss quadrature is used for numerical integration over these complex domains, treating the plate as a variable stiffness system with zero stiffness in cutouts. In the rest of the plate domain, the thickness remains constant, effectively nullifying the stiffness in the cutout regions. For an orthotropic plate with cutouts, stiffness is a function of plate coordinates x and y and becomes zero within the cutout areas:

$$A_{ij}(x,y) = 0 \quad \text{for } i,j = 1,2,6; 4,5 \tag{3.28}$$

$$B_{ij}(x,y) = 0 \quad \text{for } i,j = 1,2,6 \tag{3.29}$$

$$D_{ij}(x,y) = 0 \quad \text{for } i,j = 1,2,6 \tag{3.30}$$
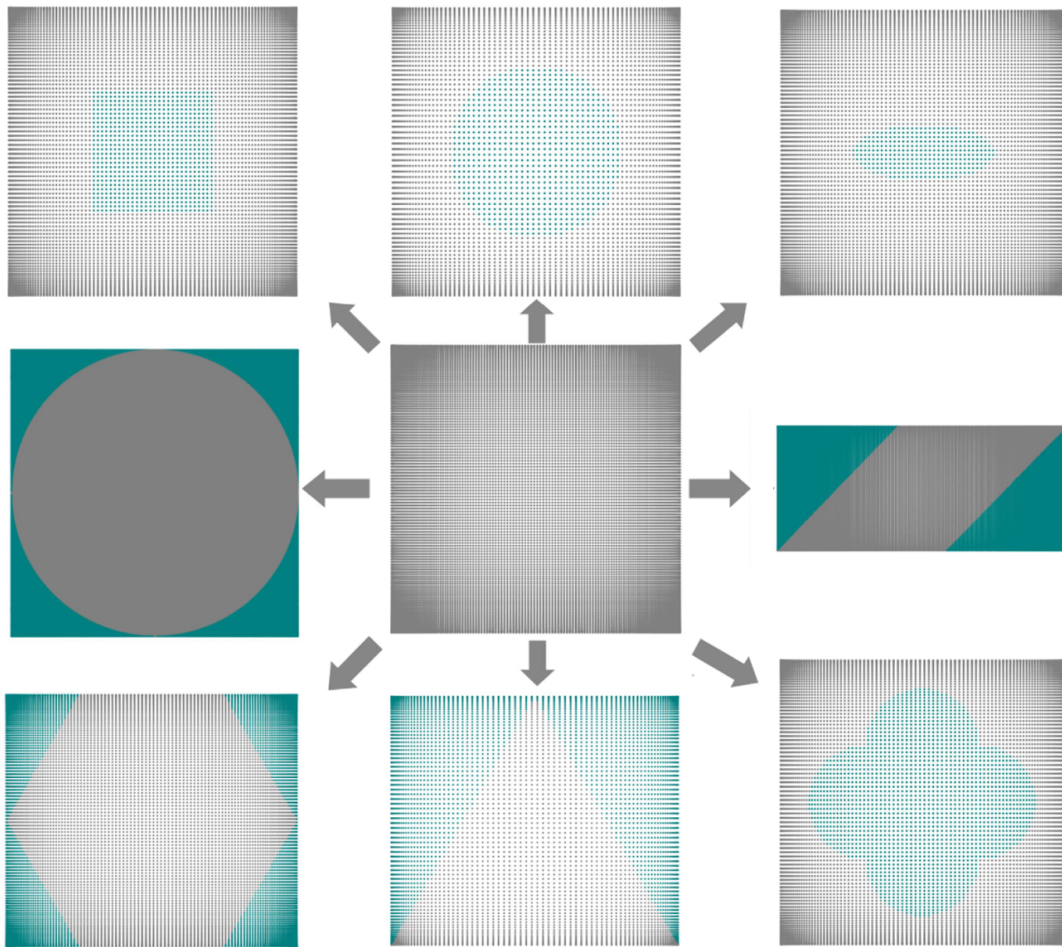
FIGURE 3.5 – Representative figure of the Discrete Ritz Method (DRM), proposed by (JING; DUAN, 2023), utilizing Gauss points to discretize any shaped plate with arbitrary cutouts. Green points indicate zero stiffness and thickness to simulate cutouts, while gray points represent the plate domain. Source: (JING; DUAN, 2023).

3.4   Hierarchical Polynomials

In this work, the admissible function used is based on hierarchical polynomials, considering various boundary conditions along the plate contour. A trial solution that satisfies the boundary conditions of the problem and contains adjustable parameters is first assumed. The method then seeks to determine the values of these parameters by taking the first variation of a specific functional, often related to the potential or total energy of the system under study. This functional is derived from the governing equations and boundary conditions of the problem.

The shape functions used are the hierarchical polynomials proposed by (BARDELL, 1991). The first four cubic polynomials are conventionally used in FEM for bending problems, as these polynomials define the boundary conditions (BARDELL, 1991). Only the first four polynomials do not have zero rotation and displacement at their limits. For

a free boundary condition, all polynomials are used. All higher degree polynomials ($i > 4$) have both zero displacement and zero slope at each end of the element (ξ or $\eta = $ -1; 1) and are used to enrich the shape function. The set of functions used in this work is derived from Rodrigues' form of Legendre orthogonal polynomials and is given by:

$$\chi_1(\xi \text{ or } \eta) = \frac{1}{2} - \frac{3}{4}(\xi \text{ or } \eta) + \frac{1}{4}(\xi \text{ or } \eta)^3$$

$$\chi_2(\xi \text{ or } \eta) = \frac{1}{8} - \frac{1}{8}(\xi \text{ or } \eta) - \frac{1}{8}(\xi \text{ or } \eta)^2 + \frac{1}{8}(\xi \text{ or } \eta)^3$$

$$\chi_3(\xi \text{ or } \eta) = \frac{1}{2} + \frac{3}{4}(\xi \text{ or } \eta) - \frac{1}{4}(\xi \text{ or } \eta)^3$$

$$\chi_4(\xi \text{ or } \eta) = -\frac{1}{8} - \frac{1}{8}(\xi \text{ or } \eta) + \frac{1}{8}(\xi \text{ or } \eta)^2 + \frac{1}{8}(\xi \text{ or } \eta)^3$$

$$\chi_i(\xi \text{ or } \eta) = \sum_{k=0}^{i/2} \frac{(-1)^k}{2^k k!} \frac{(2i - 2k - 7)!!}{(i - 2k - 1)!}(\xi \text{ or } \eta)^{i-2k-1} \quad i = 5, 6, 7, \ldots \qquad (3.31)$$

where $k!! = k(k - 2)(k - 4)\ldots(2 \text{ or } 1)$, $0!! = (-1)!! = 1$, and $i/2$ denotes its own integer part.

Mathematically, the behavior of the hierarchical polynomials which allows for them to represent multiple boundary conditions can be summarized by:

$$\chi_1(-1) \neq 0 \text{ and } \chi_i(-1) = 0 \text{ if } i \neq 1 \qquad \chi_3(1) \neq 0 \text{ and } \chi_i(1) = 0 \text{ if } i \neq 3$$

$$\chi_2'(-1) \neq 0 \text{ and } \chi_i'(-1) = 0 \text{ if } i \neq 2 \qquad \chi_4'(1) \neq 0 \text{ and } \chi_i'(1) = 0 \text{ if } i \neq 4$$

Additionally, the procedure to satisfy the boundary conditions for a specific configuration is shown in Table 3.1.

TABLE 3.1 – Procedure adopted to satisfy the boundary conditions for a given problem using the ξ variable.

Restriction	Location	Adopted Procedure
Displacement	Left edge	$\chi_1(\xi) = 0$
Rotation	Left edge	$\chi_2(\xi) = 0$
Displacement	Right edge	$\chi_3(\xi) = 0$
Rotation	Right edge	$\chi_4(\xi) = 0$

The desired boundary conditions are achieved through the elimination all or some of the first four functions $\chi_i(\xi)$ and $\chi_j(\eta)$. For a plate simply supported along its four edges (SSSS), functions of w displacement, for example, $\chi_1(\xi), \chi_3(\xi), \chi_1(\eta)$ and $\chi_3(\eta)$ are eliminated, since they are not null in $\xi = \pm 1$ and $\eta \pm 1$. In this case, w will only have, effectively $(I - 2)(J - 2)$ terms.

In this approach, the displacements of the mid-surface of the plate shown in Figure

3.4 along the u_0, v_0, w_0, φ_u, and φ_v directions are expressed as a product of a row vector of unknown coefficients and a column vector of the Ritz basis functions, as shown in Equations 3.32, 3.33, 3.34, 3.35 and 3.36, respectively.

$$
\begin{aligned}
u_0(\xi,\eta) &= \sum_{i=1}^{I}\sum_{j=1}^{J} c_{ij}^{u}\chi_i^{u}(\xi)\chi_j^{u}(\eta) = \mathbf{c}^{u}\left[\mathbf{f}^{u}(\xi,\eta)\right]^{T} \\
\mathbf{c}^{u} &= \begin{bmatrix} c_{11}^{u} & \cdots & c_{1J}^{u} & c_{21}^{u} & \cdots & c_{2J}^{u} & \cdots & c_{I1}^{u} & \cdots & c_{IJ}^{u} \end{bmatrix} \\
\mathbf{f}^{u} &= \begin{bmatrix} \chi_1^{u}\chi_1^{u} & \cdots & \chi_1^{u}\chi_J^{u} & \chi_2^{u}\chi_1^{u} & \cdots & \chi_2^{u}\chi_J^{u} & \cdots & \chi_I^{u}\chi_1^{u} & \cdots & \chi_I^{u}\chi_J^{u} \end{bmatrix}
\end{aligned}
\tag{3.32}
$$

$$
\begin{aligned}
v_0(\xi,\eta) &= \sum_{i=1}^{I}\sum_{j=1}^{J} c_{ij}^{v}\chi_i^{v}(\xi)\chi_j^{v}(\eta) = \mathbf{c}^{v}\left[\mathbf{f}^{v}(\xi,\eta)\right]^{T} \\
\mathbf{c}^{v} &= \begin{bmatrix} c_{11}^{v} & \cdots & c_{1J}^{v} & c_{21}^{v} & \cdots & c_{2J}^{v} & \cdots & c_{I1}^{v} & \cdots & c_{IJ}^{v} \end{bmatrix} \\
\mathbf{f}^{v} &= \begin{bmatrix} \chi_1^{v}\chi_1^{v} & \cdots & \chi_1^{v}\chi_J^{v} & \chi_2^{v}\chi_1^{v} & \cdots & \chi_2^{v}\chi_J^{v} & \cdots & \chi_I^{v}\chi_1^{v} & \cdots & \chi_I^{v}\chi_J^{v} \end{bmatrix}
\end{aligned}
\tag{3.33}
$$
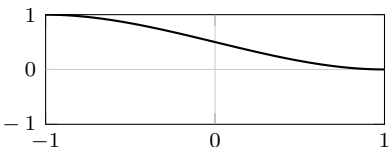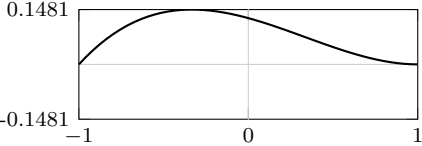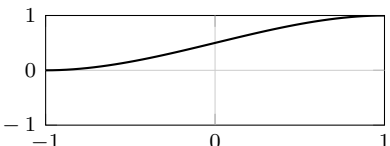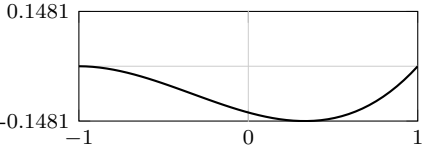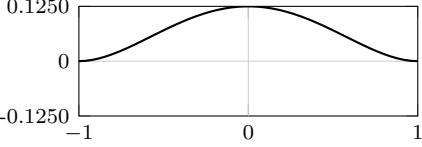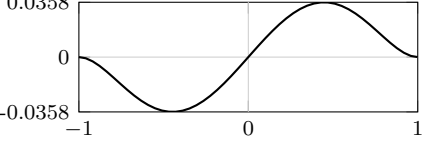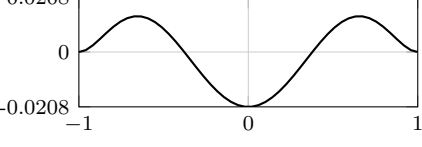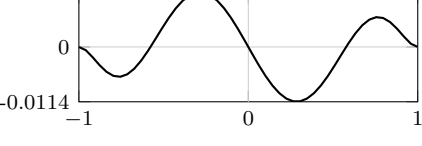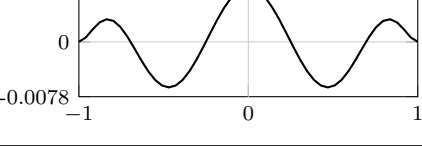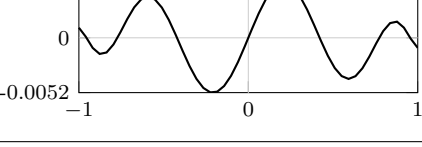
$$
\begin{aligned}
w_0(\xi,\eta) &= \sum_{i=1}^{I}\sum_{j=1}^{J} c_{ij}^{w}\chi_i^{w}(\xi)\chi_j^{w}(\eta) = \mathbf{c}^{w}\left[\mathbf{f}^{w}(\xi,\eta)\right]^{T} \\
\mathbf{c}^{w} &= \begin{bmatrix} c_{11}^{w} & \cdots & c_{1J}^{w} & c_{21}^{w} & \cdots & c_{2J}^{w} & \cdots & c_{I1}^{w} & \cdots & c_{IJ}^{w} \end{bmatrix} \\
\mathbf{f}^{w} &= \begin{bmatrix} \chi_1^{w}\chi_1^{w} & \cdots & \chi_1^{w}\chi_J^{w} & \chi_2^{w}\chi_1^{w} & \cdots & \chi_I^{w}\chi_1^{w} & \cdots & \chi_I^{w}\chi_J^{w} \end{bmatrix}
\end{aligned}
\tag{3.34}
$$

$$
\begin{aligned}
\varphi_u(\xi,\eta) &= \sum_{i=1}^{I}\sum_{j=1}^{J} c_{ij}^{\varphi_u}\chi_i^{\varphi_u}(\xi)\chi_j^{\varphi_u}(\eta) = \mathbf{c}^{\varphi_u}\left[\mathbf{f}^{\varphi_u}(\xi,\eta)\right]^{T} \\
\mathbf{c}^{\varphi_u} &= \begin{bmatrix} c_{11}^{\varphi_u} & \cdots & c_{1J}^{\varphi_u} & c_{21}^{\varphi_u} & \cdots & c_{2J}^{\varphi_u} & \cdots & c_{I1}^{\varphi_u} & \cdots & c_{IJ}^{\varphi_u} \end{bmatrix} \\
\mathbf{f}^{\varphi_u} &= \begin{bmatrix} \chi_1^{\varphi_u}\chi_1^{\varphi_u} & \cdots & \chi_1^{\varphi_u}\chi_J^{\varphi_u} & \chi_2^{\varphi_u}\chi_1^{\varphi_u} & \cdots & \chi_I^{\varphi_u}\chi_1^{\varphi_u} & \cdots & \chi_I^{\varphi_u}\chi_J^{\varphi_u} \end{bmatrix}
\end{aligned}
\tag{3.35}
$$

$$
\begin{aligned}
\varphi_v(\xi,\eta) &= \sum_{i=1}^{I}\sum_{j=1}^{J} c_{ij}^{\varphi_v}\chi_i^{\varphi_v}(\xi)\chi_j^{\varphi_v}(\eta) = \mathbf{c}^{\varphi_v}\left[\mathbf{f}^{\varphi_v}(\xi,\eta)\right]^{T} \\
\mathbf{c}^{\varphi_v} &= \begin{bmatrix} c_{11}^{\varphi_v} & \cdots & c_{1J}^{\varphi_v} & c_{21}^{\varphi_v} & \cdots & c_{2J}^{\varphi_v} & \cdots & c_{I1}^{\varphi_v} & \cdots & c_{IJ}^{\varphi_v} \end{bmatrix} \\
\mathbf{f}^{\varphi_v} &= \begin{bmatrix} \chi_1^{\varphi_v}\chi_1^{\varphi_v} & \cdots & \chi_1^{\varphi_v}\chi_J^{\varphi_v} & \chi_2^{\varphi_v}\chi_1^{\varphi_v} & \cdots & \chi_I^{\varphi_v}\chi_1^{\varphi_v} & \cdots & \chi_I^{\varphi_v}\chi_J^{\varphi_v} \end{bmatrix}
\end{aligned}
\tag{3.36}
$$

where c_{ij}^{u}, c_{ij}^{v}, c_{ij}^{w}, $c_{ij}^{\varphi_u}$ and $c_{ij}^{\varphi_v}$ are unknown coefficients to be determined, $\chi_i(\xi)$ and $\chi_j(\eta)$ are the hierarchical polynomials. In Table 3.2, the behavior of the first ten hierarchical polynomials is illustrated.

TABLE 3.2 – Behavior of the first ten hierarchical polynomials for the ξ variable. Adapted from (BARDELL, 1991).

Polynomial	Plot
$\chi_1(\xi) = \dfrac{1}{2} - \dfrac{3}{4}\xi + \dfrac{1}{4}\xi^3$	
$\chi_2(\xi) = \dfrac{1}{8} - \dfrac{1}{8}\xi - \dfrac{1}{8}\xi^2 + \dfrac{1}{8}\xi^3$	
$\chi_3(\xi) = \dfrac{1}{2} + \dfrac{3}{4}\xi - \dfrac{1}{4}\xi^3$	
$\chi_4(\xi) = -\dfrac{1}{8} - \dfrac{1}{8}\xi + \dfrac{1}{8}\xi^2 + \dfrac{1}{8}\xi^3$	
$\chi_5(\xi) = \dfrac{1}{8} - \dfrac{1}{4}\xi^2 + \dfrac{1}{8}\xi^4$	
$\chi_6(\xi) = \dfrac{1}{8}\xi - \dfrac{1}{4}\xi^3 + \dfrac{1}{8}\xi^5$	
$\chi_7(\xi) = -\dfrac{1}{48} + \dfrac{3}{16}\xi^2 - \dfrac{5}{16}\xi^4 + \dfrac{7}{48}\xi^6$	
$\chi_8(\xi) = -\dfrac{3}{48}\xi + \dfrac{5}{16}\xi^3 - \dfrac{7}{16}\xi^5 + \dfrac{9}{48}\xi^7$	
$\chi_9(\xi) = -\dfrac{3}{384} - \dfrac{15}{96}\xi^2 + \dfrac{35}{64}\xi^4 - \dfrac{63}{96}\xi^6 + \dfrac{99}{384}\xi^8$	
$\chi_{10}(\xi) = \dfrac{15}{384}\xi - \dfrac{35}{96}\xi^3 + \dfrac{63}{64}\xi^5 - \dfrac{99}{96}\xi^7 + \dfrac{143}{384}\xi^9$	

3.5   Gauss Quadrature Integration

This study employs Gauss quadrature for numerical integration, complemented by symbolic differentiation of the trial shape functions in software MATLAB®. Gauss quadrature is capable of accurately integrating polynomials of degree $2n - 1$ or lower using an n-point quadrature rule (JING; DUAN, 2023). Legendre polynomials, defined by the number of terms I and J in the ξ and η directions respectively, ensure the required precision through suitable integration points. Within the interval $[-1, 1]$, Gauss quadrature is used to evaluate the following integral:

$$\int_{-1}^{1} f(\xi)d\xi \approx \sum_{i=1}^{n} \bar{w}_i f(\xi_i) \tag{3.37}$$

where ξ_i are the integration points, defined as the roots of the Legendre polynomials $P_n(\xi)$, which can be expressed by a compact formula for the Legendre polynomials given by Rodrigues' formula:

$$P_n(x) = \frac{1}{2^n n!} \frac{d^n}{dx^n}[(x^2 - 1)^n] \tag{3.38}$$

and $\bar{w}_i$ are the corresponding weights calculated by:

$$\bar{w}_i = \frac{2}{(1 - \xi_i^2)[P_n'(\xi_i)]^2} \tag{3.39}$$

This equation is valid for the domain $\xi \in [-1, 1]$ as the zeros of the Legendre polynomials lie within this interval. For integration over different domains, a change of variables is necessary, and appropriate adjustments must be made to the formula for two-dimensional domains.

In the case of complex plate geometries, additional Gauss points are required, and a convergence study should be conducted. According to (JING; DUAN, 2023), determining the exact number of Gauss points in advance is challenging because the numerical integration of strain energy depends on the plate's geometry and deformation, influenced by its geometry, load, and boundary conditions.

3.5.1   Integrating in the Plate's Area

To integrate over the plate's area, the domain $(x, y) \in \left[-\frac{a}{2}, \frac{a}{2}\right] \times \left[-\frac{b}{2}, \frac{b}{2}\right]$ must be transformed into the domain $(\xi, \eta) \in [-1, 1]^2$. This transformation is achieved using the following equations:

$$x(\xi) = \frac{a\xi}{2} \quad \text{and} \quad y(\eta) = \frac{b\eta}{2} \tag{3.40}$$

The Jacobian of the transformation is given by:

$$J_1 = \begin{vmatrix} \dfrac{\partial x}{\partial \xi} & \dfrac{\partial y}{\partial \xi} \\ \dfrac{\partial x}{\partial \eta} & \dfrac{\partial y}{\partial \eta} \end{vmatrix} = \begin{vmatrix} \dfrac{a}{2} & 0 \\ 0 & \dfrac{b}{2} \end{vmatrix} = \frac{ab}{4} \tag{3.41}$$

To integrate a function $f(x, y)$ over the plate's area Ω_p, the integral is expressed as:

$$\int_{\Omega_p} f(x, y)\, d\Omega_p = \int_{-a/2}^{a/2} \int_{-b/2}^{b/2} f(x, y)\, dx\, dy = \frac{ab}{4} \int_{-1}^{1} \int_{-1}^{1} f(\xi, \eta)\, d\xi\, d\eta$$

$$\approx \frac{ab}{4} \sum_{p=1}^{\texttt{num\_int}_\xi} \sum_{q=1}^{\texttt{num\_int}_\eta} w_p w_q f(\xi_p, \eta_q) \tag{3.42}$$
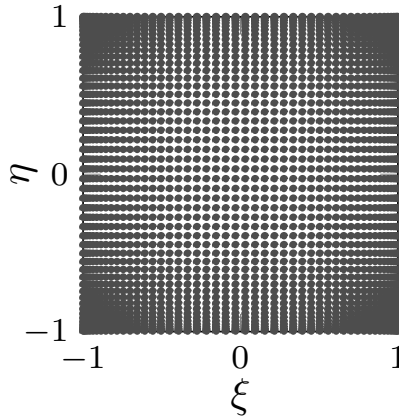
FIGURE 3.6 – Integration points along plate with $\texttt{num\_int}_\xi = \texttt{num\_int}_\eta = 50$.

3.5.2   Integrating in the Plate with Circular Cutout Area

To integrate over a plate with a cutout area, the domain $(x, y) \in \left[-\frac{a}{2}, \frac{a}{2}\right] \times \left[-\frac{b}{2}, \frac{b}{2}\right]$ must be transformed to the domain $(\xi, \eta) \in [-1, 1]^2$. This transformation is achieved using the following equations:

$$x(\xi) = \frac{a\xi}{2} \quad \text{and} \quad y(\eta) = \frac{b\eta}{2} \tag{3.43}$$

The Jacobian of this transformation is given by:

$$J_1 = \begin{vmatrix} \dfrac{\partial x}{\partial \xi} & \dfrac{\partial y}{\partial \xi} \\ \dfrac{\partial x}{\partial \eta} & \dfrac{\partial y}{\partial \eta} \end{vmatrix} = \begin{vmatrix} \dfrac{a}{2} & 0 \\ 0 & \dfrac{b}{2} \end{vmatrix} = \dfrac{ab}{4} \tag{3.44}$$

To integrate a function $f(x,y)$ over the domain Ω_c, which considers the effective area of the plate, i.e., excluding the cutout area, the procedure follows Eq. 3.45. In this case, the cutout is centered at the origin of the plate's coordinate system (x, y) and has a radius R. However, any type of restriction can be modeled for more complex cutouts. Note that the only difference compared to the case of the plate is that the points were appropriately selected within the domain Ω_c, excluding the cutout area.

$$\int_{\Omega_c} f(x,y)\, d\Omega_c = \frac{ab}{4} \int\int_{\Omega_c} f(\xi, \eta)\, d\xi\, d\eta \approx \begin{cases} \dfrac{ab}{4} \sum_{p=1}^{\texttt{num\_int}_\xi} \sum_{q=1}^{\texttt{num\_int}_\eta} w_p w_q f(\xi_p, \eta_q) \\ \text{subject to } \Omega_c : \left(\dfrac{\xi_p}{pd_1}\right)^2 + \left(\dfrac{\eta_q}{pd_2}\right)^2 > 1 \end{cases} \tag{3.45}$$

where $pd_1 = \frac{2R}{a}$ and $pd_2 = \frac{2R}{b}$.
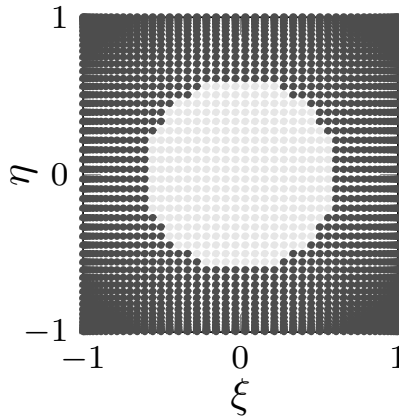
FIGURE 3.7 – Integration points for plate with a circular cutout with $\texttt{num\_int}_\xi = \texttt{num\_int}_\eta = 50$.

3.5.3 Integrating along the Stiffeners

For the case involving two stiffeners along the y-axis, a strategy similar to that employed for plates with cutouts is adopted, but integration is performed in only one dimension, η. The variables are transformed from the domain $y \in \left[-\frac{b}{2}, \frac{b}{2}\right]$ to the domain $\eta \in [-1, 1]$. After this transformation, the integration points along the η-axis corresponding to the locations of the stiffeners are conveniently selected in the domain Ω'_{st} of the stiffener.

For example, to calculate the integral of a function $f(x, y)$ along stiffeners located at $x = \pm x_s$, ranging from $y = -y_s$ to $y = y_s$, the transformations $\eta = \frac{2y}{b}$ and $\xi = \frac{2x}{a}$ must be applied, leading to:

$$\int_{-b/2}^{b/2} f(\pm x_s, y)\, dy = \frac{b}{2} \int_{-1}^{1} f(\pm \xi_s, \eta)\, d\eta \approx \frac{b}{2} \sum_{q=1}^{\texttt{num\_int}_\eta} w_q f(\pm \xi_s, \eta_q) \tag{3.46}$$

Selecting the points within the stiffener's domain yields Eq. 3.47.

$$\int_{\Omega'_{st}} f(\pm x_s, y)\, d\Omega'_{st} \approx \begin{cases} \frac{b}{2} \sum_{q=1}^{\texttt{num\_int}_\eta} w_q f(\pm \xi_s, \eta_q) \\ \text{subject to } \Omega'_{st} : \frac{-2y_s}{b} \leq \eta_q \leq \frac{2y_s}{b} \end{cases} \tag{3.47}$$
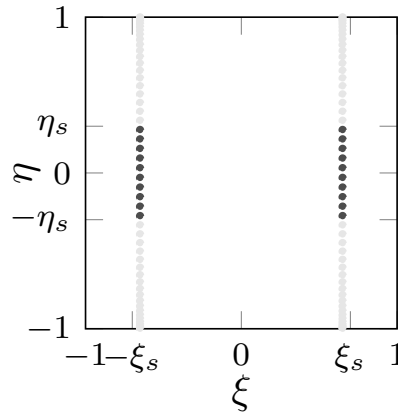
FIGURE 3.8 – Integration points along the stiffeners for $\texttt{num\_int}_\eta = 50$.

3.6 Prebuckling Analysis

To perform the prebuckling analysis, a procedure adopted by (NIMA; GANESAN, 2021) and (JING; DUAN, 2023) was followed, in which the distribution of membrane forces is solved using the Ritz method, a variational technique based on the principle of stationary total potential energy. In order to provide an overview of the procedure adopted in this analysis, a brief explanation of the procedure will be given, and throughout this section, the procedure will be detailed.

The potential energy of the orthotropic plate, as determined by the in-plane external forces, is given by:

$$\Pi_1 = U_m + U_m^s - U_F \tag{3.48}$$

where U_m is the strain energy stored in the plate, U_m^{s} represents the energy contributed by the stiffeners due to axial strain and bending around the z-axis and U_F is the potential energy of the applied forces.

The strain energy of a plate is given by:

$$U_m = \frac{1}{2} \int \int_{\Omega_c} \boldsymbol{\varepsilon}^T \begin{bmatrix} \mathbf{A} & \mathbf{B} \\ \mathbf{B} & \mathbf{D} \end{bmatrix} \boldsymbol{\varepsilon} \, dxdy + \int \int_{\Omega_c} \boldsymbol{\gamma}^T \mathbf{H} \boldsymbol{\gamma} \, dxdy \qquad (3.49)$$

where Ω_c is the domain corresponding to the effective area of the membrane.

As stated in (NIMA; GANESAN, 2021), when symmetrically stacked laminates are subjected only to in-plane forces, out-of-plane deflections are not expected. Consequently, the strain energies associated with bending and out-of-plane shearing become negligible, allowing for the reduction of the strain energy expression to:

$$U_m = \frac{1}{2} \int_{\Omega_c} (\boldsymbol{\varepsilon^0})^T \mathbf{A} \boldsymbol{\varepsilon^0} d\Omega \qquad (3.50)$$

The general form of the potential energy of boundary forces is:

$$U_F = \oint_{\Omega'} \overrightarrow{N} \cdot \overrightarrow{\Delta} \, d\Omega' \qquad (3.51)$$

where $\overrightarrow{N}$ is the traction vector on the boundary, $\overrightarrow{\Delta}$ is the displacement vector, and Ω' is the boundary contour on which the forces are being applied.

The functional Π_1 undergoes to first variation with respect to the unknown coefficients $\{c_{ij}^u, c_{ij}^v\}$. The resulting conditions for the stationary value of the total potential energy are represented as:

$$\frac{\partial \Pi_1}{\partial c_{ij}^u} = 0, \quad \frac{\partial \Pi_1}{\partial c_{ij}^v} = 0, \quad i = 1, 2, \ldots, I; \quad j = 1, 2, \ldots, J \qquad (3.52)$$

This derivation yields a system of linear equations. The coefficients c_{ij}^u and c_{ij}^v can be determined through the solution of this matrix-formulated linear system. After this, the values of u_0 and v_0 are obtained, and subsequently, the in-plane stresses $\bar{\mathbf{N}}$.

3.6.1 Strain Energy for a Plate
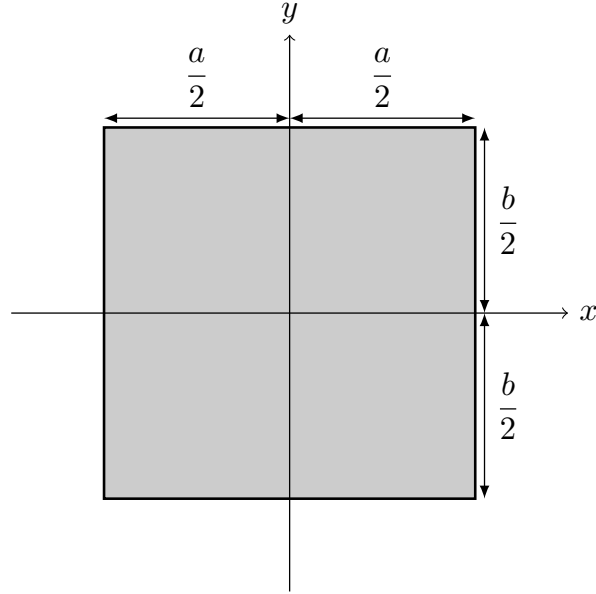
FIGURE 3.9 – Plate.

The strain energy of the plate is given by:

$$U_m = \frac{1}{2} \int_{-b/2}^{b/2} \int_{-a/2}^{a/2} (\boldsymbol{\varepsilon^0})^T \mathbf{A} \boldsymbol{\varepsilon^0} \, dx \, dy \tag{3.53}$$

To integrate over the plate's area, the domain $(x, y) \in [-a/2, a/2] \times [-b/2, b/2]$ must be transformed to the domain $(\xi, \eta) \in [-1, 1]^2$. This transformation is achieved by the following equations:

$$x(\xi) = \frac{a\xi}{2}, \quad y(\eta) = \frac{b\eta}{2} \tag{3.54}$$

The Jacobian of the transformation is:

$$J_1 = \begin{vmatrix} \dfrac{\partial x}{\partial \xi} & \dfrac{\partial y}{\partial \xi} \\ \dfrac{\partial x}{\partial \eta} & \dfrac{\partial y}{\partial \eta} \end{vmatrix} = \begin{vmatrix} \dfrac{a}{2} & 0 \\ 0 & \dfrac{b}{2} \end{vmatrix} = \frac{ab}{4} \tag{3.55}$$

Thus, the strain energy U_m in the transformed domain is:

$$U_m = \frac{1}{2} \int_{-1}^{1} \int_{-1}^{1} (\boldsymbol{\varepsilon^0})^T \mathbf{A} \boldsymbol{\varepsilon^0} \, |J_1| \, d\xi \, d\eta = \frac{ab}{8} \int_{-1}^{1} \int_{-1}^{1} (\boldsymbol{\varepsilon^0})^T \mathbf{A} \boldsymbol{\varepsilon^0} \, d\xi \, d\eta \tag{3.56}$$

It is important to note the need for a variable change in the integrand, as described in Eq. 3.57. Additionally, when dealing with a VAT laminate, a variable change would also be necessary in the values of $A_{ij}(x, y)$.

$$(\boldsymbol{\varepsilon^0})^T = \left[\frac{\partial u_0}{\partial \xi} \frac{\partial \xi}{\partial x} \quad \frac{\partial v_0}{\partial \eta} \frac{\partial \eta}{\partial y} \quad \left(\frac{\partial u_0}{\partial \eta} \frac{\partial \eta}{\partial y} + \frac{\partial v_0}{\partial \xi} \frac{\partial \xi}{\partial x} \right) \right] \tag{3.57}$$

Moreover, algebraic manipulation of the values of U_m was performed to isolate the calculation of integrals involving only the multiplication of trial shape functions and their derivatives in the formulations. Thus, with just a single set of integrations, U_m can be determined for other dimensions $a \times b$ and various values of A_{ij} for $i, j = 1, 2, 6$.

This approach facilitates a broad range of simulations with reduced computational cost, as the integral calculations constitute the most computationally demanding aspect of the prebuckling and buckling analysis process. This strategy will be applied to all subsequent potential energy calculations across all configurations, including the plate, the plate with a cutout, and the stiffened plate with a cutout.

3.6.2 Strain Energy for a Plate with Circular Cutout
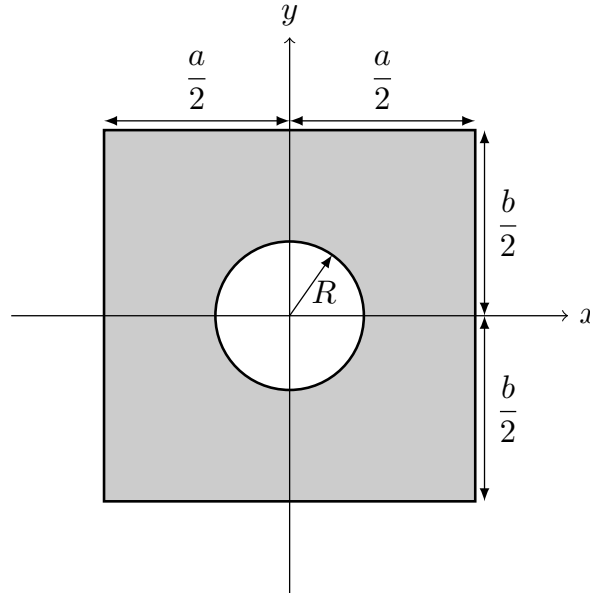
FIGURE 3.10 – Plate with circular cutout.

The strain energy for a plate with a circular cutout is given by Eq. 3.58. To calculate the integral of the strain energy for a plate with a circular cutout, the same integration limits as for the plate are used. However, the integration condition is applied only to the region outside the circular cutout.

$$U_m = \frac{1}{2} \int \int_{\Omega_c} (\boldsymbol{\varepsilon^0})^T \mathbf{A} \boldsymbol{\varepsilon^0} |J_1| d\xi d\eta = \begin{cases} \frac{ab}{8} \int_{-1}^{1} \int_{-1}^{1} (\boldsymbol{\varepsilon^0})^T \mathbf{A} \boldsymbol{\varepsilon^0} d\xi d\eta \\ \text{subject to } \Omega_c : \left(\frac{\xi}{pd_1}\right)^2 + \left(\frac{\eta}{pd_2}\right)^2 > 1 \end{cases} \quad (3.58)$$

where $pd_1 = \frac{2R}{a}$ and $pd_2 = \frac{2R}{b}$.

3.6.3 Strain Energy for a Plate with Circular Cutout and Stiffeners

In the case illustrated in Figure 3.11, the stiffener is not directly affected by any external force; instead, the plate is the sole component subjected to loading. Consequently, the stiffener's contribution to the rigidity of the panel is solely through its elastic strain energy. For simplification, the flanges are modeled as beam elements along the midplane, employing the kinematics formulation of the Euler-Bernoulli Beam Theory as utilized in (YOO; LEE, 2011) and (SILVA, 2021). These beam elements share the same displacements as the plate element. The current formulation of the stiffener's strain energy accounts for energy due to axial strain, bending around the x and z axes, and torsion (SILVA, 2021).
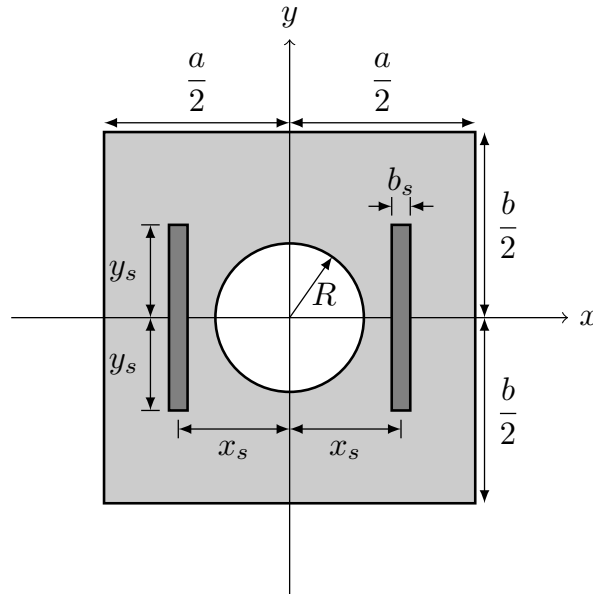
FIGURE 3.11 – Plate with circular cutout and two stiffeners parallel to the y direction.

For stiffeners positioned parallel to the y-axis, along the lines $x = \pm x_s$, ranging from $-y_s$ to y_s (i.e., with length $l_s = 2y_s$), in the prebuckling analysis, the potential energy of each stiffener accounts for energy due to axial strain and bending around the z-axis. In accordance with (YOO; LEE, 2011) and (SILVA, 2021), for each stiffener located at $\pm x_s$:

$$U_m^{\text{axial}(s)} = \frac{1}{2} \int_{-y_s}^{y_s} E_y^s A_{st} \left(\frac{\partial v_0(\pm x_s, y)}{\partial y} \right)^2 dy \tag{3.59}$$

$$U_m^{\text{bending } z(s)} = \frac{1}{2} \int_{-y_s}^{y_s} E_y^s I_{zz} \left(\frac{\partial^2 u_0(\pm x_s, y)}{\partial y^2} \right)^2 dy \tag{3.60}$$

where A_{st} is the cross-sectional area of the stiffener in the x-z plane, E_y^s is the effective elasticity modulus of the stiffener positioned in the y-axis direction, and I_{zz} is the moment of inertia about the z-axis.
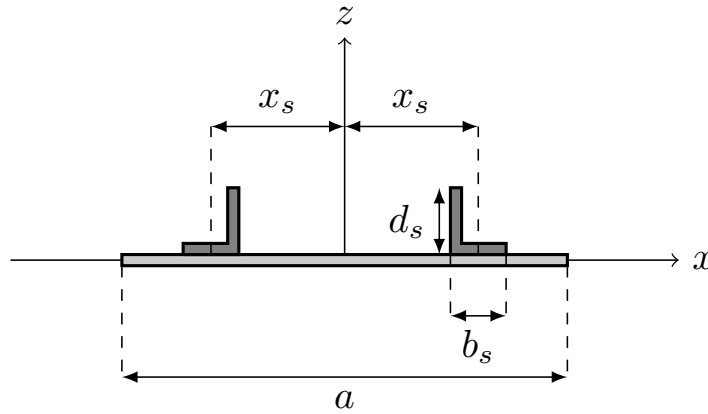
FIGURE 3.12 – Plate with circular cutout and two stiffeners parallel to the y direction (xz view).

Performing the change of variables, for each stiffener located at $\pm \xi_s$:

$$U_m^{\text{axial}(s)} = \frac{E_y^s A_{st}}{b} \int_{-\frac{2y_s}{b}}^{\frac{2y_s}{b}} \left(\frac{\partial v_0(\pm \xi_s, \eta)}{\partial \eta} \right)^2 d\eta \tag{3.61}$$

$$U_m^{\text{bending } z(s)} = \frac{4 E_y^s I_{zz}}{b^3} \int_{-\frac{2y_s}{b}}^{\frac{2y_s}{b}} \left(\frac{\partial^2 u_0(\pm \xi_s, \eta)}{\partial \eta^2} \right)^2 d\eta \tag{3.62}$$

Considering two stiffeners arranged along the y-axis, the potential energy related to axial forces and bending around the z-axis is given by the following equation.

$$U_m^s = U_m^{\text{axial}(s_1)} + U_m^{\text{axial}(s_2)} + U_m^{\text{bending } z(s_1)} + U_m^{\text{bending } z(s_2)} \tag{3.63}$$

Furthermore, in Appendix A (Stiffeners' Parameters), the methodology used to obtain the parameters E_y^s, I_{zz}, and A_{st} can be verified.

3.6.4   Potential of the External Loads

The general form of the potential energy of boundary forces is:

$$U_F = \oint_{\Omega'} \vec{N} \cdot \vec{\Delta} \, d\Omega'$$

(3.64)

For the special case of a rectangular plate of dimensions $a \times b$ under biaxial and shear distributed loading, Eq. 3.64 is applied to the plate geometry and can be represented by Eq. 3.65.

$$U_F = \int_{-b/2}^{b/2} \{N_x u_{(x=a/2)} - N_x u_{(x=-a/2)}\} dy + \int_{-a/2}^{a/2} \{N_y v_{(y=b/2)} - N_y v_{(y=-b/2)}\} dx$$
$$+ \int_{-a/2}^{a/2} \{N_{xy} u_{(y=b/2)} - N_{xy} u_{(y=-b/2)}\} dx + \int_{-b/2}^{b/2} \{N_{xy} v_{(x=a/2)} - N_{xy} v_{(x=-a/2)}\} dy$$

(3.65)

The domain $(x, y) \in \left[-\frac{a}{2}, \frac{a}{2}\right] \times \left[-\frac{b}{2}, \frac{b}{2}\right]$ must be changed to the domain $(\xi, \eta) \in [-1, 1]^2$. This is achieved by making the following transformation:

$$U_F = \frac{b}{2} \int_{-1}^{1} \{N_x u_{(\xi=1)} - N_x u_{(\xi=-1)}\} d\eta + \frac{a}{2} \int_{-1}^{1} \{N_y v_{(\eta=1)} - N_y v_{(\eta=-1)}\} d\xi$$
$$+ \frac{a}{2} \int_{-1}^{1} \{N_{xy} u_{(\eta=1)} - N_{xy} u_{(\eta=-1)}\} d\xi + \frac{b}{2} \int_{-1}^{1} \{N_{xy} v_{(\xi=1)} - N_{xy} v_{(\xi=-1)}\} d\eta$$

(3.66)

3.6.5   Stationary Value of the Total Potential Energy for the Prebuckling Problem

To obtain the stationary value of total potential energy and without loss of generality, an illustrative example will be presented for a stiffened plate with a circular cutout. This example represents the general case and is described by the energy functional in Eq. 3.67.

$$\Pi_1 = U_m + U_m^s - U_F$$

(3.67)

Upon substituting the displacement terms u_0 and v_0, represented by their trial function shapes into Eqs. 3.58, 3.63, and 3.66, which correspond to the calculations of U_m, U_m^s, and U_F respectively, and further integrating the outcomes into Eq. 3.67, the functional Π_1 undergoes to first variation with respect to the unknown coefficients $\{c_{ij}^u, c_{ij}^v\}$. The resulting conditions for the stationary value of the total potential energy are represented as:

$$\frac{\partial \Pi_1}{\partial c_{ij}^u} = 0, \quad \frac{\partial \Pi_1}{\partial c_{ij}^v} = 0, \quad i = 1, 2, \ldots, I; \quad j = 1, 2, \ldots, J \tag{3.68}$$

This derivation yields a system of linear equations. The coefficients c_{ij}^u and c_{ij}^v can be determined through the solution of this matrix-formulated linear system, elucidated as follows:

$$\begin{bmatrix} c_{ij}^u \\ c_{ij}^v \end{bmatrix} = (\mathbf{K}_m + \mathbf{K}_m^s)^{-1}\mathbf{W}, \quad i = 1, 2, \ldots, I; \quad j = 1, 2, \ldots, J \tag{3.69}$$

where $\mathbf{K}_m$ represents the membrane stiffness matrix derived from Eq. 3.58, $\mathbf{K}_m^s$ represents the energy contributed by the stiffeners due to axial strain and bending around the z-axis, as derived from Eq. 3.63, and $\mathbf{W}$ is a vector determined by the load potential energy from Eq. 3.66.

The matrix $\mathbf{K}_m$ is represented by Eq. 3.70.

$$\mathbf{K}_m = \begin{bmatrix} \mathbf{K}_{uu} & \mathbf{K}_{uv} \\ \mathbf{K}_{uv}^T & \mathbf{K}_{vv} \end{bmatrix} \tag{3.70}$$

The elements of $\mathbf{K}_m$ are computed as follows:

$$\mathbf{K}_{uu} = \left\{ A_{11}\mathbf{I}^{1010}\left(\frac{b}{a}\right) + A_{66}\mathbf{I}^{0101}\left(\frac{a}{b}\right) + A_{16}\left(\mathbf{I}^{0110} + \mathbf{I}^{1001}\right) \right\}_{uu} \tag{3.71}$$

$$\mathbf{K}_{uv} = \left\{ A_{16}\mathbf{I}^{1010}\left(\frac{b}{a}\right) + A_{26}\mathbf{I}^{0101}\left(\frac{a}{b}\right) + A_{66}\mathbf{I}^{0110} + A_{12}\mathbf{I}^{1001} \right\}_{uv} \tag{3.72}$$

$$\mathbf{K}_{vv} = \left\{ A_{66}\mathbf{I}^{1010}\left(\frac{b}{a}\right) + A_{22}\mathbf{I}^{0101}\left(\frac{a}{b}\right) + A_{26}\left(\mathbf{I}^{0110} + \mathbf{I}^{1001}\right) \right\}_{vv} \tag{3.73}$$

where

$$\mathbf{I}_{rs}^{defg} = \iint_{\Omega_c} \frac{\partial^{d+e}[\mathbf{f}^r(\xi,\eta)]^T}{\partial\xi^d\partial\eta^e} \cdot \frac{\partial^{f+g}\mathbf{f}^s(\xi,\eta)}{\partial\xi^f\partial\eta^g}\, d\xi\, d\eta \quad \{r,s\} \in \{u,v,w,\varphi_u,\varphi_v\} \tag{3.74}$$

The elements of $\mathbf{K}_m^s$ for the two stiffeners along the η axis are computed as follows:

$$\mathbf{K}_m^s = \begin{bmatrix} \mathbf{K}_{uu}^s & \mathbf{K}_{uv}^s \\ (\mathbf{K}_{uv}^s)^T & \mathbf{K}_{vv}^s \end{bmatrix} \tag{3.75}$$

where

$$\mathbf{K}_{uu}^s = \frac{8E_y^s I_{zz}}{b^3} \int_{-\frac{2y_s}{b}}^{\frac{2y_s}{b}} \left[\mathbf{f}_{,\eta\eta}^u(-\xi_s,\eta)\right]^T \left[\mathbf{f}_{,\eta\eta}^u(-\xi_s,\eta)\right] d\eta + \tag{3.76}$$

$$+ \frac{8E_y^s I_{zz}}{b^3} \int_{-\frac{2y_s}{b}}^{\frac{2y_s}{b}} \left[\mathbf{f}_{,\eta\eta}^u(\xi_s,\eta)\right]^T \left[\mathbf{f}_{,\eta\eta}^u(\xi_s,\eta)\right] d\eta \tag{3.77}$$

$$\mathbf{K}_{uv}^s = \mathbf{0} \tag{3.78}$$

$$\mathbf{K}_{vv}^s = \frac{2E_y^s A_{st}}{b} \int_{-\frac{2y_s}{b}}^{\frac{2y_s}{b}} \left[\mathbf{f}_{,\eta}^v(-\xi_s,\eta)\right]^T \left[\mathbf{f}_{,\eta}^v(-\xi_s,\eta)\right] d\eta + \tag{3.79}$$

$$+ \frac{2E_y^s A_{st}}{b} \int_{-\frac{2y_s}{b}}^{\frac{2y_s}{b}} \left[\mathbf{f}_{,\eta}^v(\xi_s,\eta)\right]^T \left[\mathbf{f}_{,\eta}^v(\xi_s,\eta)\right] d\eta \tag{3.80}$$

where $\mathbf{f}_{,\varpi}^p$ represents the first-order partial derivative of $\mathbf{f}^p$ with respect to ϖ and $\mathbf{f}_{,\varpi\varrho}^p$ represents the second-order partial derivative with respect to the variables ϖ and ϱ.

The matrix $\mathbf{W}$ depends on the loading condition. Therefore, in the case of pure shear N_{xy}, for example:

$$U_F = \frac{a}{2} \int_{-1}^1 \{N_{xy}u_{(\eta=1)} - N_{xy}u_{(\eta=-1)}\}d\xi + \frac{b}{2} \int_{-1}^1 \{N_{xy}v_{(\xi=1)} - N_{xy}v_{(\xi=-1)}\}d\eta$$

$$U_F = \left(\frac{N_{xy}a}{2}\mathbf{c}^u\right) \int_{-1}^1 \left([\mathbf{f}^u(\xi,1)]^T - [\mathbf{f}^u(\xi,-1)]^T\right) d\xi +$$

$$+ \left(\frac{N_{xy}b}{2}\mathbf{c}^v\right) \int_{-1}^1 \left([\mathbf{f}^v(1,\eta)]^T - [\mathbf{f}^v(-1,\eta)]^T\right) d\eta \tag{3.81}$$

Taking the first variation of U_F with respect to c_{ij}^u and c_{ij}^v, the matrix $\mathbf{W}$ is obtained.

$$\mathbf{W} = \begin{bmatrix} \mathbf{W}_u \\ \mathbf{W}_v \end{bmatrix} \tag{3.82}$$

$\mathbf{W}_u$ has dimension of $I \times J$ terms:

$$\mathbf{W}_u = \frac{a}{2} \int_{-1}^1 \begin{bmatrix} \chi_1^u(\xi)\chi_1^u(\eta)|_{\eta=1} - \chi_1^u(\xi)\chi_1^u(\eta)|_{\eta=-1} \\ \chi_1^u(\xi)\chi_2^u(\eta)|_{\eta=1} - \chi_1^u(\xi)\chi_2^u(\eta)|_{\eta=-1} \\ \cdots \\ \chi_I^u(\xi)\chi_J^u(\eta)|_{=1} - \chi_I^u(\xi)\chi_J^u(\eta)|_{\eta=-1} \end{bmatrix} d\xi \tag{3.83}$$

$\mathbf{W}_v$ also has dimension of $I \times J$ terms:

$$\mathbf{W}_v = \frac{b}{2} \int_{-1}^{1} \begin{bmatrix} \chi_1^v(\xi)\chi_1^v(\eta)|_{\xi=1} - \chi_1^v(\xi)\chi_1^v(\eta)|_{\xi=-1} \\ \chi_1^v(\xi)\chi_2^v(\eta)|_{\xi=1} - \chi_1^v(\xi)\chi_2^v(\eta)|_{\xi=-1} \\ \dots \\ \chi_I^v(\xi)\chi_J^v(\eta)|_{\xi=1} - \chi_I^v(\xi)\chi_J^v(\eta)|_{\xi=-1} \end{bmatrix} d\eta \tag{3.84}$$

Following the methodology employed in (JING; DUAN, 2023), the in-plane displacements u_0 and v_0 are derived by substituting c_{ij}^u and c_{ij}^v into Equations 3.32 and 3.33. Subsequently, u_0 and v_0 are utilized to determine the in-plane strain $\boldsymbol{\varepsilon}^{\mathbf{0}}$, discarding the effects of curvatures $\boldsymbol{\kappa}$ and von Kármán strains $\tilde{\boldsymbol{\varepsilon}}$.

By substituting $\boldsymbol{\varepsilon}^{\mathbf{0}}$ into Eq. 3.85 and disregarding the matrices $\mathbf{B}$, $\mathbf{D}$, and $\mathbf{H}$, the in-plane stress resultants $\overline{\mathbf{N}} = \{\overline{N}_x, \overline{N}_y, \overline{N}_{xy}\}^T$ are identified, as shown in Eq. 3.86.

$$\begin{Bmatrix} \mathbf{N} \\ \mathbf{M} \\ \mathbf{S} \end{Bmatrix} = \begin{bmatrix} \mathbf{A} & \mathbf{B} & \mathbf{0} \\ \mathbf{B} & \mathbf{D} & \mathbf{0} \\ \mathbf{0} & \mathbf{0} & \mathbf{H} \end{bmatrix} \begin{Bmatrix} \boldsymbol{\varepsilon}^{\mathbf{0}} \\ \boldsymbol{\kappa} \\ \boldsymbol{\gamma} \end{Bmatrix} \tag{3.85}$$

$$\overline{N}_x = 2\left[A_{16}E_{01}^u/b + A_{12}E_{01}^v/b + A_{11}E_{10}^u/a + A_{16}E_{10}^v/a\right]$$
$$\overline{N}_y = 2\left[A_{26}E_{01}^u/b + A_{22}E_{01}^v/b + A_{12}E_{10}^u/a + A_{26}E_{10}^v/a\right]$$
$$\overline{N}_{xy} = 2\left[A_{66}E_{01}^u/b + A_{26}E_{01}^v/b + A_{16}E_{10}^u/a + A_{66}E_{10}^v/a\right] \tag{3.86}$$

where

$$E_{pq}^u(\xi,\eta) = \frac{\partial^{p+q}u_0(\xi,\eta)}{\partial\xi^p\partial\eta^q}, \quad E_{pq}^v(\xi,\eta) = \frac{\partial^{p+q}v_0(\xi,\eta)}{\partial\xi^p\partial\eta^q}, \quad \{p,q\} \in \{0,1\} \tag{3.87}$$

As illustrated, $\overline{\mathbf{N}} = \left\{\overline{N}_x, \overline{N}_y, \overline{N}_{xy}\right\}^T$ emerges as a function of coordinates ξ and η, determined by the in-plane stiffness A_{ij} (i, j = 1, 2, 6), boundary conditions, and the applied in-plane loads. Furthermore, the diagram of the implementation used in prebuckling analysis can be verified, as shown in Figure 3.13.
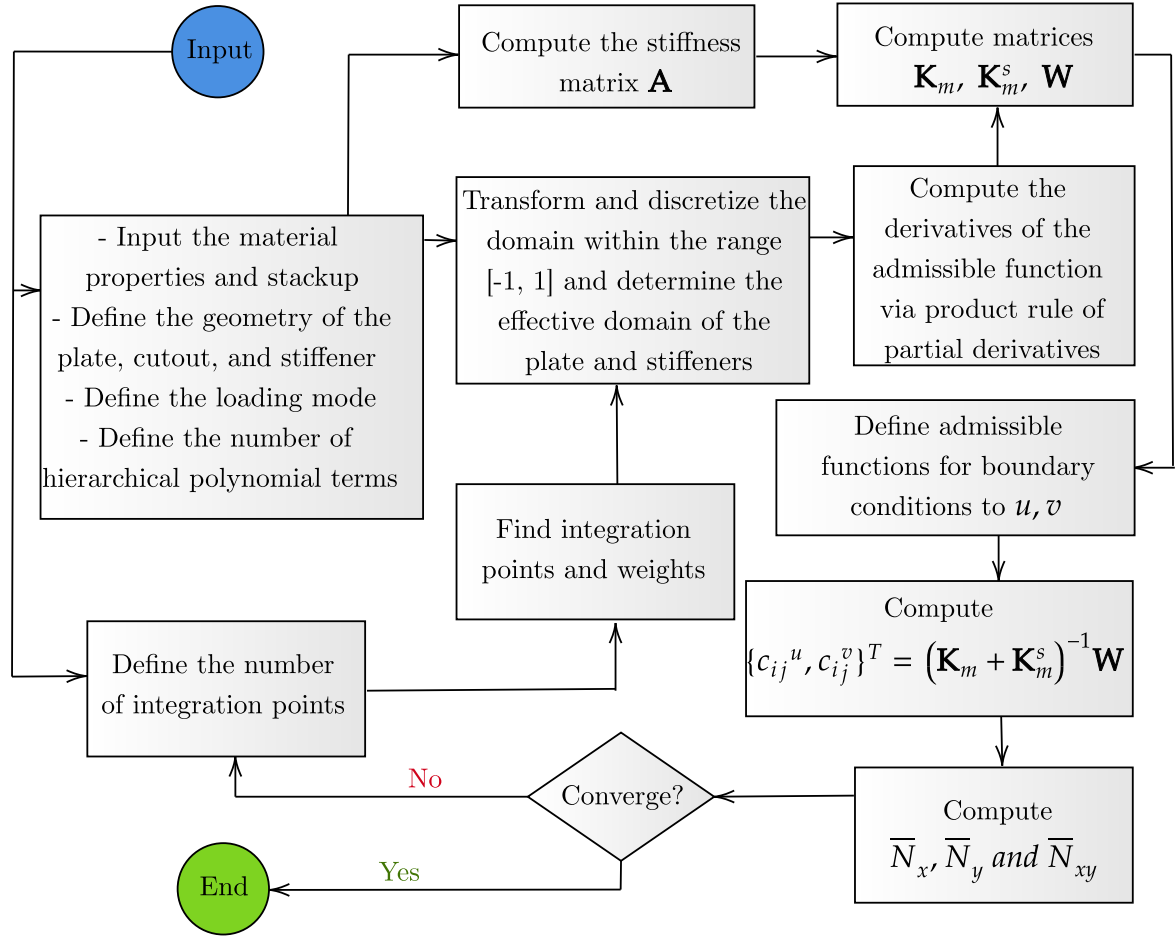
FIGURE 3.13 – Diagram of the implementation used in prebuckling analysis.

3.7   Buckling Analysis

Following the methodology adopted by (JING; DUAN, 2023), the buckling analysis of orthotropic plates is driven by in-plane stress resultants $\overline{\mathbf{N}}$ identified during the prebuckling phase. This analysis integrates the stress stiffening energy into the total potential energy. Additionally, the functional Π_2 must incorporate the contributions from the out-of-plane energy of the stiffeners and the bending energy of the plate. This relationship is expressed as:

$$\Pi_2 = U_b + U_b^s - U_N \tag{3.88}$$

where U_b represents the out-of-plane bending energy of the plate, U_b^s denotes the out-of-plane bending and torsion energy of the stiffeners, and U_N corresponds to the stress stiffening energy derived from the prebuckling analysis. The detailed calculations of these contributions will be presented later in this section.

3.7.1 Stress Stiffening Energy

The stress stiffening energy, U_N, associated with the von Kármán strains, $\tilde{\boldsymbol{\varepsilon}}$, and $\overline{\mathbf{N}}$, derived from the in-plane stresses obtained during the prebuckling analysis, is expressed by the following equation:

$$U_N = \int\int_{\Omega_c} \overline{\mathbf{N}}^T \tilde{\boldsymbol{\varepsilon}} |J_1|\, d\xi\, d\eta = \frac{ab}{4} \int\int_{\Omega_c} \overline{\mathbf{N}}^T \tilde{\boldsymbol{\varepsilon}}\, d\xi\, d\eta \tag{3.89}$$

where $\overline{\mathbf{N}} = \{\overline{N}_x, \overline{N}_y, \overline{N}_{xy}\}^T$ represents the in-plane stress resultants and $\tilde{\boldsymbol{\varepsilon}}$ represents the von Kármán strains and they are identified by the following equations.

$$\overline{N}_x = 2\left[A_{16}E_{01}^u/b + A_{12}E_{01}^v/b + A_{11}E_{10}^u/a + A_{16}E_{10}^v/a\right] \tag{3.90}$$

$$\overline{N}_y = 2\left[A_{26}E_{01}^u/b + A_{22}E_{01}^v/b + A_{12}E_{10}^u/a + A_{26}E_{10}^v/a\right] \tag{3.91}$$

$$\overline{N}_{xy} = 2\left[A_{66}E_{01}^u/b + A_{26}E_{01}^v/b + A_{16}E_{10}^u/a + A_{66}E_{10}^v/a\right] \tag{3.92}$$

where

$$E_{pq}^u(\xi,\eta) = \frac{\partial^{p+q}u_0(\xi,\eta)}{\partial\xi^p\partial\eta^q}, \quad E_{pq}^v(\xi,\eta) = \frac{\partial^{p+q}v_0(\xi,\eta)}{\partial\xi^p\partial\eta^q}, \quad \{p,q\} \in \{0,1\} \tag{3.93}$$

and

$$\tilde{\boldsymbol{\varepsilon}}^T = \begin{bmatrix} \tilde{\varepsilon}_x & \tilde{\varepsilon}_y & \tilde{\gamma}_{xy} \end{bmatrix} = \begin{bmatrix} \frac{1}{2}\left(\frac{\partial w_0}{\partial\xi}\frac{\partial\xi}{\partial x}\right)^2 & \frac{1}{2}\left(\frac{\partial w_0}{\partial\eta}\frac{\partial\eta}{\partial y}\right)^2 & \frac{\partial w_0}{\partial\xi}\frac{\partial\xi}{\partial x}\frac{\partial w_0}{\partial\eta}\frac{\partial\eta}{\partial y} \end{bmatrix} \tag{3.94}$$

Furthermore, the integral is defined over the effective area of the plate within the domain Ω_c. That is, if there are any cutouts present in the plate, the area represented by the cutouts is not included in the calculation. Note also that the buckling analysis is interconnected with the prebuckling analysis through this equation.

3.7.2 The Out-of-Plane Bending Energy for a Plate

The out-of-plane bending energy U_b stored within the orthotropic plate is quantified by:

$$U_b = \frac{1}{2}\int_{-1}^{1}\int_{-1}^{1} \boldsymbol{\kappa}^T \boldsymbol{D}\boldsymbol{\kappa}|J_1|\, d\xi\, d\eta + \frac{1}{2}\int_{-1}^{1}\int_{-1}^{1} \boldsymbol{\gamma}^T \mathbf{H}\boldsymbol{\gamma}|J_1|\, d\xi\, d\eta \tag{3.95}$$

For instance, for a plate with dimensions $a \times b$:

$$U_b = \frac{ab}{8} \int_{-1}^{1} \int_{-1}^{1} \boldsymbol{\kappa}^T \mathbf{D} \boldsymbol{\kappa} \, d\xi \, d\eta + \frac{ab}{8} \int_{-1}^{1} \int_{-1}^{1} \boldsymbol{\gamma}^T \mathbf{H} \boldsymbol{\gamma} \, d\xi \, d\eta \qquad (3.96)$$

where

$$\boldsymbol{\kappa}^T = \left[\frac{\partial \varphi_u}{\partial \xi} \frac{\partial \xi}{\partial x} \quad \frac{\partial \varphi_v}{\partial \eta} \frac{\partial \eta}{\partial y} \quad \left(\frac{\partial \varphi_u}{\partial \eta} \frac{\partial \eta}{\partial y} + \frac{\partial \varphi_v}{\partial \xi} \frac{\partial \xi}{\partial x} \right) \right] \qquad (3.97)$$

and

$$\boldsymbol{\gamma}^T = \left[\left(\varphi_v + \frac{\partial w_0}{\partial \eta} \frac{\partial \eta}{\partial y} \right) \quad \left(\varphi_u + \frac{\partial w_0}{\partial \xi} \frac{\partial \xi}{\partial x} \right) \right] \qquad (3.98)$$

3.7.3   The Out-of-Plane Bending Energy for a Plate with a Circular Cutout

Similar to the plate, the out-of-plane bending energy U_b stored within the orthotropic plate with a circular cutout is quantified in its domain Ω_c by:

$$U_b = \frac{1}{2} \int \int_{\Omega_c} \boldsymbol{\kappa}^T \mathbf{D} \boldsymbol{\kappa} |J_1| \, d\xi \, d\eta + \frac{1}{2} \int \int_{\Omega_c} \boldsymbol{\gamma}^T \mathbf{H} \boldsymbol{\gamma} |J_1| \, d\xi \, d\eta \qquad (3.99)$$

For instance, for a plate with dimensions $a \times b$, containing a cutout:

$$U_b = \frac{ab}{8} \int \int_{\Omega_c} \boldsymbol{\kappa}^T \mathbf{D} \boldsymbol{\kappa} \, d\xi \, d\eta + \frac{ab}{8} \int \int_{\Omega_c} \boldsymbol{\gamma}^T \mathbf{H} \boldsymbol{\gamma} \, d\xi \, d\eta \qquad (3.100)$$

Thus, a conditional integration is performed, as explained earlier, according to Eqs. 3.101 and 3.102.

$$\frac{ab}{8} \int \int_{\Omega_c} \boldsymbol{\kappa}^T \mathbf{D} \boldsymbol{\kappa} \, d\xi \, d\eta = \begin{cases} \frac{ab}{8} \int_{-1}^{1} \int_{-1}^{1} \boldsymbol{\kappa}^T \mathbf{D} \boldsymbol{\kappa} \, d\xi \, d\eta \\ \text{subject to } \Omega_c : \left(\frac{\xi}{pd_1} \right)^2 + \left(\frac{\eta}{pd_2} \right)^2 > 1 \end{cases} \qquad (3.101)$$

$$\frac{ab}{8} \int \int_{\Omega_c} \boldsymbol{\gamma}^T \mathbf{H} \boldsymbol{\gamma} \, d\xi \, d\eta = \begin{cases} \frac{ab}{8} \int_{-1}^{1} \int_{-1}^{1} \boldsymbol{\gamma}^T \mathbf{H} \boldsymbol{\gamma} \, d\xi \, d\eta \\ \text{subject to } \Omega_c : \left(\frac{\xi}{pd_1} \right)^2 + \left(\frac{\eta}{pd_2} \right)^2 > 1 \end{cases} \qquad (3.102)$$

where $pd_1 = \frac{2R}{a}$ and $pd_2 = \frac{2R}{b}$.

3.7.4 The Out-of-Plane Bending and Torsion Energy for a Stiffened Plate with a Circular Cutout
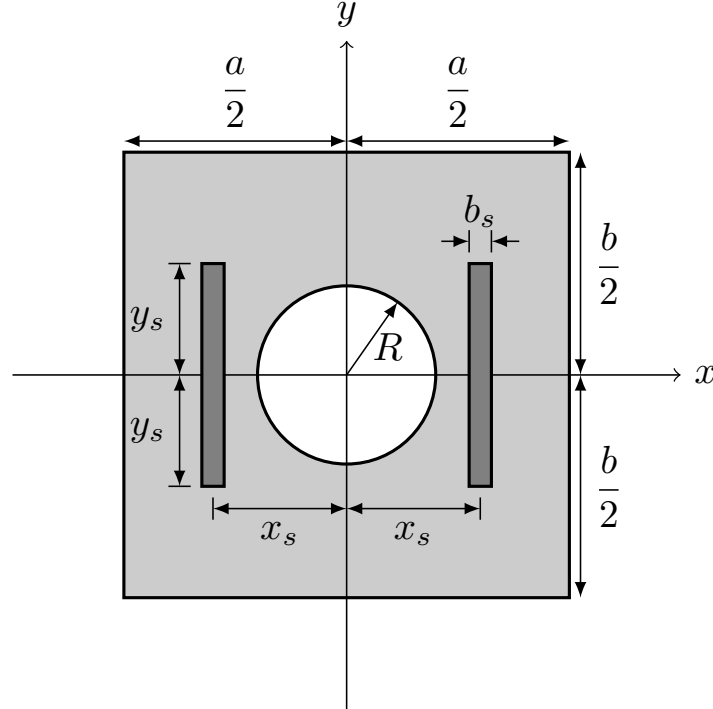
FIGURE 3.14 – Plate with circular cutout and two stiffeners parallel to the y direction.

According to (YOO; LEE, 2011), the strain energy stored in a beam consists of the following components, while neglecting the minor contributions of the bending shear strain energy and the warping shear strain energy: the energies due to bending in the x- and z-directions; the energy due to Saint-Venant shear stress; and the energy due to warping torsion.

In the prebuckling analysis, the energies related to axial loading and bending in the z-direction due to the stiffeners were calculated. Now, in the buckling analysis, the out-of-plane bending and torsion energy originating from the stiffeners will be considered, which can be represented by the following equations:

$$U_b^{\text{bending } x(s)} = \frac{1}{2} \int_{-y_s}^{y_s} E_y^s I_{xx} \left(\frac{\partial^2 w_0(\pm x_s, y)}{\partial y^2} \right)^2 dy \tag{3.103}$$

$$U_b^{\text{venant}(s)} = \frac{1}{2} \int_{-y_s}^{y_s} G_{xz}^s J \left(\frac{\partial \beta}{\partial y} \right)^2 dy \tag{3.104}$$

$$U_b^{\text{warping}(s)} = \frac{1}{2} \int_{-y_s}^{y_s} E_y^s \Gamma \left(\frac{\partial^2 \beta}{\partial y^2} \right)^2 dy \tag{3.105}$$

where β is the rotation angle due to twisting in the $x - z$ plane around the shear center, as shown in Figure 3.15, I_{xx} is the moment of inertia about the x-axis, E_y^s is the effective elasticity modulus of the stiffener in the y-axis direction, G_{xz}^s is the effective shear modulus in the $x - z$ plane of the stiffener, J is the Saint-Venant torsional constant of the stiffener, and Γ is the warping torsional constant of the stiffener.
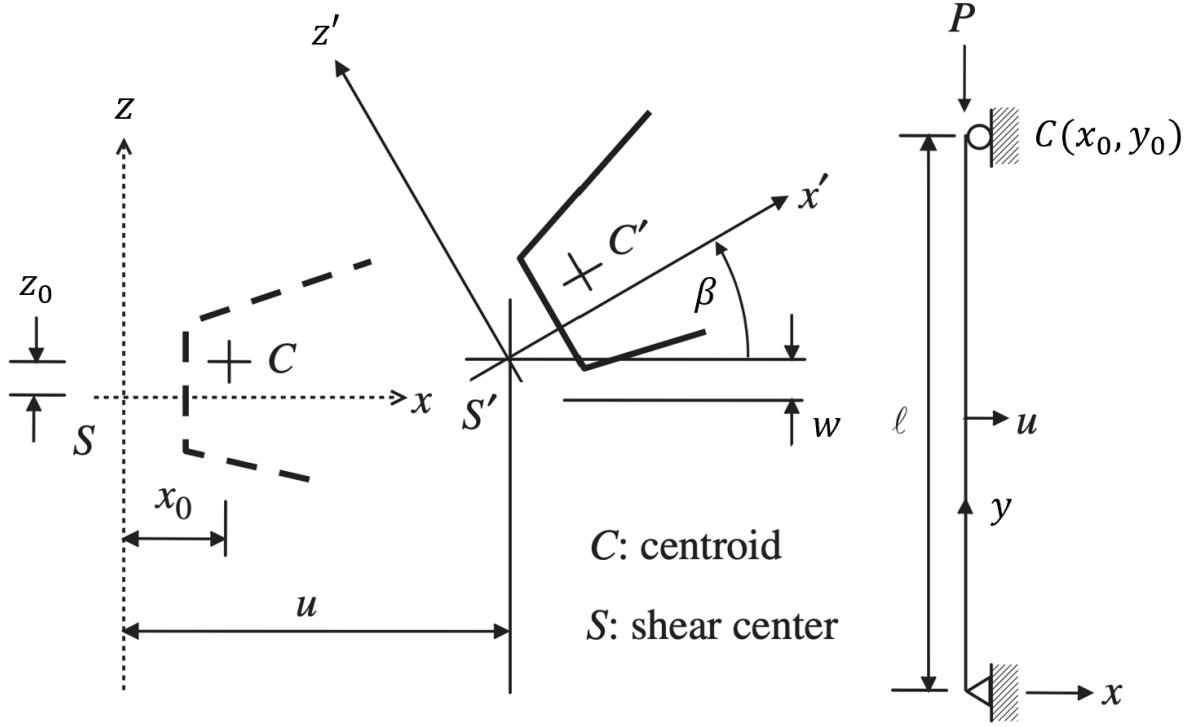
FIGURE 3.15 – Representative figure of the flexural-torsional buckling deformation acting on the stiffeners, modeled as beam elements. Source: Adapted from (YOO; LEE, 2011).

Assuming small rotations, the following simplification is made, as adopted by (SILVA, 2021).

$$\beta \approx \left(\frac{\partial w_0}{\partial x} \right) \tag{3.106}$$

Thus, the equations related to Saint-Venant shear stress and the energy due to warping torsion were simplified as shown in the equations below.

$$U_b^{\text{venant}(s)} = \frac{1}{2} \int_{-y_s}^{y_s} G_{xz}^s J \left(\frac{\partial^2 w_0(\pm x_s, y)}{\partial x \partial y} \right)^2 dy \tag{3.107}$$

$$U_b^{\text{warping}(s)} = \frac{1}{2} \int_{-y_s}^{y_s} E_y^s \Gamma \left(\frac{\partial^3 w_0(\pm x_s, y)}{\partial y^2 \partial x} \right)^2 dy \tag{3.108}$$

Performing the change of coordinates and substitution of partial derivatives:

$$U_b^{\text{bending } x^{(s)}} = \frac{4E_y^s I_{xx}}{b^3} \int_{-\frac{2y_s}{b}}^{\frac{2y_s}{b}} \left(\frac{\partial^2 w_0(\pm\xi_s, \eta)}{\partial \eta^2} \right)^2 d\eta \tag{3.109}$$

$$U_b^{\text{venant}(s)} = \frac{4G_{xz}^s J}{a^2 b} \int_{-\frac{2y_s}{b}}^{\frac{2y_s}{b}} \left(\frac{\partial^2 w_0(\pm\xi_s, \eta)}{\partial \xi \partial \eta} \right)^2 d\eta \tag{3.110}$$

$$U_b^{\text{warping}(s)} = \frac{16E_y^s \Gamma}{b^3 a^2} \int_{-\frac{2y_s}{b}}^{\frac{2y_s}{b}} \left(\frac{\partial^3 w_0(\pm\xi_s, \eta)}{\partial \eta^2 \partial \xi} \right)^2 d\eta \tag{3.111}$$

$$U_b^s = U_b^{\text{bending } x^{(s_1)}} + U_b^{\text{warping}(s_1)} + U_b^{\text{venant}(s_1)} +$$
$$+ U_b^{\text{bending } x^{(s_2)}} + U_b^{\text{warping}(s_1)} + U_b^{\text{venant}(s_2)} \tag{3.112}$$

Furthermore, in Appendix A (Stiffeners' Parameters), the methodology used to obtain the parameters E_y^s, G_{xz}^s, J, Γ and I_{zz} can be verified.

3.7.5 Stationary Value of the Total Potential Energy for the Buckling Problem

Taking the first variation of the total potential energy $\Pi_2 = U_b + U_b^s - U_N$ with respect to the unknown coefficients c_{ij}^w, $c_{ij}^{\varphi_u}$, and $c_{ij}^{\varphi_v}$ results in:

$$\frac{\partial \Pi_2}{\partial c_{ij}^w} = 0, \quad \frac{\partial \Pi_2}{\partial c_{ij}^{\varphi_u}} = 0, \quad \frac{\partial \Pi_2}{\partial c_{ij}^{\varphi_v}} = 0, \quad i = 1, 2, \ldots, I; \quad j = 1, 2, \ldots, J \tag{3.113}$$

This leads to a linear buckling eigenvalue problem, articulated as:

$$\{\mathbf{K}_b + \mathbf{K}_b^s - \boldsymbol{\lambda}\mathbf{K}_g\}\{\mathbf{c}\} = \mathbf{0} \tag{3.114}$$

where $\{\mathbf{c}\} = \{\mathbf{c}^w, \frac{a\mathbf{c}^{\varphi_u}}{2}, \frac{b\mathbf{c}^{\varphi_v}}{2}\}^T$, is the vector of unknown coefficients. Each component $\mathbf{c}^p$, $p \in \{w, \varphi_u, \varphi_v\}$ is a vector with $I \times J$ terms.

The bending stiffness matrix $\mathbf{K}_b$ is structured as follows:

$$\mathbf{K_b} = \begin{bmatrix} \mathbf{K}_{ww} & \mathbf{K}_{w\varphi_u} & \mathbf{K}_{w\varphi_v} \\ \mathbf{K}_{w\varphi_u}^T & \mathbf{K}_{\varphi_u\varphi_u} & \mathbf{K}_{\varphi_u\varphi_v} \\ \mathbf{K}_{w\varphi_v}^T & \mathbf{K}_{\varphi_u\varphi_v}^T & \mathbf{K}_{\varphi_v\varphi_v} \end{bmatrix} \tag{3.115}$$

where

$$\mathbf{K}_{ww} = \left\{ A_{44}\mathbf{I}^{1010}\frac{b}{a} + A_{55}\mathbf{I}^{0101}\frac{a}{b} + A_{45}(\mathbf{I}^{0110} + \mathbf{I}^{1001}) \right\}_{ww} \tag{3.116}$$

$$\mathbf{K}_{w\varphi_u} = \left\{ A_{44}\mathbf{I}^{1000}\frac{b}{a} + A_{45}\mathbf{I}^{0100} \right\}_{w\varphi_u} \tag{3.117}$$

$$\mathbf{K}_{w\varphi_v} = \left\{ A_{55}\mathbf{I}^{0100}\frac{a}{b} + A_{45}\mathbf{I}^{1000} \right\}_{w\varphi_v} \tag{3.118}$$

$$\mathbf{K}_{\varphi_u\varphi_u} = \left\{ A_{44}\mathbf{I}^{0000}\frac{b}{a} + 4D_{11}\mathbf{I}^{1010}\frac{b}{a^3} + \frac{4D_{16}(\mathbf{I}^{0110} + \mathbf{I}^{1001})}{a^2} + \frac{4D_{66}\mathbf{I}^{0101}}{ab} \right\}_{\varphi_u\varphi_u} \tag{3.119}$$

$$\mathbf{K}_{\varphi_u\varphi_v} = \left\{ A_{45}\mathbf{I}^{0000} + \frac{4D_{26}\mathbf{I}^{0101}}{b^2} + \frac{4(D_{66}\mathbf{I}^{0110} + D_{12}\mathbf{I}^{1001})}{ab} + \frac{4D_{16}\mathbf{I}^{1010}}{a^2} \right\}_{\varphi_u\varphi_v} \tag{3.120}$$

$$\mathbf{K}_{\varphi_v\varphi_v} = \left\{ A_{55}\mathbf{I}^{0000}\frac{a}{b} + \frac{4D_{22}\mathbf{I}^{0101}a}{b^3} + \frac{4D_{26}(\mathbf{I}^{0110} + \mathbf{I}^{1001})}{b^2} + \frac{4D_{66}\mathbf{I}^{1010}}{ab} \right\}_{\varphi_v\varphi_v} \tag{3.121}$$

where

$$\mathbf{I}_{rs}^{defg} = \iint_{\Omega_c} \frac{\partial^{d+e}[\mathbf{f}^r(\xi,\eta)]^T}{\partial\xi^d\partial\eta^e} \cdot \frac{\partial^{f+g}\mathbf{f}^s(\xi,\eta)}{\partial\xi^f\partial\eta^g}\, d\xi\, d\eta \quad \{r,s\} \in \{u,v,w,\varphi_u,\varphi_v\} \tag{3.122}$$

The out-of-plane bending and torsion stiffness matrix $\mathbf{K}_b^s$ due to the inclusion of stiffeners is structured as follows:

$$\mathbf{K}_b^s = \begin{bmatrix} \mathbf{K}_{bb}^s & \mathbf{0} & \mathbf{0} \\ \mathbf{0} & \mathbf{0} & \mathbf{0} \\ \mathbf{0} & \mathbf{0} & \mathbf{0} \end{bmatrix} \tag{3.123}$$

where

$$\mathbf{K}_{bb}^s = \frac{8E_y^s I_{xx}}{b^3} \int_{-\frac{2y_s}{b}}^{\frac{2y_s}{b}} \left[\mathbf{f}_{,\eta\eta}^w(\pm\xi_s,\eta) \right]^T \left[\mathbf{f}_{,\eta\eta}^w(\pm\xi_s,\eta) \right] d\eta + \tag{3.124}$$

$$+ \frac{8G_{xz}^s J}{a^2 b} \int_{-\frac{2y_s}{b}}^{\frac{2y_s}{b}} \left[\mathbf{f}_{,\xi\eta}^w(\pm\xi_s,\eta) \right]^T \left[\mathbf{f}_{,\xi\eta}^w(\pm\xi_s,\eta) \right] d\eta + \tag{3.125}$$

$$+ \frac{32E_y^s \Gamma}{b^3 a^2} \int_{-\frac{2y_s}{b}}^{\frac{2y_s}{b}} \left[\mathbf{f}_{,\eta\eta\xi}^w(\pm\xi_s,\eta) \right]^T \left[\mathbf{f}_{,\eta\eta\xi}^w(\pm\xi_s,\eta) \right] d\eta \tag{3.126}$$

The geometrical matrix $\mathbf{K}_g$ associated with the von Kármán strains $\tilde{\boldsymbol{\varepsilon}}$, and $\overline{\mathbf{N}}$, derived from the in-plane stresses obtained during the prebuckling analysis, is structured as follows:

$$\mathbf{K}_g = \begin{bmatrix} \mathbf{K}_{gg} & \mathbf{0} & \mathbf{0} \\ \mathbf{0} & \mathbf{0} & \mathbf{0} \\ \mathbf{0} & \mathbf{0} & \mathbf{0} \end{bmatrix} \tag{3.127}$$

where

$$\begin{aligned}
\mathbf{K}_{gg} = 2\Bigg\{ &\frac{A_{16}E_{10}^u\mathbf{I}^{0110}}{a} + \frac{A_{16}E_{10}^u\mathbf{I}^{1001}}{a} + \frac{A_{16}E_{01}^u\mathbf{I}^{1010}}{a} + \frac{A_{66}E_{10}^v\mathbf{I}^{0110}}{a} + \frac{A_{66}E_{10}^v\mathbf{I}^{1001}}{a} \\
&+ \frac{A_{12}E_{01}^v\mathbf{I}^{1010}}{a} + \frac{A_{12}E_{10}^u\mathbf{I}^{0101}}{b} + \frac{A_{66}E_{01}^u\mathbf{I}^{0110}}{b} + \frac{A_{66}E_{01}^u\mathbf{I}^{1001}}{b} + \frac{A_{26}E_{10}^v\mathbf{I}^{0101}}{b} \\
&+ \frac{A_{26}E_{01}^v\mathbf{I}^{0110}}{b} + \frac{A_{26}E_{01}^v\mathbf{I}^{1001}}{b} + \frac{A_{26}E_{01}^u\mathbf{I}^{0101}a}{b^2} + \frac{A_{11}E_{10}^u\mathbf{I}^{1010}b}{a^2} + \frac{A_{22}E_{01}^v\mathbf{I}^{0101}a}{b^2} \\
&+ \frac{A_{16}E_{10}^v\mathbf{I}^{1010}b}{a^2} \Bigg\}_{ww}
\end{aligned} \tag{3.128}$$

where

$$E_{pq}^{\vartheta}\mathbf{I}_{ww}^{defg} = \iint_{\Omega_c} E_{pq}^{\vartheta}(\xi,\eta) \cdot \frac{\partial^{d+e}[\mathbf{f}^w(\xi,\eta)]^T}{\partial\xi^d\partial\eta^e} \cdot \frac{\partial^{f+g}\mathbf{f}^w(\xi,\eta)}{\partial\xi^f\partial\eta^g}\, d\xi\, d\eta$$

$$\{i,j\} \in \{1,2,6\};\ \{p,q\} \in \{0,1\};\ \{\vartheta\} \in \{u,v\};\ \{d,e,f,g\} \in \{0,1\} \tag{3.129}$$

with

$$E_{pq}^u(\xi,\eta) = \frac{\partial^{p+q}u_0(\xi,\eta)}{\partial\xi^p\partial\eta^q}, \quad E_{pq}^v(\xi,\eta) = \frac{\partial^{p+q}v_0(\xi,\eta)}{\partial\xi^p\partial\eta^q}, \quad \{p,q\} \in \{0,1\} \tag{3.130}$$

The dimensions of each matrices are $(3 \times I \times J) \times (3 \times I \times J)$. The solution of Eq. 3.114 determines the buckling loads and mode shapes of the orthotropic plates, with the critical buckling load denoted by λ_{cr}. Furthermore, the diagram of the implementation used in buckling analysis can be visualized in Figure 3.16.

Input

- Input the material
properties and stackup
- Define the geometry of the
plate, cutout, and stiffener
- Define the number of
hierarchical polynomial terms
- Use $\overline{N}_x$, $\overline{N}_y$ and $\overline{N}_{xy}$
calculated in prebuckling
analysis for a loading mode

Compute the stiffness
matrices $\mathbf{B}, \mathbf{D}, \mathbf{H}$

Compute matrices
$\mathbf{K}_b$, $\mathbf{K}_b^s$, $\mathbf{K}_g$

Transform and discretize the
domain within the range
[-1, 1] and determine the
effective domain of the
plate and stiffeners

Compute the
derivatives of the
admissible function
via product rule of
partial derivatives

Find integration
points and weights

Define admissible
functions for boundary
conditions to w, φ_u, φ_v

End

Compute
$\{\mathbf{K}_b + \mathbf{K}_b^s\text{-}\lambda\mathbf{K}_g\}\{\mathbf{c}\} = \mathbf{0}$

Define the number
of integration points

No

Yes

Converge?

Obtain critical modes
from $\boldsymbol{\lambda}$

FIGURE 3.16 – Diagram of the implementation used in buckling analysis.

4 Numerical Improvement on the Simulation Performance of the Model

A methodology has been developed to enhance the efficiency of integral calculations by utilizing hierarchical polynomials. This strategy offers significant advantages by eliminating the need to modify trial shape functions, ensuring both speed and simplicity in various simulations.

Considering that each of the four edges of the plate can have three possible boundary conditions (clamped, simply supported, or free), this would typically result in $3^4 - 1$ integration sets to cover all scenarios. However, in the implementation presented in this study, only one integration set is necessary.

Initially, the integrals derived from the first four hierarchical polynomials are calculated for all simulations in the directions of ξ and η, along with subsequent polynomials for $I > 4$ and $J > 4$, which will enrich the solution. Based on the results obtained from these integrals, and depending on the adopted boundary condition, certain polynomials are then excluded through a computational method. This involves the exclusion of rows and columns associated with χ_1, χ_2, χ_3, and χ_4 only in the final phase of prebuckling and buckling calculations.

For example, if a clamped condition on all edges needs to be simulated, it is sufficient to subsequently nullify the contributions from the polynomials as indicated in Table 4.1 after calculating all integrals that include contributions from all polynomials.

TABLE 4.1 – Table showing the procedure adopted to obtain the CCCC solution. The polynomials indicated with a value of zero will not be used in the solution.

Variable	ξ				η			
	χ_1	χ_2	χ_3	χ_4	χ_1	χ_2	χ_3	χ_4
u	1	1	1	1	1	1	1	1
v	1	1	1	1	1	1	1	1
w	0	1	0	1	0	1	0	1
φ_u	0	1	0	1	0	1	0	1

Variable	ξ				η			
	χ_1	χ_2	χ_3	χ_4	χ_1	χ_2	χ_3	χ_4
φ_v	0	1	0	1	0	1	0	1

However, if another simulation with a different boundary condition, such as SSSS, is desired, it would be enough to select the appropriate polynomials without needing to perform another set of integrations. This demonstrates the efficiency of using hierarchical polynomials in solving the Discrete Ritz Method problem for various boundary conditions with only one set of integrations, employing the First-Order Shear Deformation Theory (FSDT).

Additionally, a methodology was developed, as will be shown later, to ensure that from a single integration set with I and J, all data for such that $I' \leq I$ and $J' \leq J$ are also collected. This approach significantly reduces the computational cost, thereby facilitating the study of convergence. For example, in a simulation where $I = J = 30$, all values for $I' = J' \leq 30$ will be collected.

It is possible to calculate the $\mathbf{K}_{uu}$, $\mathbf{K}_{uv}$, $\mathbf{K}_{vv}$, $\mathbf{K}_{ww}$, $\mathbf{K}_{w\varphi_u}$, $\mathbf{K}_{w\varphi_v}$, $\mathbf{K}_{\varphi_u\varphi_u}$, $\mathbf{K}_{\varphi_u\varphi_v}$ and $\mathbf{K}_{\varphi_v\varphi_v}$ for I and J terms and obtain the result for $I' \leq I$ and $J' \leq J$ terms simply by removing unwanted lines and columns from the aforementioned matrices. In an analogous manner, any desired boundary condition can be satisfied without the need of recalculating the integrals used in those matrices.

To illustrate the logic behind this method, it is convenient to first examine the structure of the vector of trial functions in Eq. 4.1.

$$\mathbf{f}(\xi,\eta) = \begin{bmatrix} \chi_1(\xi)\chi_1(\eta) \\ \chi_1(\xi)\chi_2(\eta) \\ \vdots \\ \chi_1(\xi)\chi_J(\eta) \\ \chi_2(\xi)\chi_1(\eta) \\ \chi_2(\xi)\chi_2(\eta) \\ \vdots \\ \vdots \\ \chi_I(\xi)\chi_1(\eta) \\ \chi_I(\xi)\chi_2(\eta) \\ \vdots \\ \chi_I(\xi)\chi_J(\eta) \end{bmatrix}^T \tag{4.1}$$

The function $\chi_{I'}(\xi)$ shows up in the columns with indexes $(I'-1)J+1, (I'-1)J+$

$2, \ldots, I'J$, and the function $\chi_{J'}(\eta)$ shows up in the columns with indexes $J', J'+J, J'+2J, \ldots, J'+(I-1)J$. For a desired number of terms $I' \leq I$ in the ξ functions, the elements with $\chi_{I'+1}(\xi), \chi_{I'+2}(\xi), \ldots, \chi_I(\xi)$ must be removed from $\mathbf{f}(\xi, \eta)$. The variable $\iota_\xi(I')$ denotes the set with the indexes of the columns of $\mathbf{f}(\xi, \eta)$ to be eliminated and is given by:

$$\iota_\xi(I') = \bigcup_{i=I'+1}^{I} \{(i-1)J+1, (i-1)J+2, \ldots, iJ\} = \bigcup_{i=I'+1}^{I} [(i-1)J+1, iJ] \qquad (4.2)$$

Similarly, to obtain the solution for $J' \leq J$ terms in the η functions, the elements with $\chi_{J'+1}(\eta), \chi_{J'+2}(\eta), \ldots, \chi_J(\eta)$ must be removed from $\mathbf{f}(\xi, \eta)$. The variable $\iota_\eta(J')$ denotes the set with the indexes of the columns of $\mathbf{f}(\xi, \eta)$ to be eliminated and is given by:

$$\iota_\eta(J') = \bigcup_{i=1}^{I} \{J'+(i-1)J+1, J'+(i-1)J+2, \ldots, iJ\} = \bigcup_{i=1}^{I} [J'+(i-1)J+1, iJ] \qquad (4.3)$$

Therefore, to solve the buckling problem for I' terms in ξ and J' terms in η, the columns with indices in $\iota_\xi(I') \cup \iota_\eta(J')$ must be eliminated from $\mathbf{f}(\xi, \eta)$. Consequently, for the matrices obtained by integrating the product $\left[\mathbf{f}(\xi, \eta)\right]^T \mathbf{f}(\xi, \eta)$, the rows and columns within that set must be removed.

For example, suppose all the desired matrices have already been calculated for $I = J = 6$ terms. Then, it is possible to analyze the results for any number of $I' \leq 6$ and $J' \leq 6$ terms without the need of recalculating the matrices. If $I' = J' = 4$, according to Eqs. 4.2 and 4.3, $\iota_\xi(4) = [25, 30] \cup [31, 36] = [25, 36]$ and $\iota_\eta(4) = [5, 6] \cup [11, 12] \cup [17, 18] \cup [23, 24] \cup [29, 30] \cup [35, 36]$. This means that the columns in the set $\iota_\xi(4) \cup \iota_\eta(4) = \{5, 6, 11, 12, 17, 18, 23, 24, 25, 26, 27, 28, 29, 30, 31, 32, 33, 34, 35, 36\}$ must be removed from $\mathbf{f}(\xi, \eta)$. Consequently, the rows and columns in the same set have to be eliminated from the matrices $\mathbf{K}_{uu}$, $\mathbf{K}_{uv}$, $\mathbf{K}_{vv}$, $\mathbf{K}_{ww}$, $\mathbf{K}_{w\varphi_u}$, $\mathbf{K}_{w\varphi_v}$, $\mathbf{K}_{\varphi_u\varphi_u}$, $\mathbf{K}_{\varphi_u\varphi_v}$ and $\mathbf{K}_{\varphi_v\varphi_v}$. The terms that will be excluded in the given example are contained in Table 4.2, with $I = J = 6$ terms and $I' = J' = 4$.

TABLE 4.2 – Table containing the terms that will be excluded in the given example, with $I = J = 6$ terms and $I' = J' = 4$.

1	2	3	4	5	6	7	8	9	10	11	12
$\chi_1(\xi)\chi_1(\eta)$	$\chi_1(\xi)\chi_2(\eta)$	$\chi_1(\xi)\chi_3(\eta)$	$\chi_1(\xi)\chi_4(\eta)$	$\chi_1(\xi)\chi_5(\eta)$	$\chi_1(\xi)\chi_6(\eta)$	$\chi_2(\xi)\chi_1(\eta)$	$\chi_2(\xi)\chi_2(\eta)$	$\chi_2(\xi)\chi_3(\eta)$	$\chi_2(\xi)\chi_4(\eta)$	$\chi_2(\xi)\chi_5(\eta)$	$\chi_2(\xi)\chi_6(\eta)$
13	14	15	16	17	18	19	20	21	22	23	24
$\chi_3(\xi)\chi_1(\eta)$	$\chi_3(\xi)\chi_2(\eta)$	$\chi_3(\xi)\chi_3(\eta)$	$\chi_3(\xi)\chi_4(\eta)$	$\chi_3(\xi)\chi_5(\eta)$	$\chi_3(\xi)\chi_6(\eta)$	$\chi_4(\xi)\chi_1(\eta)$	$\chi_4(\xi)\chi_2(\eta)$	$\chi_4(\xi)\chi_3(\eta)$	$\chi_4(\xi)\chi_4(\eta)$	$\chi_4(\xi)\chi_5(\eta)$	$\chi_4(\xi)\chi_6(\eta)$
25	26	27	28	29	30	31	32	33	34	35	36
$\chi_5(\xi)\chi_1(\eta)$	$\chi_5(\xi)\chi_2(\eta)$	$\chi_5(\xi)\chi_3(\eta)$	$\chi_5(\xi)\chi_4(\eta)$	$\chi_5(\xi)\chi_5(\eta)$	$\chi_5(\xi)\chi_6(\eta)$	$\chi_6(\xi)\chi_1(\eta)$	$\chi_6(\xi)\chi_2(\eta)$	$\chi_6(\xi)\chi_3(\eta)$	$\chi_6(\xi)\chi_4(\eta)$	$\chi_6(\xi)\chi_5(\eta)$	$\chi_6(\xi)\chi_6(\eta)$

Another removal must be performed to satisfy the boundary conditions. Since the

proposed implementation uses hierarchical polynomials as trial functions, the boundary
conditions can be satisfied by setting some of the first four polynomials in ξ and η equal
to zero. Each one of these polynomials is associated to a removal set, which is a set
containing the indexes of the columns of $\mathbf{f}(\xi, \eta)$ where it appears. All the eight removal
sets (four in ξ and four in η) are listed in Table 4.3.

TABLE 4.3 – Columns of $\mathbf{f}(\xi, \eta)$ where the first four hierarchical polynomials appear for a total of I'
terms in ξ and J' terms in η.

Function	Plot	Removal set
$\chi_1(\xi)$		$\{1, 2, \ldots, J'\} = [1, J']$
$\chi_2(\xi)$		$\{J' + 1, J' + 2, \ldots, 2J'\} = [J' + 1, 2J']$
$\chi_3(\xi)$		$\{2J' + 1, 2J' + 2, \ldots, 3J'\} = [2J' + 1, 3J']$
$\chi_4(\xi)$		$\{3J' + 1, 3J' + 2, \ldots, 4J'\} = [3J' + 1, 4J']$
$\chi_1(\eta)$		$\{1, J' + 1, 2J' + 1, \ldots, (I' - 1)J' + 1\}$
$\chi_2(\eta)$		$\{2, J' + 2, 2J' + 2, \ldots, (I' - 1)J' + 2\}$
$\chi_3(\eta)$		$\{3, J' + 3, 2J' + 3, \ldots, (I' - 1)J' + 3\}$
$\chi_4(\eta)$		$\{4, J' + 4, 2J' + 4, \ldots, (I' - 1)J' + 4\}$

The integrals and matrices are initially calculated considering all terms (as if all the
plate's edges were free to move), and the appropriate rows and columns are subsequently
removed from the matrices to reflect the boundary conditions at the plate's edges. For
each constrained edge, a convenient removal set is obtained for the functions w_0, φ_u and
φ_v. For every one of these functions a resulting removal set is obtained from the union of
the removal sets of the four edges. The way the removal sets are obtained is summarized
in Table 4.4, and the resulting removal set for each function is the union of the removal
sets obtained at the edges.

TABLE 4.4 – Removal sets for w_0, φ_u and φ_v at the plate's edges.

	Edge at $\xi = 1$ (i.e., $x = a/2$)	
	Simply supported $w_0(1, \eta) = 0$	Clamped $w_0(1, \eta) = \varphi_u(1, \eta) = \varphi_v(1, \eta) = 0$
w_0 removal set	$\chi_3(\xi)$ removal set	$\chi_3(\xi)$ removal set
φ_u removal set	$\varnothing$	$\chi_3(\xi)$ removal set
φ_v removal set	$\varnothing$	$\chi_3(\xi)$ removal set
	Edge at $\eta = 1$ (i.e., $y = b/2$)	
	Simply supported $w_0(\xi, 1) = 0$	Clamped $w_0(\xi, 1) = \varphi_u(\xi, 1) = \varphi_v(\xi, 1) = 0$
w_0 removal set	$\chi_3(\eta)$ removal set	$\chi_3(\eta)$ removal set
φ_u removal set	$\varnothing$	$\chi_3(\eta)$ removal set
φ_v removal set	$\varnothing$	$\chi_3(\eta)$ removal set
	Edge at $\xi = -1$ (i.e., $x = -a/2$)	
	Simply supported $w_0(-1, \eta) = 0$	Clamped $w_0(-1, \eta) = \varphi_u(-1, \eta) = \varphi_v(-1, \eta) = 0$
w_0 removal set	$\chi_1(\xi)$ removal set	$\chi_1(\xi)$ removal set
φ_u removal set	$\varnothing$	$\chi_1(\xi)$ removal set
φ_v removal set	$\varnothing$	$\chi_1(\xi)$ removal set
	Edge at $\eta = -1$ (i.e., $y = -b/2$)	
	Simply supported $w_0(\xi, -1) = 0$	Clamped $w_0(\xi, -1) = \varphi_u(\xi, -1) = \varphi_v(\xi, -1) = 0$
w_0 removal set	$\chi_1(\eta)$ removal set	$\chi_1(\eta)$ removal set
φ_u removal set	$\varnothing$	$\chi_1(\eta)$ removal set
φ_v removal set	$\varnothing$	$\chi_1(\eta)$ removal set

For example, if $I' = J' = 6$ terms are used to analyze the buckling modes of a plate, the following shape function removal sets can be used:

$$\chi_1(\xi) \text{ removal set} = \{1, 2, 3, 4, 5, 6\}$$
$$\chi_3(\xi) \text{ removal set} = \{13, 14, 15, 16, 17, 18\}$$
$$\chi_1(\eta) \text{ removal set} = \{1, 7, 13, 19, 25, 31\}$$
$$\chi_3(\eta) \text{ removal set} = \{3, 9, 15, 21, 27, 33\}$$

To ensure greater clarity, Table 4.5 contains all terms and their order for verification

of the results.

TABLE 4.5 – Table containing all terms for $I' = J' = 6$.

1	2	3	4	5	6	7	8	9	10	11	12
$\chi_1(\xi)\chi_1(\eta)$	$\chi_1(\xi)\chi_2(\eta)$	$\chi_1(\xi)\chi_3(\eta)$	$\chi_1(\xi)\chi_4(\eta)$	$\chi_1(\xi)\chi_5(\eta)$	$\chi_1(\xi)\chi_6(\eta)$	$\chi_2(\xi)\chi_1(\eta)$	$\chi_2(\xi)\chi_2(\eta)$	$\chi_2(\xi)\chi_3(\eta)$	$\chi_2(\xi)\chi_4(\eta)$	$\chi_2(\xi)\chi_5(\eta)$	$\chi_2(\xi)\chi_6(\eta)$
13	**14**	**15**	**16**	**17**	**18**	**19**	**20**	**21**	**22**	**23**	**24**
$\chi_3(\xi)\chi_1(\eta)$	$\chi_3(\xi)\chi_2(\eta)$	$\chi_3(\xi)\chi_3(\eta)$	$\chi_3(\xi)\chi_4(\eta)$	$\chi_3(\xi)\chi_5(\eta)$	$\chi_3(\xi)\chi_6(\eta)$	$\chi_4(\xi)\chi_1(\eta)$	$\chi_4(\xi)\chi_2(\eta)$	$\chi_4(\xi)\chi_3(\eta)$	$\chi_4(\xi)\chi_4(\eta)$	$\chi_4(\xi)\chi_5(\eta)$	$\chi_4(\xi)\chi_6(\eta)$
25	**26**	**27**	**28**	**29**	**30**	**31**	**32**	**33**	**34**	**35**	**36**
$\chi_5(\xi)\chi_1(\eta)$	$\chi_5(\xi)\chi_2(\eta)$	$\chi_5(\xi)\chi_3(\eta)$	$\chi_5(\xi)\chi_4(\eta)$	$\chi_5(\xi)\chi_5(\eta)$	$\chi_5(\xi)\chi_6(\eta)$	$\chi_6(\xi)\chi_1(\eta)$	$\chi_6(\xi)\chi_2(\eta)$	$\chi_6(\xi)\chi_3(\eta)$	$\chi_6(\xi)\chi_4(\eta)$	$\chi_6(\xi)\chi_5(\eta)$	$\chi_6(\xi)\chi_6(\eta)$

The resulting removal set for w_0, φ_u and φ_v is obtained from the union of the respective removal sets at each edge.

Thus, the rows with indexes in the resulting w_0 removal set must be eliminated from $\mathbf{K}_{ww}$, $\mathbf{K}_{w\varphi_u}$ and $\mathbf{K}_{w\varphi_v}$. Additionally, the same procedure must be performed for the columns of $\mathbf{K}_{ww}$.

The columns with indexes in the resulting φ_u removal set must be eliminated from $\mathbf{K}_{w\varphi_u}$ and $\mathbf{K}_{\varphi_u\varphi_u}$. For $\mathbf{K}_{\varphi_u\varphi_v}$ the procedure must be performed for the rows, while as for $\mathbf{K}_{\varphi_u\varphi_u}$ it must be done for the rows and columns.

The columns with indexes in the resulting φ_v removal set must be eliminated from $\mathbf{K}_{w\varphi_v}$, $\mathbf{K}_{\varphi_u\varphi_v}$ and $\mathbf{K}_{\varphi_v\varphi_v}$. Additionally, the same procedure must be performed for the columns of $\mathbf{K}_{\varphi_v\varphi_v}$.

Finally, considering that the first four hierarchical polynomials are always initially integrated, an additional numerical improvement on the simulation performance was achieved by verifying the symmetry of the resulting matrices derived from the multiplication of partial derivatives in both the prebuckling and buckling analysis, as follows:

$$I^{0000}(i, j) = I^{0000}(j, i) \quad i = 1, 2, \ldots, I; \quad j = 1, 2, \ldots, J \tag{4.4}$$

$$I^{1010}(i, j) = I^{1010}(j, i) \quad i = 1, 2, \ldots, I; \quad j = 1, 2, \ldots, J \tag{4.5}$$

$$I^{0101}(i, j) = I^{0101}(j, i) \quad i = 1, 2, \ldots, I; \quad j = 1, 2, \ldots, J \tag{4.6}$$

where

$$\mathbf{I}_{rs}^{defg} = \int\!\!\int_{\Omega_c} \frac{\partial^{d+e}[\mathbf{f}^r(\xi, \eta)]^T}{\partial\xi^d\partial\eta^e} \cdot \frac{\partial^{f+g}\mathbf{f}^s(\xi, \eta)}{\partial\xi^f\partial\eta^g} \, d\xi \, d\eta \quad \{r, s\} \in \{u, v, w, \varphi_u, \varphi_v\} \tag{4.7}$$

Furthermore, in the buckling analysis, it was also verified that the following matrices possess the following symmetry, due to the fact that the values of E_{pq}^{ϑ}, obtained through the prebuckling analysis, are scalars. Thus, at each integration point:

$$E_{10}^u I^{1010}(i,j) = E_{10}^u I^{1010}(j,i) \quad i = 1, 2, \ldots, I; \quad j = 1, 2, \ldots, J \tag{4.8}$$

$$E_{10}^u I^{0101}(i,j) = E_{10}^u I^{0101}(j,i) \quad i = 1, 2, \ldots, I; \quad j = 1, 2, \ldots, J \tag{4.9}$$

$$E_{01}^u I^{1010}(i,j) = E_{01}^u I^{1010}(j,i) \quad i = 1, 2, \ldots, I; \quad j = 1, 2, \ldots, J \tag{4.10}$$

$$E_{01}^u I^{0101}(i,j) = E_{01}^u I^{0101}(j,i) \quad i = 1, 2, \ldots, I; \quad j = 1, 2, \ldots, J \tag{4.11}$$

$$E_{10}^v I^{1010}(i,j) = E_{10}^v I^{1010}(j,i) \quad i = 1, 2, \ldots, I; \quad j = 1, 2, \ldots, J \tag{4.12}$$

$$E_{10}^v I^{0101}(i,j) = E_{10}^v I^{0101}(j,i) \quad i = 1, 2, \ldots, I; \quad j = 1, 2, \ldots, J \tag{4.13}$$

$$E_{01}^v I^{1010}(i,j) = E_{01}^v I^{1010}(j,i) \quad i = 1, 2, \ldots, I; \quad j = 1, 2, \ldots, J \tag{4.14}$$

$$E_{01}^v I^{0101}(i,j) = E_{01}^v I^{0101}(j,i) \quad i = 1, 2, \ldots, I; \quad j = 1, 2, \ldots, J \tag{4.15}$$

where

$$\mathbf{I}_{rs}^{defg} = \int \int_{\Omega_c} \frac{\partial^{d+e}[\mathbf{f}^r(\xi,\eta)]^T}{\partial\xi^d\partial\eta^e} \cdot \frac{\partial^{f+g}\mathbf{f}^s(\xi,\eta)}{\partial\xi^f\partial\eta^g} \, d\xi \, d\eta \quad \{r,s\} \in \{u,v,w,\varphi_u,\varphi_v\} \tag{4.16}$$

with

$$E_{pq}^u(\xi,\eta) = \frac{\partial^{p+q}u_0(\xi,\eta)}{\partial\xi^p\partial\eta^q}, \quad E_{pq}^v(\xi,\eta) = \frac{\partial^{p+q}v_0(\xi,\eta)}{\partial\xi^p\partial\eta^q}, \quad \{p,q\} \in \{0,1\} \tag{4.17}$$

This reduces the computational effort by half when calculating the integrals contained in these matrices, making the implementation not only robust but also faster, allowing simulations with lower indices and various boundary conditions.

In Figure 4.1, the representative diagram of the numerical improvements on the simulation performance of the model using hierarchical polynomials is shown. Note that the proposed methodology allows for adaptability in handling numerical simulations that initially did not converge by simulating them with lower indices of hierarchical polynomials. It also enables robust convergence analysis and facilitates a large number of simulations involving various boundary conditions from just one set of numerical integrations. Furthermore, considering that each integration point is independent, parallel computing was utilized through the Parallel Computing Toolbox™ in MATLAB®, where many calculations or processes are carried out simultaneously. This strategy can accelerate the simulation process, depending on the number of cores available in a computer's processor.
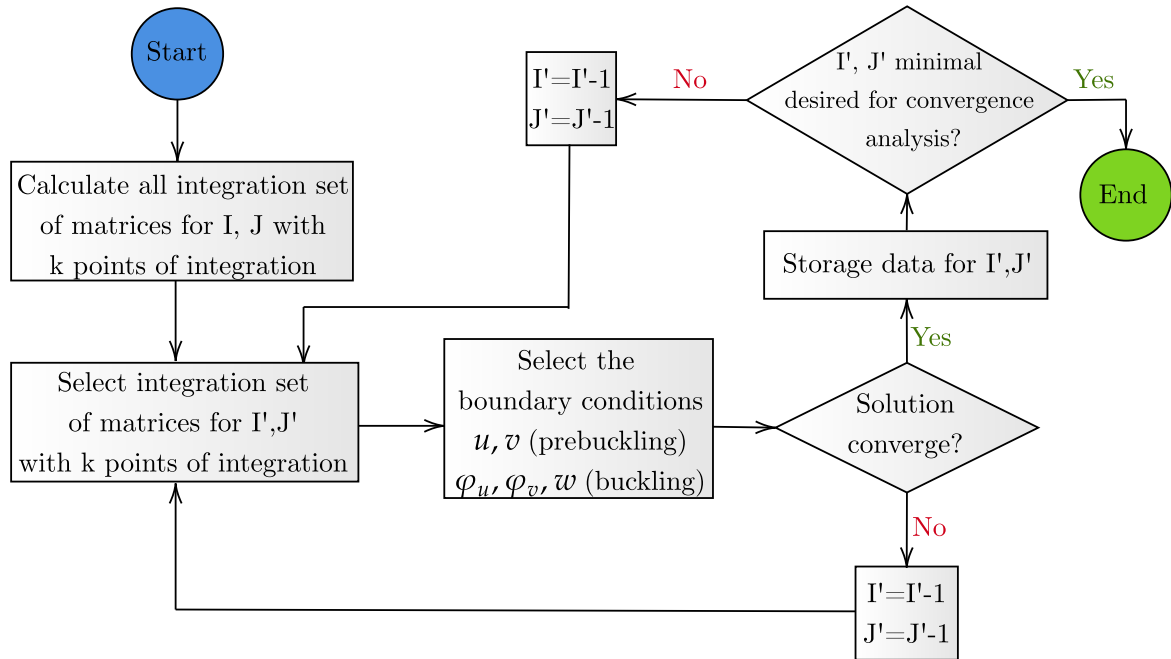
FIGURE 4.1 – Representative diagram of the numerical improvement on the simulation performance of
the model using hierarchical polynomials.

5 Model Verification

5.1 Initial Considerations

Throughout this work, the boundary conditions of a plate will be represented in a counterclockwise direction by four letters in the form 1234, as shown in Figure 5.1.
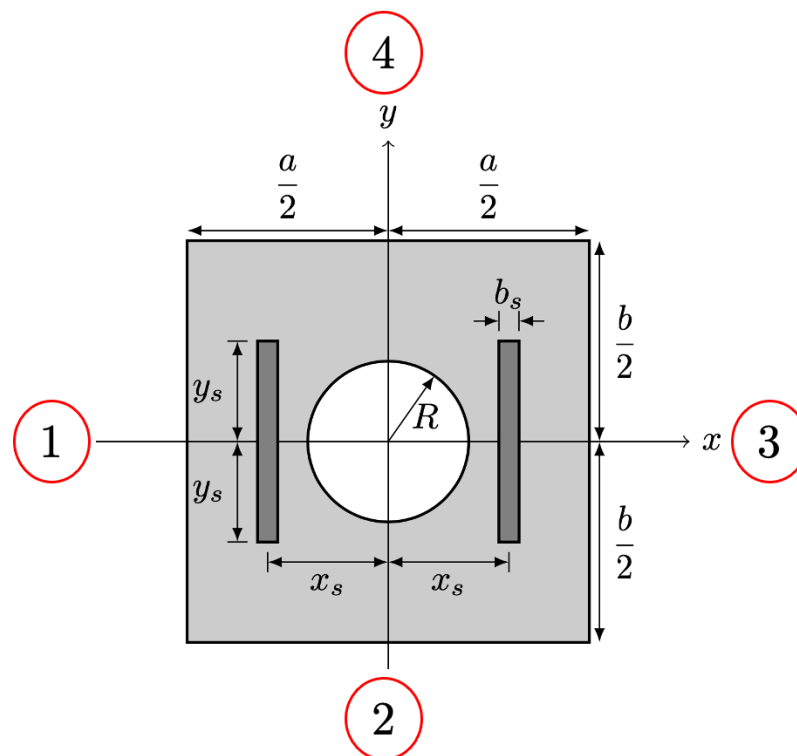
FIGURE 5.1 – Representative figure of the orientation adopted to characterize the boundary conditions 1234, represented in a counterclockwise direction.

The four letters can assume the following boundary conditions:

- C: Clamped;

- S: Simply Supported;

- F: Free.

Furthermore, the behavior of the mode shapes will be characterized by normalized absolute out-of-plane displacements and will use the "jet" color scale in MATLAB®, as shown in Figure 5.2.

0   1

FIGURE 5.2 – Representative figure of the "jet" color scale used to characterize the normalized absolute out-of-plane displacements.

Regarding the illustration of stress fields throughout this work, the same "jet" color scale will be used; however, the values will not be absolute nor normalized.

5.2   Plate

To verify the adopted model, which employs the Discrete Ritz Method using hierarchical polynomials as trial shape functions, simulations were conducted using MATLAB® software. These simulations were compared with the results obtained by (NARITA, 1990) for a composite plate with the properties specified in Table 5.1, under the boundary condition of being simply supported on all sides, as well as with a FEM.

TABLE 5.1 – Table containing the layer material properties for the composite plate studied, as provided in (NARITA, 1990).

Material	E_1 [GPa]	E_2 [GPa]	G_{12} [GPa]	G_{13} [GPa]	G_{23} [GPa]	ν_{12}	E_1/E_2
Graphite/Epoxy	138	8.96	7.1	7.1	7.1	0.3	15.4

As shown in Table 5.2, the appropriate hierarchical polynomials were selected for this configuration.

TABLE 5.2 – Table showing the procedure adopted to obtain the SSSS solution. The polynomials indicated with a value of zero will not be used in the solution.

Variable	ξ				η			
	χ_1	χ_2	χ_3	χ_4	χ_1	χ_2	χ_3	χ_4
u	1	1	1	1	1	1	1	1
v	1	1	1	1	1	1	1	1
w	0	1	0	1	0	1	0	1
φ_u	1	1	1	1	1	1	1	1
φ_v	1	1	1	1	1	1	1	1

In these simulations, the critical buckling results under positive pure shear loading, N_{xy}, were compared. This loading configuration was chosen in light of it being the setup

used in experiments that will be detailed subsequently. Furthermore, a finite element model was developed in Abaqus® software. The simulated geometric conditions used to verify the mathematical modeling in (NARITA, 1990) were arbitrarily selected and are shown in Table 5.3.

TABLE 5.3 – Table containing the simulated geometric conditions used to verify the mathematical modeling with (NARITA, 1990).

Stacking	$a \times a$ [mm]	t [mm]	h [mm]
[0, 0, 0]	425×425	1	3
[15, -15, 15]	425×425	1	3
[30, -30, 30]	425×425	1	3
[45, -45, 45]	425×425	1	3

Furthermore, the results from (NARITA, 1990) are dimensionless, as outlined in Eq. 5.1:

$$\lambda_{PS} = \frac{N_{xy}a^2}{D_0} \tag{5.1}$$

where

$$D_0 = \frac{E_1 h^3}{12(1 - \nu_{12}\nu_{21})} \qquad \nu_{21} = \nu_{12}\left(\frac{E_2}{E_1}\right) \tag{5.2}$$

where a represents the dimension of one side of the square plate, t denotes the thickness of each lamina, and h is the total thickness of the laminate.

To improve the verification reliability of the model, a Finite Element Model (FEM) was also developed using Abaqus® software, incorporating 7,225 mesh elements.

A comparison was conducted between the outcomes predicted by the model used in this study, the expected outcomes in (NARITA, 1990), and a model developed using Finite Element Analysis (FEA) with Abaqus® software. The semi-analytical approach employed $I = J = 20$ terms, with 100 integration points. The normalized critical buckling load results across four stacking configurations, including a comparative analysis between the methodology utilized in this study, the findings documented in (NARITA, 1990), and the Finite Element Method (FEM) analysis conducted with Abaqus®, can be verified in Table 5.4.

TABLE 5.4 – Normalized critical buckling load results $\lambda_{cr} = N_{xy}a^2/D_0$ across four stacking configurations, including comparative analysis between the methodology utilized in this study, findings documented in (NARITA, 1990), and through Finite Element Method (FEM) analysis conducted with Abaqus®.   The error calculated with respect to the results obtained through FEM is given by: Error $= (\lambda_{cr} - \lambda_{FEM})/\lambda_{FEM}$.

Stacking	(NARITA, 1990)	Error [%] (NARITA, 1990)	Present	Error [%] (Present)	FEM
[0, 0, 0]	25.71	0.04	25.64	-0.23	25.70
[15, -15, 15]	17.24	1.11	17.01	-0.23	17.05
[30, -30, 30]	14.64	4.42	13.99	-0.21	14.02
[45, -45, 45]	14.62	6.56	13.70	-0.15	13.72

Upon examining Table 5.4, it is observed that there was good agreement between the results presented by (NARITA, 1990) and those obtained through FEM, with an error ranging from 0.04% to 6.56%. It is noteworthy that as the ply angle increased, so did the error, reaching its maximum in the stacking configuration of [45,-45,45].

Furthermore, the semi-analytical model adopted, utilizing hierarchical polynomials, exhibited a deviation ranging from 0.15% to 0.23% in relation to FEM. The results obtained demonstrated an excellent correlation with both the finite element model and (NARITA, 1990).

Based on these results, the verification of the buckling analysis in a plate was considered satisfactory, given that the results obtained for four stacking configurations were consistent with those predicted in the literature and with those obtained through FEM. Following this verification, the buckling analysis for plates with circular cutouts was conducted, which will be presented in the next section.

Furthermore, the behavior of the first modes simulated across four stacking configurations, including their comparison with the findings documented in (NARITA, 1990) and FEM analysis, can be verified in Figures 5.3, 5.4, 5.5, and 5.6, which represent the normalized absolute out-of-plane displacements obtained.

(a) $\lambda = 25.71$ (b) $\lambda = 25.70$ (c) $\lambda = 25.64$
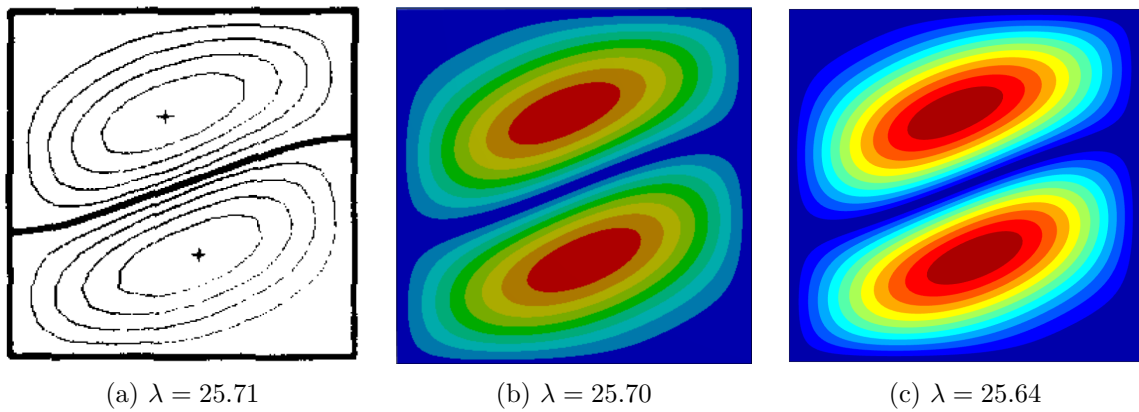
FIGURE 5.3 – Normalized absolute out-of-plane displacements for the 1° mode, SSSS boundary condition, under pure shear loading, with a stacking configuration of [0,0,0]. (a) (NARITA, 1990). (b) FEM. (c) Present.

(a) $\lambda = 17.24$ (b) $\lambda = 17.05$ (c) $\lambda = 17.01$
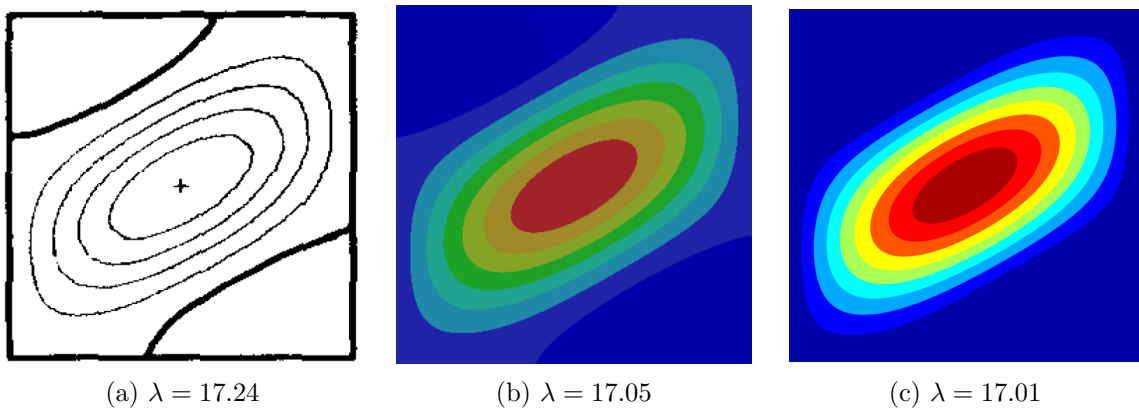
FIGURE 5.4 – Normalized absolute out-of-plane displacements for the 1° mode, SSSS boundary condition, under pure shear loading, with a stacking configuration of [15,-15,15]. (a) (NARITA, 1990). (b) FEM. (c) Present.

(a) $\lambda = 14.64$ (b) $\lambda = 14.02$ (c) $\lambda = 13.99$
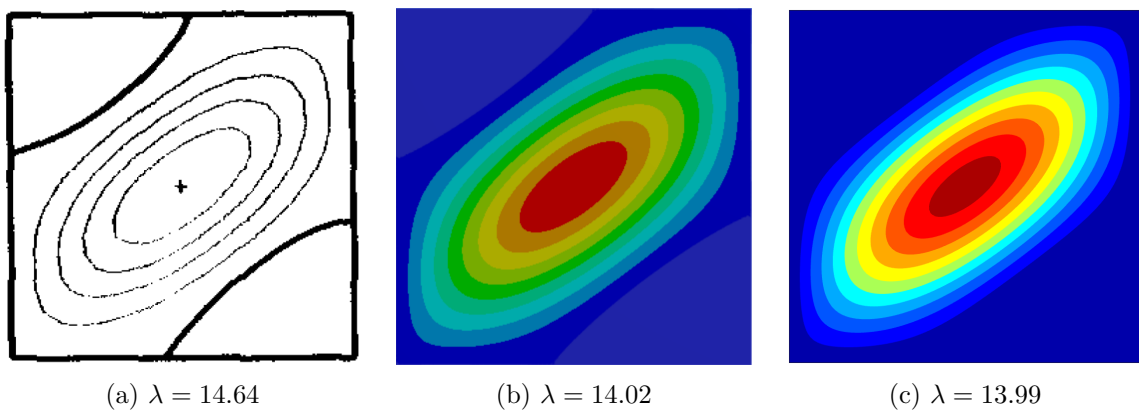
FIGURE 5.5 – Normalized absolute out-of-plane displacements for the 1° mode, SSSS boundary condition, under pure shear loading, with a stacking configuration of [30,-30,30]. (a) (NARITA, 1990). (b) FEM. (c) Present.

(a) $\lambda = 14.62$ (b) $\lambda = 13.72$ (c) $\lambda = 13.70$
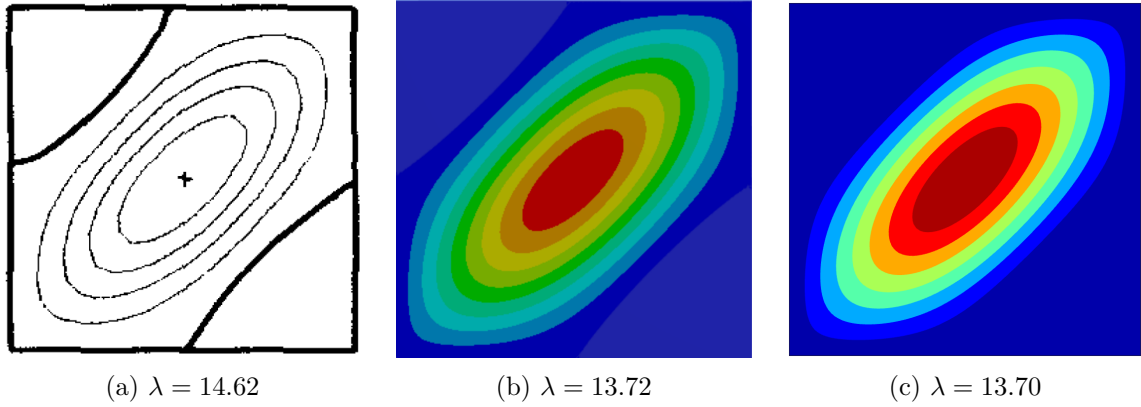
FIGURE 5.6 – Normalized absolute out-of-plane displacements for the 1° mode, SSSS boundary condition, under pure shear loading, with a stacking configuration of [45,-45,45]. (a) (NARITA, 1990). (b) FEM. (c) Present.

5.3 Plate with a Circular Cutout

To verify the model incorporating cutouts, a comparison was conducted with the results from (JING; DUAN, 2023), (ABOLGHASEMI *et al.*, 2019), and a FEM analysis for an isotropic square plate with a circular cutout. The material properties are detailed in Table 5.5. The plate thickness is specified as $h/a = 0.01$, and the radius of the circular cutout is represented by R.

TABLE 5.5 – Material properties of the isotropic square plates with a circular cutout as specified in (JING; DUAN, 2023).

E [GPa]	ν_{12}	a [mm]	b [mm]	h [mm]	h/a	R/a
200	0.3	100	100	1	0.01	0.3

Furthermore, although the chosen material is not a composite, it was selected primarily to verify the methodology itself. Additionally, data for this material were available from two literature sources. The application of this methodology to composite materials will be validated using experimentally simulated materials, as will be demonstrated throughout this work. Moreover, for isotropic material, the flexural rigidity of the plate is defined as:

$$D_1 = \frac{Eh^3}{12(1 - \nu_{12}^2)} \tag{5.3}$$

Initially, a comparison of in-plane loadings obtained through prebuckling calculations for a uniaxial loading N_x was conducted. Note that for this calculation, the first four hierarchical polynomials of u and v are always used, regardless of the simulated boundary condition. Additionally, since the integrals containing the trial shape functions are the

same for both u and v, it is only necessary to calculate the integrals for u, for instance.

Utilizing $I = J = 30$ terms in the admissible function and 292×292 Gauss points for numerical integration, the in-plane stress resultants $\bar{\mathbf{N}}$ of a square plate with a circular cutout ($R/a = 0.3$) under uniaxial loading N_x, with an SSSS boundary condition, were compared with the results from (JING; DUAN, 2023) and obtained via FEM (Abaqus®), as observed in Figures 5.7, 5.8, and 5.9. In this case, the in-plane stress resultants obtained using this method exhibit good agreement with both FEM and the results from the literature. It is important to note that this characterization highlights the behavior of the stress fields $\bar{N}_x$, $\bar{N}_y$, and $\bar{N}_{xy}$ when subjected to a unit value of N_x. Therefore, these values do not have specific units of measurement but are instead reference values relative to N_x. It is noteworthy that the presence of a circular cutout induces a stress concentration when subjected to uniaxial loading N_x, resulting in $\bar{N}_x$, $\bar{N}_y$, and $\bar{N}_{xy}$ exhibiting non-uniform stress distributions.
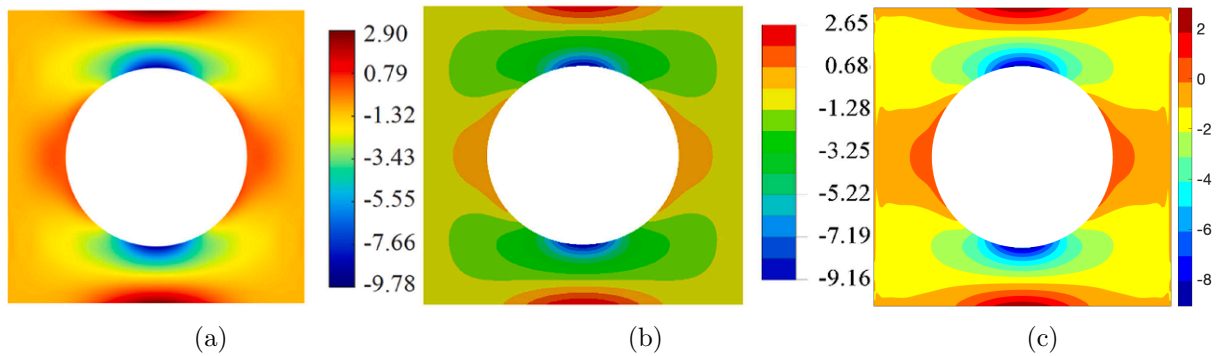
FIGURE 5.7 – Representative figure of the $\bar{N}_x$ stress field under uniaxial loading N_x, $R/a = 0.3$: (a) (JING; DUAN, 2023). (b) FEM. (c) Present. These values do not have specific units of measurement but are instead reference values relative to N_x.
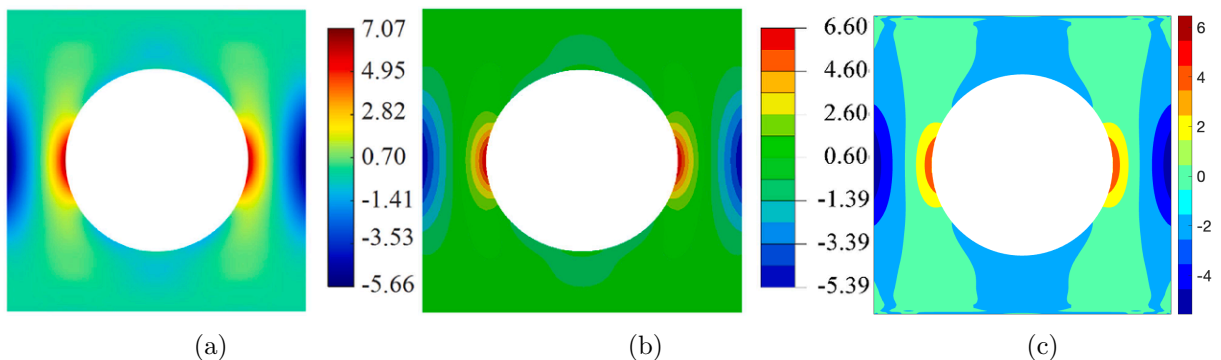
FIGURE 5.8 – Representative figure of the $\bar{N}_y$ stress field under uniaxial loading N_x, $R/a = 0.3$: (a) (JING; DUAN, 2023). (b) FEM. (c) Present. These values do not have specific units of measurement but are instead reference values relative to N_x.
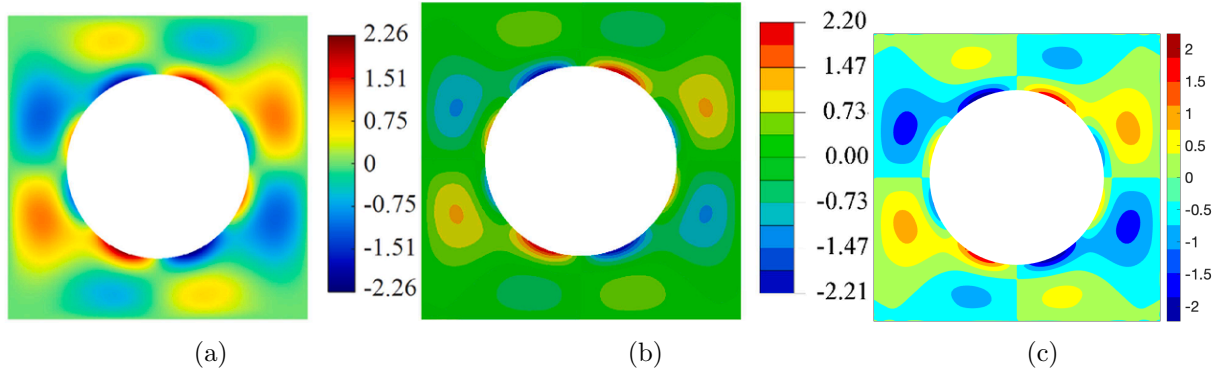
FIGURE 5.9 – Representative figure of the $\bar{N}_{xy}$ stress field under uniaxial loading N_x, $R/a = 0.3$: (a) (JING; DUAN, 2023). (b) FEM. (c) Present. These values do not have specific units of measurement but are instead reference values relative to N_x.

Simulations were conducted for various loading conditions, including uniaxial (in the x-axis direction), biaxial, and pure shear loading. Three boundary conditions—SSSS, CCCC, and CFCF—were applied to the plate's four edges 1234 (1-left, 2-down, 3-right, 4-up) in a counterclockwise direction. In these simulations, $I = J = 30$ terms were used in the admissible function and 292×292 Gauss points for numerical integration in the calculation of the integrals that compose the prebuckling and buckling analyses. The normalized critical buckling load results for the simulated boundary conditions and loading modes, with $R/a = 0.3$, as well as comparisons with data from the literature in (JING; DUAN, 2023) and (ABOLGHASEMI *et al.*, 2019) and by FEM, can be verified in Table 5.6.

TABLE 5.6 – Normalized critical buckling load results $\lambda_{cr} = N_{cr}a^2/(D_1\pi^2)$ for the plate under uniaxial, biaxial, and pure shear loading. The error calculated with respect to the results obtained through FEM is given by: Error $= (\lambda_{cr} - \lambda_{\text{FEM}})/\lambda_{\text{FEM}}$.

Boundary condition	Loading mode	R/a	Present	Error [%] (Present)	(JING; DUAN, 2023)	Error [%] (JING; DUAN, 2023)	(ABOLGHASEMI *et al.*, 2019)	Error [%] (ABOLGHASEMI *et al.*, 2019)	FEM
SSSS	uniaxial N_x	0.3	2.771	0.362	2.790	1.050	2.818	2.064	2.761
CCCC	uniaxial N_x	0.3	7.526	0.226	7.395	-1.518	7.099	-5.460	7.509
CFCF	biaxial	0.3	1.807	-0.055	1.807	-0.055	1.867	3.263	1.808
CCCC	pure shear	0.3	4.408	0.045	4.418	0.272	4.059	-7.876	4.406

As observed in Table 5.6, errors starting from 0.045% were obtained for the case with CCCC boundary condition and pure shear loading, and up to 0.362% for the case with SSSS boundary condition and uniaxial loading of N_x in relation to the finite element analysis. Additionally, the results were consistent with those predicted in the literature.

The normalized critical buckling load results for the simulated boundary conditions and loading modes considering the first four modes, with $R/a = 0.3$, as well as comparisons with data from the literature in (JING; DUAN, 2023) and by FEM, can be verified in Tables 5.7, 5.8, 5.9, and 5.10.

TABLE 5.7 – Normalized critical buckling load results $\lambda_{cr} = N_{cr}a^2/(D_1\pi^2)$ for a SSSS plate under uniaxial loading N_x with $R/a = 0.3$. The error calculated with respect to the results obtained through FEM is given by: Error $= (\lambda_{cr} - \lambda_{\text{FEM}})/\lambda_{\text{FEM}}$.

Mode	Present	Error [%] (Present)	(JING; DUAN, 2023)	Error [%] (JING; DUAN, 2023)	FEM
1	2.771	0.362	2.790	1.050	2.761
2	3.905	0.670	3.935	1.444	3.879
3	4.164	0.653	4.175	0.919	4.137
4	5.640	0.913	5.665	1.360	5.589

TABLE 5.8 – Normalized critical buckling load results $\lambda_{cr} = N_{cr}a^2/(D_1\pi^2)$ for a CCCC plate under uniaxial loading N_x with $R/a = 0.3$. The error calculated with respect to the results obtained through FEM is given by: Error $= (\lambda_{cr} - \lambda_{\text{FEM}})/\lambda_{\text{FEM}}$.

Mode	Present	Error [%] (Present)	(JING; DUAN, 2023)	Error [%] (JING; DUAN, 2023)	FEM
1	7.526	0.226	7.395	-1.518	7.509
2	7.647	0.091	7.693	0.694	7.640
3	7.673	0.092	7.842	2.296	7.666
4	7.778	0.232	8.352	7.629	7.760

TABLE 5.9 – Normalized critical buckling load results $\lambda_{cr} = N_{cr}a^2/(D_1\pi^2)$ for a CFCF plate under biaxial loading with $R/a = 0.3$. The error calculated with respect to the results obtained through FEM is given by: Error $= (\lambda_{cr} - \lambda_{\text{FEM}})/\lambda_{\text{FEM}}$.

Mode	Present	Error [%] (Present)	(JING; DUAN, 2023)	Error [%] (JING; DUAN, 2023)	FEM
1	1.807	-0.055	1.807	-0.055	1.808
2	1.808	-0.055	1.808	-0.055	1.809
3	3.881	0.052	3.918	1.005	3.879
4	3.962	0.051	4.010	1.263	3.960

TABLE 5.10 – Normalized critical buckling load results $\lambda_{cr} = N_{cr}a^2/(D_1\pi^2)$ for a CCCC plate under pure shear loading with $R/a = 0.3$. The error calculated with respect to the results obtained through FEM is given by: Error $= (\lambda_{cr} - \lambda_{\text{FEM}})/\lambda_{\text{FEM}}$.

Mode	Present	Error [%] (Present)	(JING; DUAN, 2023)	Error [%] (JING; DUAN, 2023)	FEM
1	4.408	0.045	4.418	0.272	4.406
2	4.419	0.023	4.440	0.498	4.418
3	6.227	0.032	6.258	0.530	6.225
4	6.311	0.048	6.369	0.967	6.308

It is significant to note that these modes align well with those predicted in the literature (JING; DUAN, 2023) and (ABOLGHASEMI *et al.*, 2019), as well as by the FEM for various loading and boundary conditions. This consistency of results is achieved despite the limitations of a semi-analytical model, which implements a meshfree method of solution based on the Discrete Ritz Method. Consequently, the verification of a plate with a cutout was considered satisfactory in this work.

Furthermore, for the case containing stiffeners, the model will be validated according to finite element analysis and experimental tests, considering specific geometric characteristics of the stiffeners and their arrangement along the plate.

The normalized absolute out-of-plane displacements for the first four modes for the simulated boundary conditions and loading modes, with $R/a = 0.3$, as well as comparisons with FEM, can be verified in Figures 5.10, 5.11, 5.12, and 5.13. Note that the behavior of the out-of-plane displacements showed good correlation between those obtained through the implemented model and those obtained through finite element analysis.

(a) $\lambda = 2.771$.   (b) $\lambda = 2.761$.   (c) $\lambda = 3.905$.   (d) $\lambda = 3.879$.

(e) $\lambda = 4.164$.   (f) $\lambda = 4.137$.   (g) $\lambda = 5.640$.   (h) $\lambda = 5.589$.
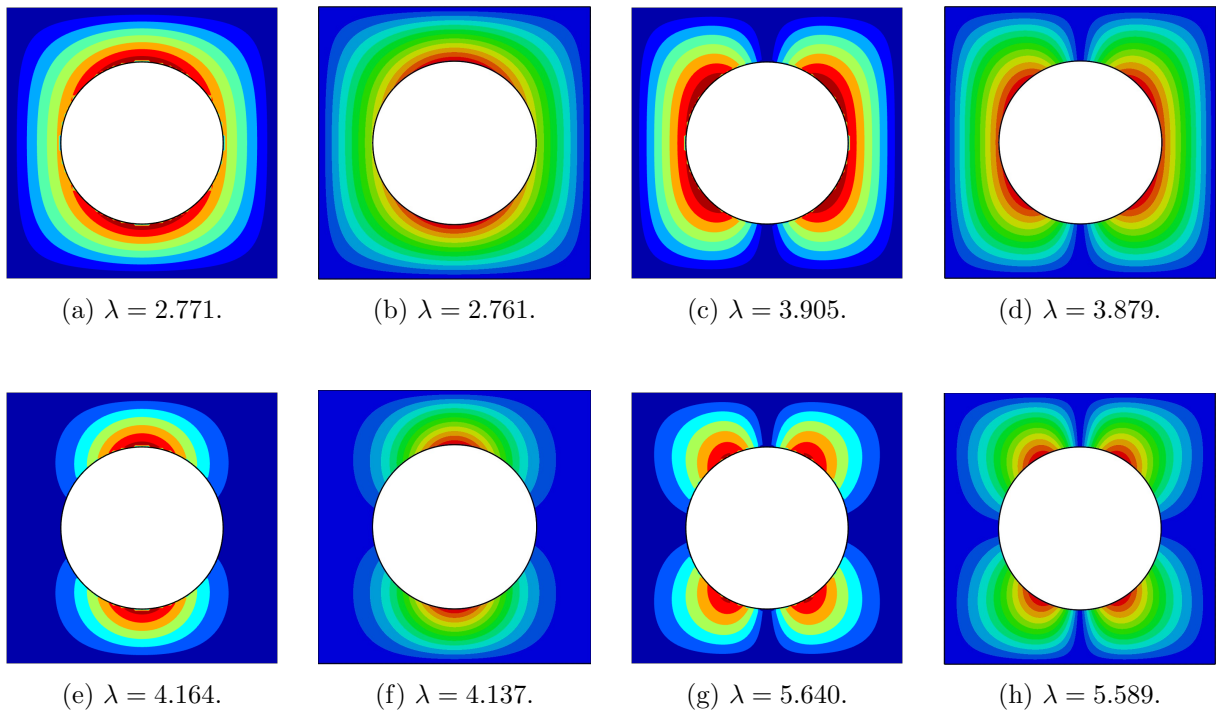
FIGURE 5.10 – Normalized absolute out-of-plane displacements for the uniaxial loading N_x, SSSS, $R/a = 0.3$. (a) 1° mode (Present). (b) 1° mode (FEM).(c) 2° mode (Present). (d) 2° mode (FEM). (e) 3° mode (Present). (f) 3° mode (FEM). (g) 4° mode (Present). (h) 4° mode (FEM).

(a) $\lambda = 7.526$.   (b) $\lambda = 7.509$.   (c) $\lambda = 7.647$.   (d) $\lambda = 7.640$.

(e) $\lambda = 7.673$.   (f) $\lambda = 7.666$.   (g) $\lambda = 7.778$.   (h) $\lambda = 7.760$.
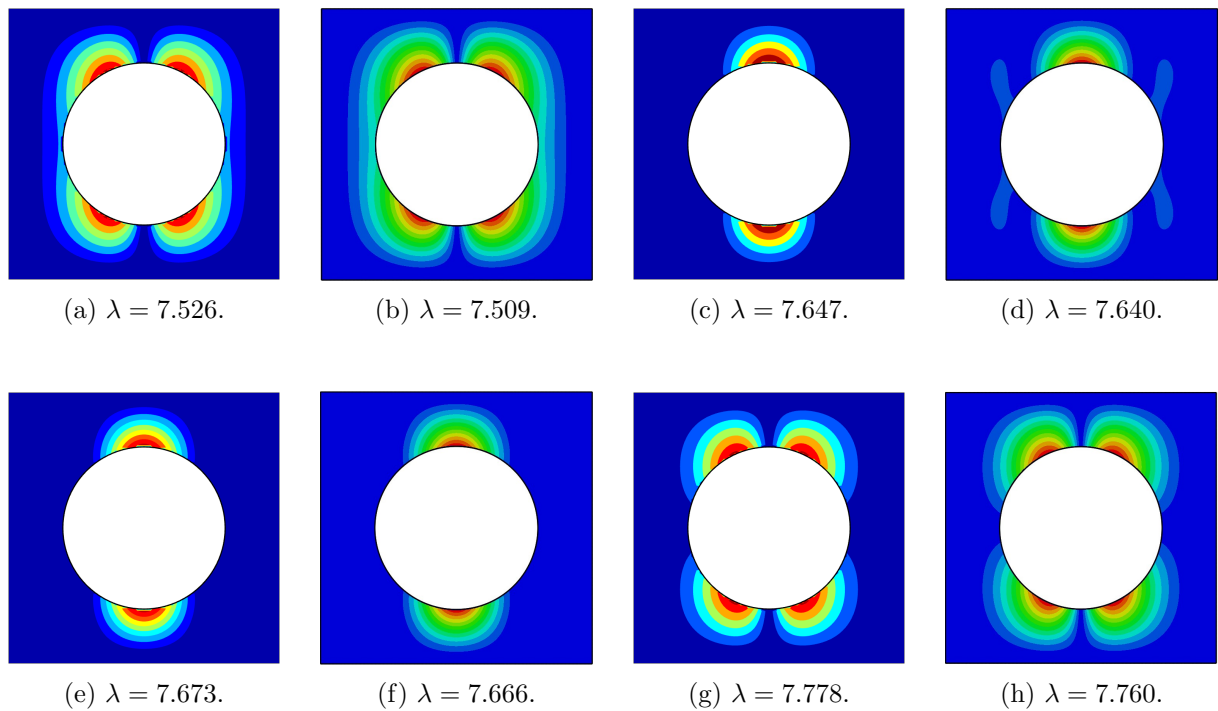
FIGURE 5.11 – Normalized absolute out-of-plane displacements for the uniaxial loading N_x, CCCC, $R/a = 0.3$. (a) 1° mode (Present). (b) 1° mode (FEM).(c) 2° mode (Present). (d) 2° mode (FEM). (e) 3° mode (Present). (f) 3° mode (FEM). (g) 4° mode (Present). (h) 4° mode (FEM).

(a) $\lambda = 1.807$.   (b) $\lambda = 1.808$.   (c) $\lambda = 1.808$.   (d) $\lambda = 1.809$.

(e) $\lambda = 3.881$.   (f) $\lambda = 3.879$.   (g) $\lambda = 3.962$.   (h) $\lambda = 3.960$.
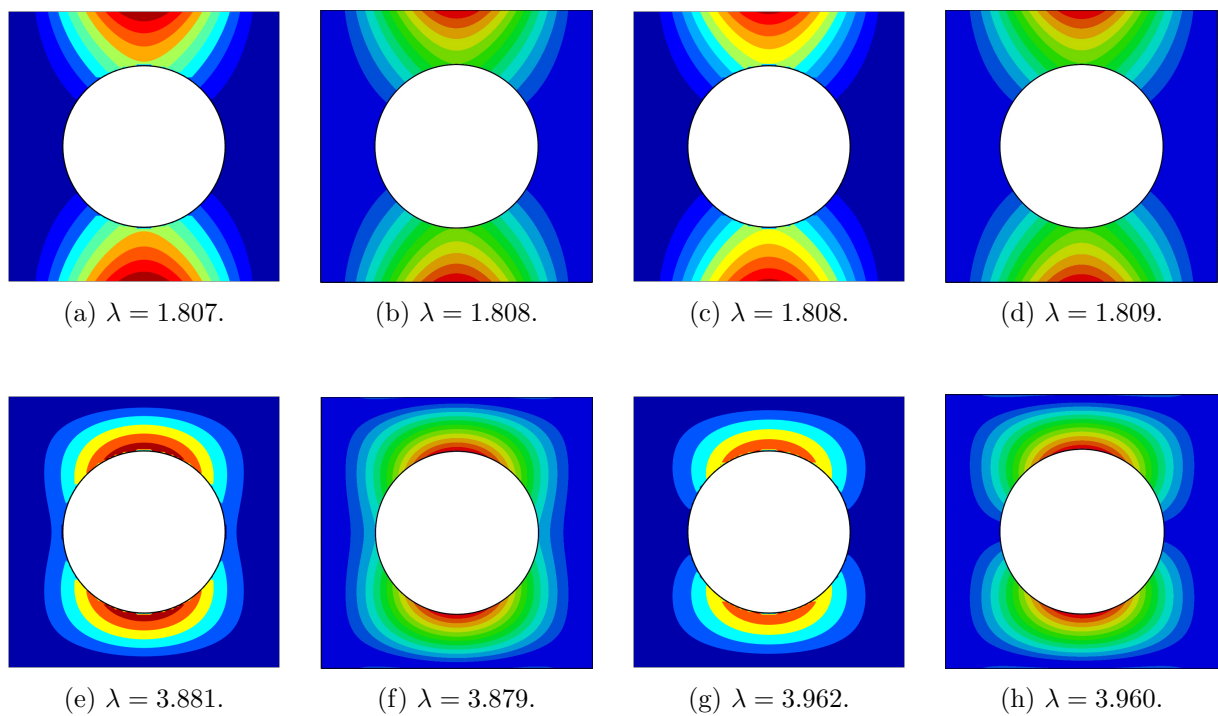
FIGURE 5.12 – Normalized absolute out-of-plane displacements for the biaxial loading, CFCF, $R/a = 0.3$. (a) 1° mode (Present). (b) 1° mode (FEM).(c) 2° mode (Present). (d) 2° mode (FEM). (e) 3° mode (Present). (f) 3° mode (FEM). (g) 4° mode (Present). (h) 4° mode (FEM).

(a) $\lambda = 4.408$.   (b) $\lambda = 4.406$.   (c) $\lambda = 4.419$.   (d) $\lambda = 4.418$.

(e) $\lambda = 6.227$.   (f) $\lambda = 6.225$.   (g) $\lambda = 6.311$.   (h) $\lambda = 6.308$.
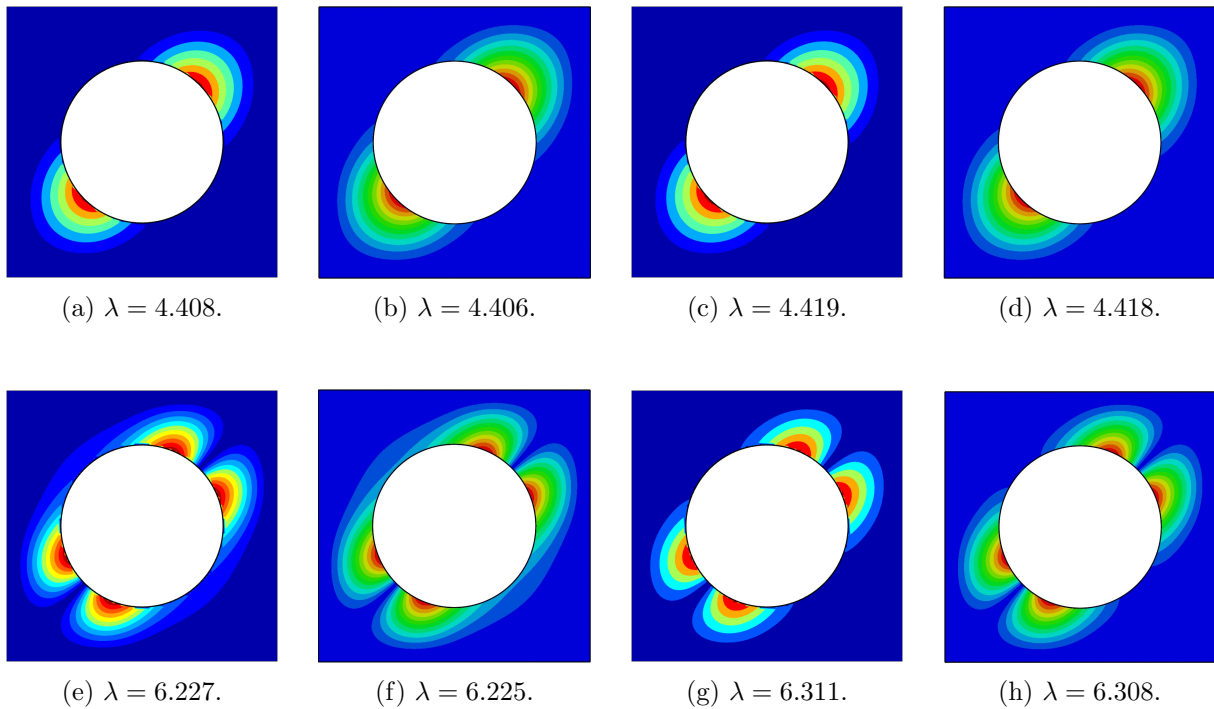
FIGURE 5.13 – Normalized absolute out-of-plane displacements for the pure shear loading, CCCC, $R/a = 0.3$. (a) 1° mode (Present). (b) 1° mode (FEM).(c) 2° mode (Present). (d) 2° mode (FEM). (e) 3° mode (Present). (f) 3° mode (FEM). (g) 4° mode (Present). (h) 4° mode (FEM).

An interesting fact is that the case with the SSSS boundary condition did not converge for $I = J = 30$ with 292×292 Gauss points. The procedure adopted in this case was to remove rows and columns from the stiffness matrices associated with the problem to $I' = J' = 20$ in order to achieve convergence for 292×292 Gauss points. Despite this, the case with SSSS produced excellent results, presenting an error of 0.362% in its critical buckling load compared to FEM. It is noteworthy that the methodology of reducing the solution of problems to $I' < I$ and $J' < J$, in addition to playing an important role in the study of convergence, can also provide insights into the relationship between the convergence of I, J and the number of Gauss points, without the need to perform multiple integration sets for smaller values of I' and J' for a given number of Gauss points.

In addition, the simulation for the boundary condition CFCF did not converge with $I = J = 30$ and 292×292 Gauss points. However, the computational strategy of calculating results for $I' < I$ and $J' < J$ was employed, achieving excellent results for $I' = J' = 29$ and 292×292 points, with only a few additional seconds required. This, indeed, provides a significant advantage in convergence analysis while maximizing the use of limited computational resources.

6 Experimental Test Setup

The experimental test presented in this master's dissertation was conducted at the Instituto Tecnológico de Aeronáutica (ITA), specifically in the Laboratory of Aerospace Structures. Within this framework, as will be shown later, a series of experiments were undertaken, each involving distinct configurations of a square plate under pure shear loading, using a picture frame testing jig:

- **Configuration I**: A square plate under diagonal tensile loading.

- **Configuration II**: A square plate with a circular cutout, also under diagonal tensile loading.

- **Configuration III**: A square plate with a circular cutout and reinforced with two stiffeners, under diagonal tensile loading.

Visual representations of the experimental setups for these configurations are provided in Figures 6.1 and 6.2.

(a)   (b)   (c)
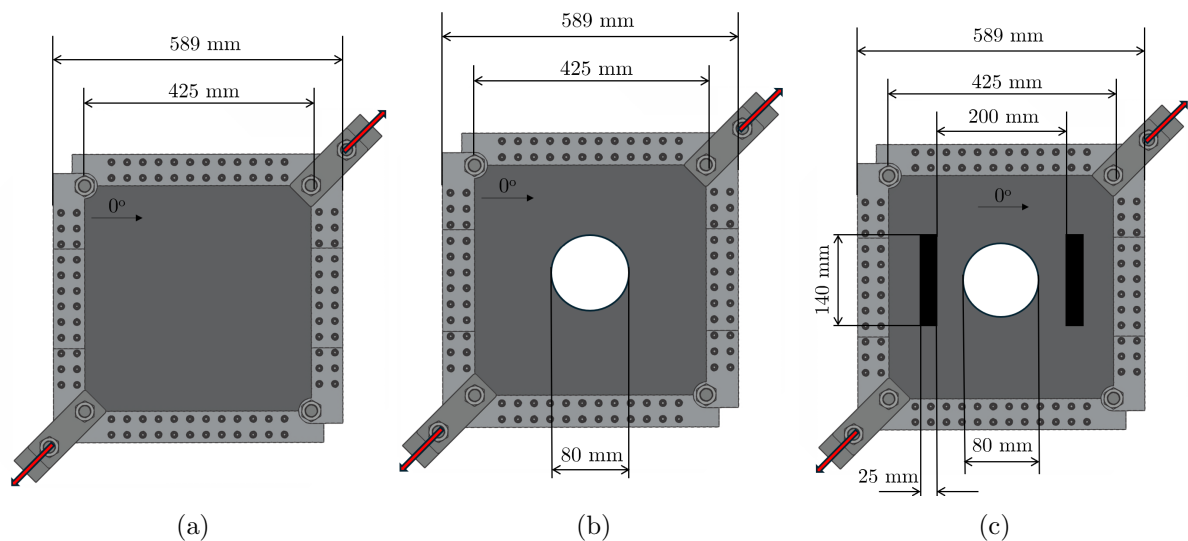
FIGURE 6.1 – Representative figure of the three experiments conducted in the structural laboratory of ITA. (a) Plate. (b) Plate with a circular cutout. (c) Plate with a circular cutout and two stiffeners.
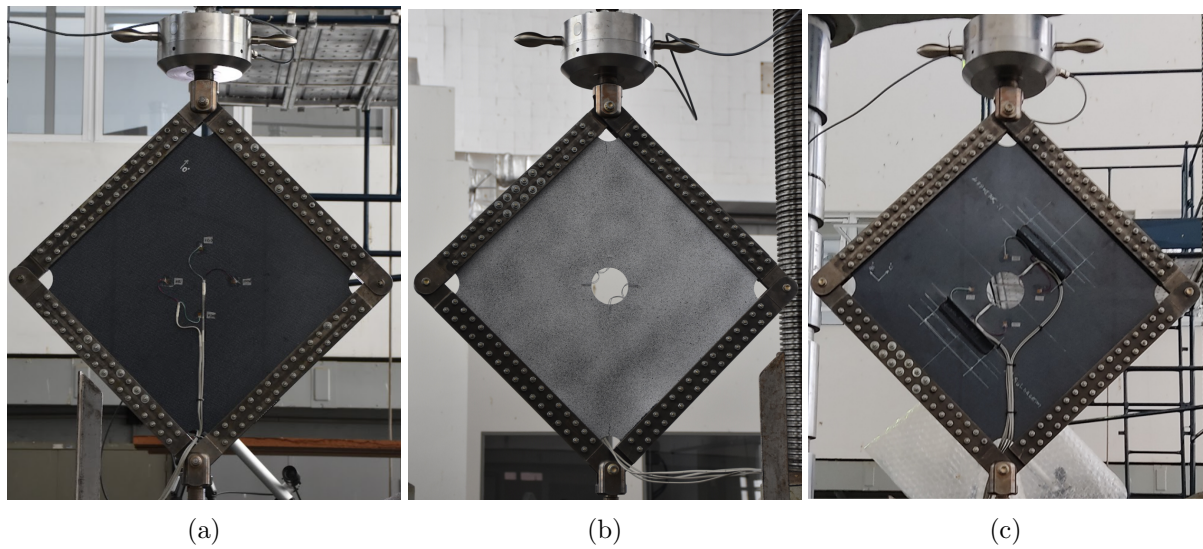
FIGURE 6.2 – Photographs taken from the three experiments conducted in the structural laboratory of ITA. (a) Plate. (b) Plate with a circular cutout. (c) Plate with a circular cutout and two stiffeners.
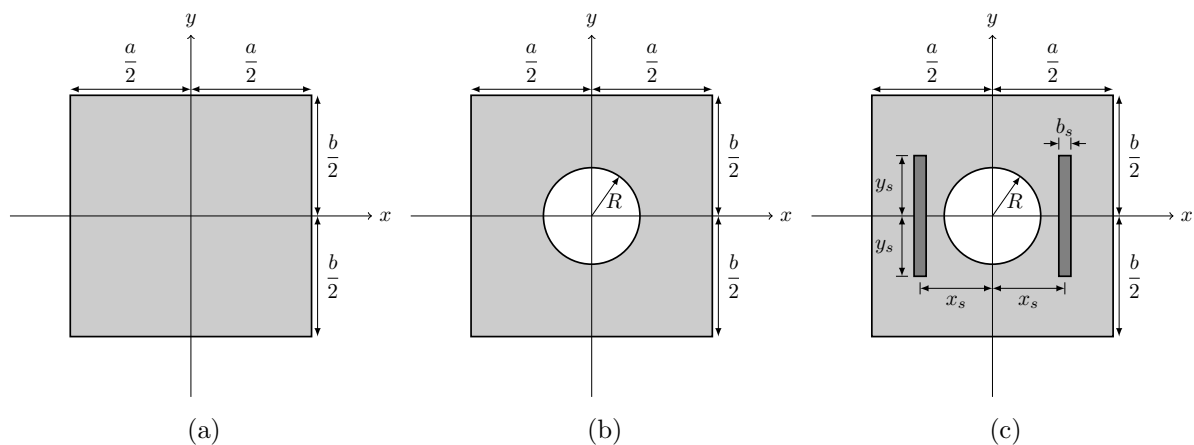
FIGURE 6.3 – Representative figure of the geometric characteristics of the three experiments conducted in the structural laboratory of ITA. (a) Plate. (b) Plate with a circular cutout. (c) Plate with a circular cutout and two stiffeners.

The properties of the thermoplastic composite material used in the plate and stiffeners were assessed through the FINEP SPIRIT FLY Project, an industry-led R&D collaboration between Brazil (ALLTEC) and The Netherlands (TORAY Advanced Composites). This project aims to develop a thermoplastic-based demonstrator component that meets Embraer's functional, technical, production, and financial requirements. These measurements were conducted in the Laboratory of Aerospace Structures at Instituto Tecnológico de Aeronáutica (ITA) and can be found in Table 6.1. Furthermore, the stacking configuration and geometric characteristics are shown in Table 6.2. Additionally, the geometric characteristics of the stiffeners were modeled mathematically as shown in Figure 6.4.

TABLE 6.1 – Material properties of the plate and stiffeners utilized in the tests.

Material	E_1 [GPa]	E_2 [GPa]	G_{12} [GPa]	G_{13} [GPa]	G_{23} [GPa]	ν_{12}
TC 1225/ Carbon T300JB 3K 5HS	55.549	55.549	3.773	3.773	3.773	0.052

TABLE 6.2 – Table containing the geometric characteristics of the panels modeled in the three experiments, along with the stacking configuration of the plate and stiffeners.

Stacking	a [mm]	b [mm]	t [mm]	h [mm]	R [mm]	x_s [mm]	y_s [mm]	d_s [mm]	b_s [mm]
$[(0,90)/(+45,-45)]_{2s}$ (8 plies)	425	425	0.31	2.48	40	112.5	70	27.5	25
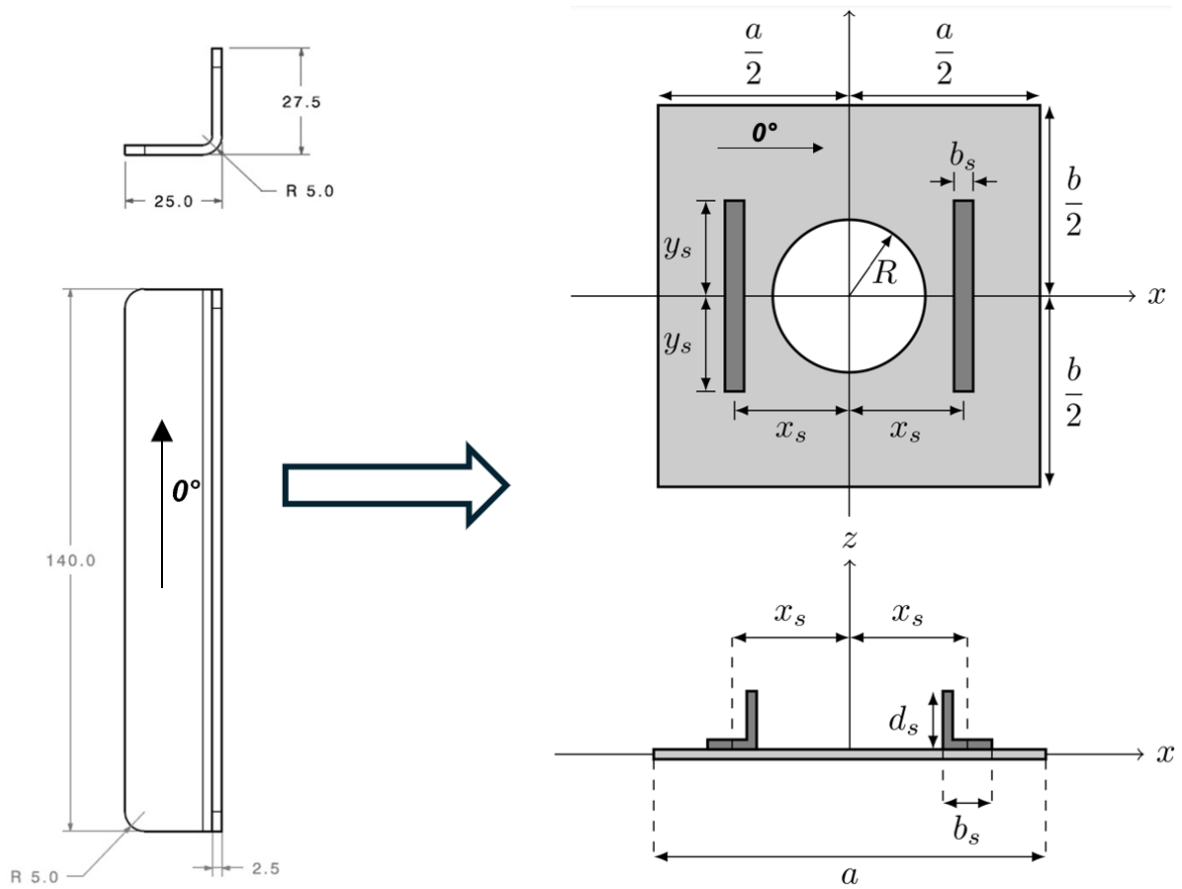
FIGURE 6.4 – Representative figure of the actual geometric characteristics of the stiffeners on the left, alongside their idealization used in the implemented model on the right, as well as the geometric characteristics of the stiffened panel with a circular cutout.

A 3D Digital Image Correlation (DIC) system provided by Dantec Dynamics was employed, offering imagery of the out-of-plane displacement field. This technique captures a sequence of images detailing the surface deformation of the test specimen. Typically, the surface is marked with a stochastic speckle pattern, enhancing the capability to monitor distinct points across successive images. Through the comparative analysis of images pre and post-deformation, the DIC software is capable of generating comprehensive maps of displacement and strain across the surface. Utilizing two or more cameras, the 3D DIC

method captures the specimen's surface from varied perspectives, facilitating the generation of three-dimensional reconstructions of displacement and strain fields. This advanced methodological approach enables precise measurement and analysis of the mechanical behaviors of materials and structures when subjected to specific loading conditions, thus yielding critical insights into their characteristics and performance. Moreover, the stacking sequence configuration of the plate and the stiffeners is visually represented in Figure 6.5.
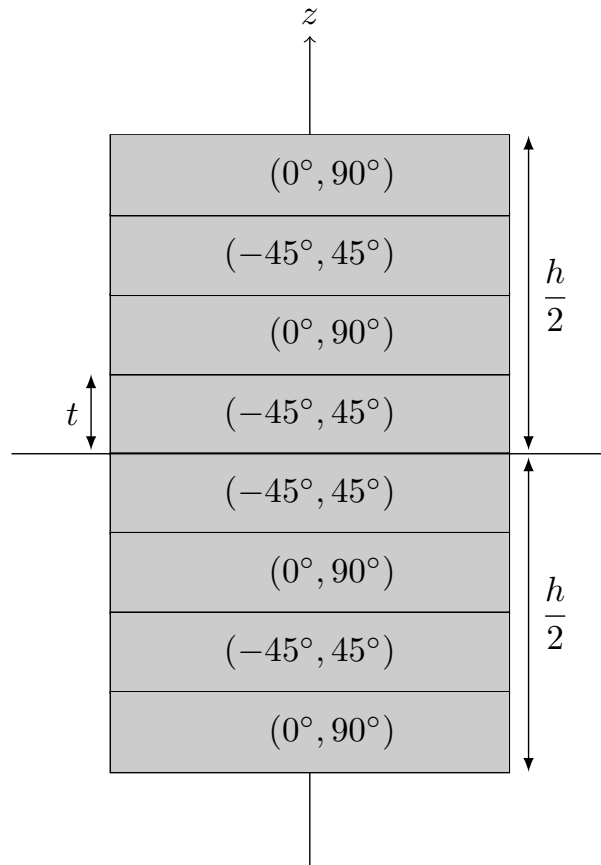
FIGURE 6.5 – Representative figure of the quasi-isotropic stacking sequence configuration of the plate and the stiffeners.

The apparatus used with a 3D Digital Image Correlation setup by Dantec Dynamics during the tests, as well as the assembly of the panel and picture frame on the testing apparatus during the tests, are presented in the photographs taken in the structural laboratory of ITA, as shown in Figures 6.6 and 6.7, respectively.
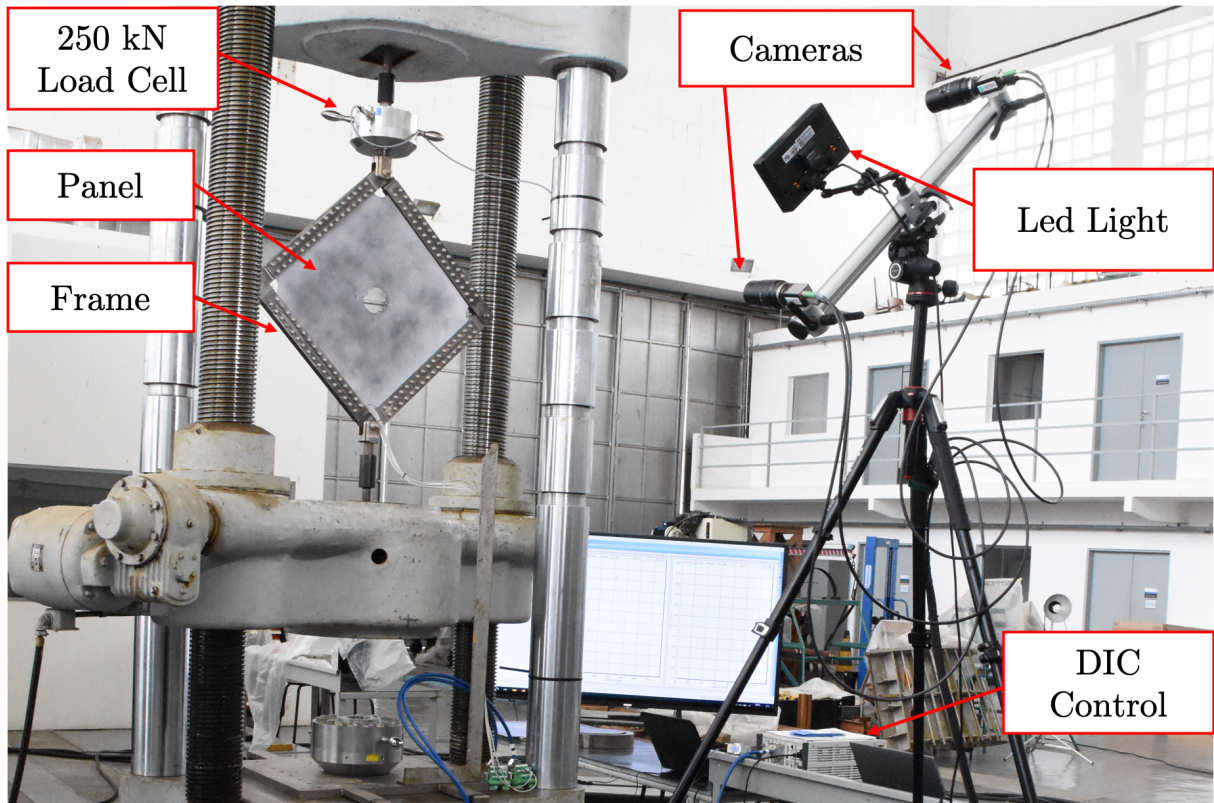
FIGURE 6.6 – Figure obtained from a photograph taken in the structural laboratory of ITA, showcasing the apparatus used with a 3D Digital Image Correlation setup by Dantec Dynamics during the tests.

FIGURE 6.7 – Figure obtained from a photograph captured in the structural laboratory of ITA, showcasing the setup apparatus, including the assembly of the panel and picture frame on the testing apparatus during the tests.

The experimental setups were instrumented by affixing strain gauges to both surfaces of the plates, a configuration depicted in Figures 6.8 and 6.9. Specifically, 45° back-to-back strain gauges were positioned 70 mm from the center, utilizing the Micro Measurement CEA 06 125UW 350 model with a gauge factor of 2.175. Data acquisition occurred in real-time at a frequency of 10 Hz.

(a)   (b)
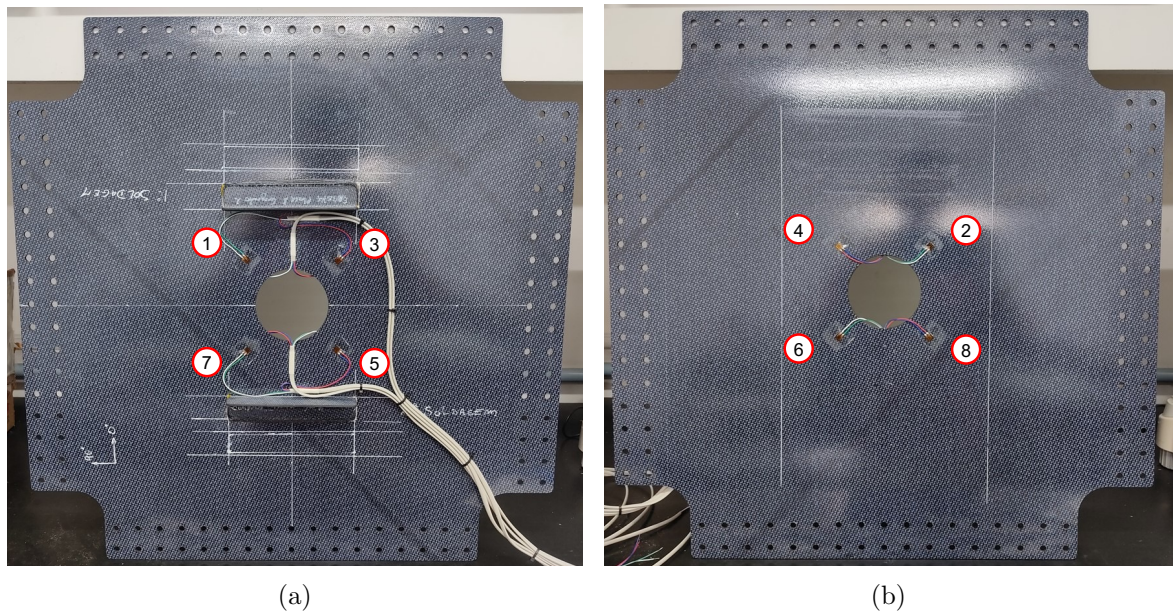
FIGURE 6.8 – Representative figure showing the positioning of strain gauges on both sides of the plate during all testing cases.
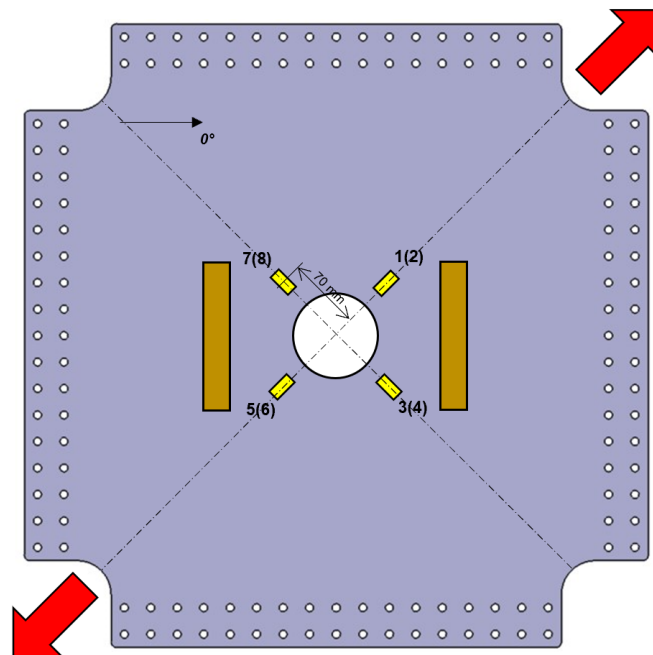
FIGURE 6.9 – Representative figure showing the positioning of strain gauges on the plate during all testing cases.

6.1   Procedure to Obtain the Critical Buckling

In the buckling test, deformation versus load values were obtained for the three experiments conducted using strain gauges, as shown in Figures 6.10, 6.11 and 6.12. With these data, the calculation of membrane deformation (MD) and bending curvature (BC) was conducted for each pair of strain gauges arranged oppositely on the plate, according to:

$$\text{MD}_{ij} = \frac{\text{SG}_i + \text{SG}_j}{2} \quad \text{BC}_{ij} = \frac{\text{SG}_i - \text{SG}_j}{2} \quad (i,j) = (1,2); (3,4); (5,6); (7,8) \tag{6.1}$$
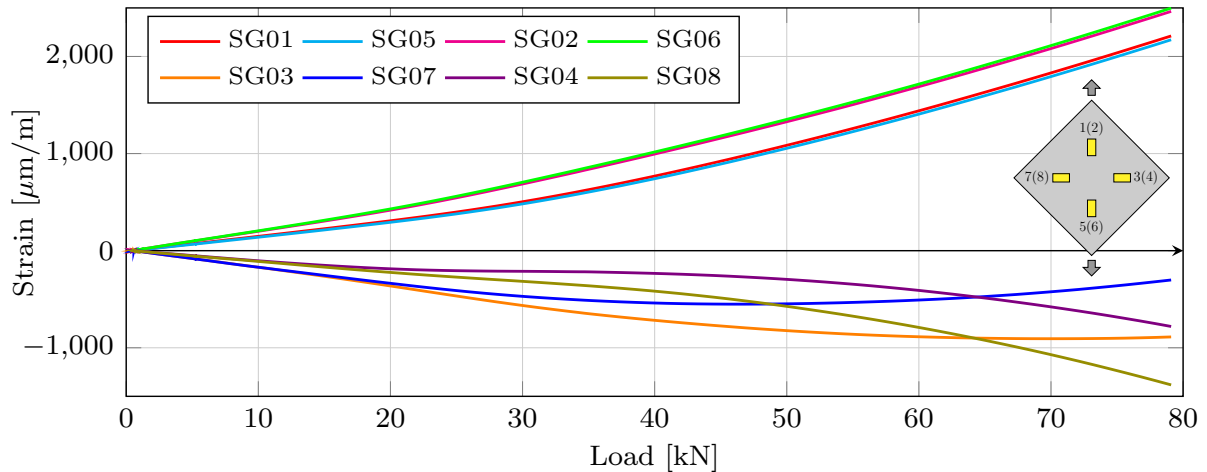
FIGURE 6.10 – Representative figure of the deformations obtained through strain gauges when subjected to a load in the experiment involving the plate.
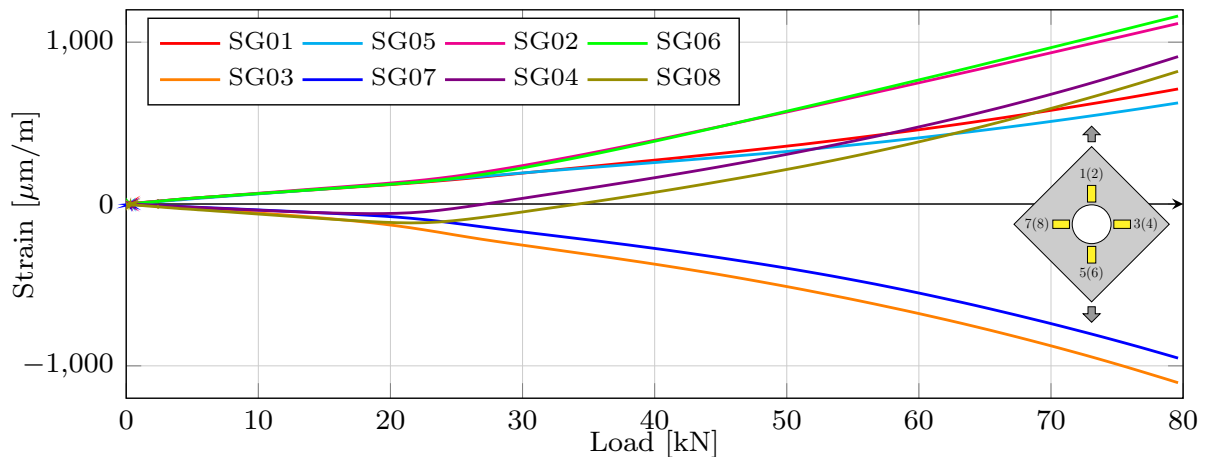
FIGURE 6.11 – Representative figure of the deformations obtained through strain gauges when subjected to a load in the experiment involving the plate with a circular cutout.
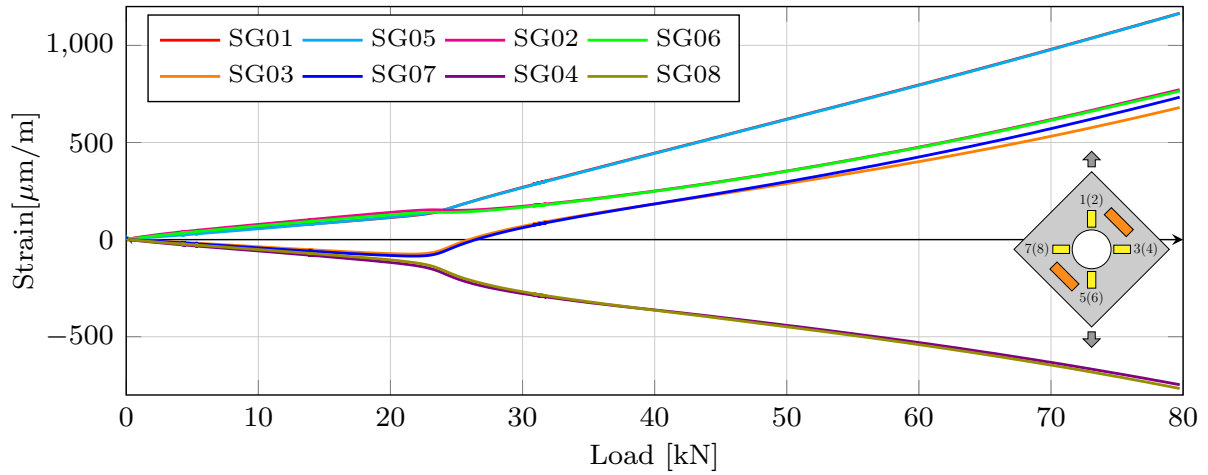
FIGURE 6.12 – Representative figure of the deformations obtained through strain gauges when subjected to a load in the experiment involving the stiffened plate with a circular cutout.

The results obtained through the calculation of membrane deformation and bending curvature from the deformation data derived from the strain gauges, in the experiment involving the plate, the plate with a circular cutout, and the stiffened plate with a circular cutout, are represented in Figures 6.13, 6.14, and 6.15, respectively.
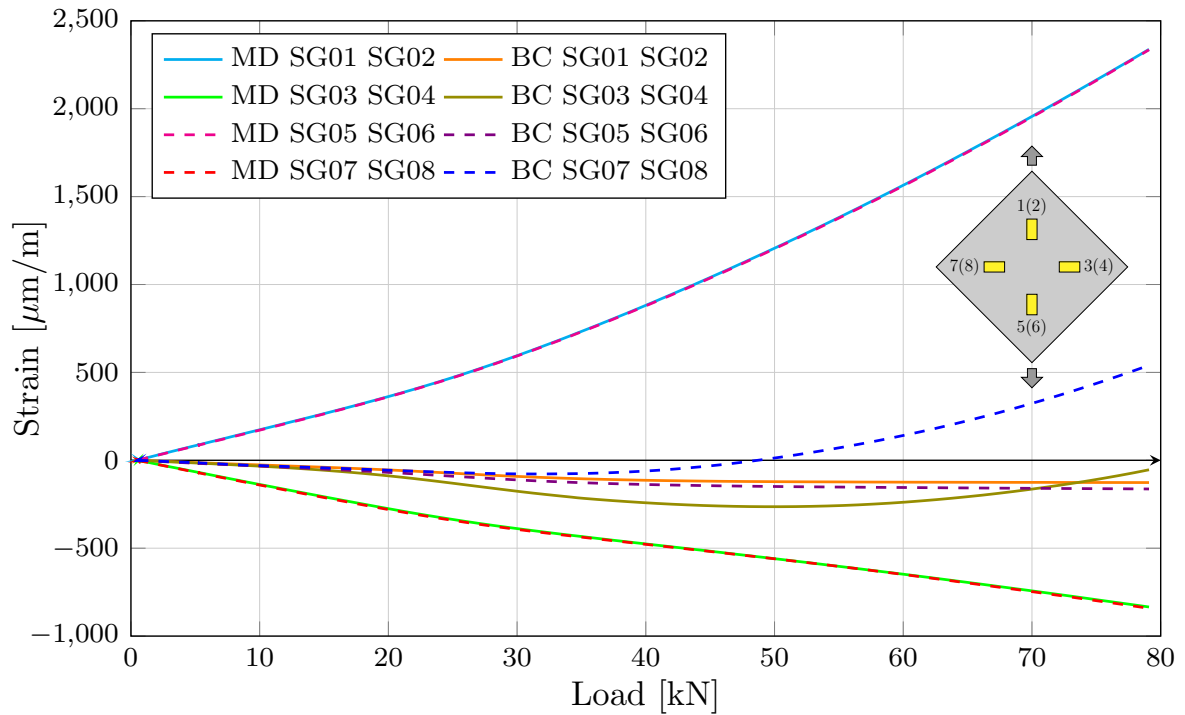
FIGURE 6.13 – Figure obtained through the calculation of membrane deformation and bending curvature from the deformation data derived from the strain gauges in the experiment involving the plate.
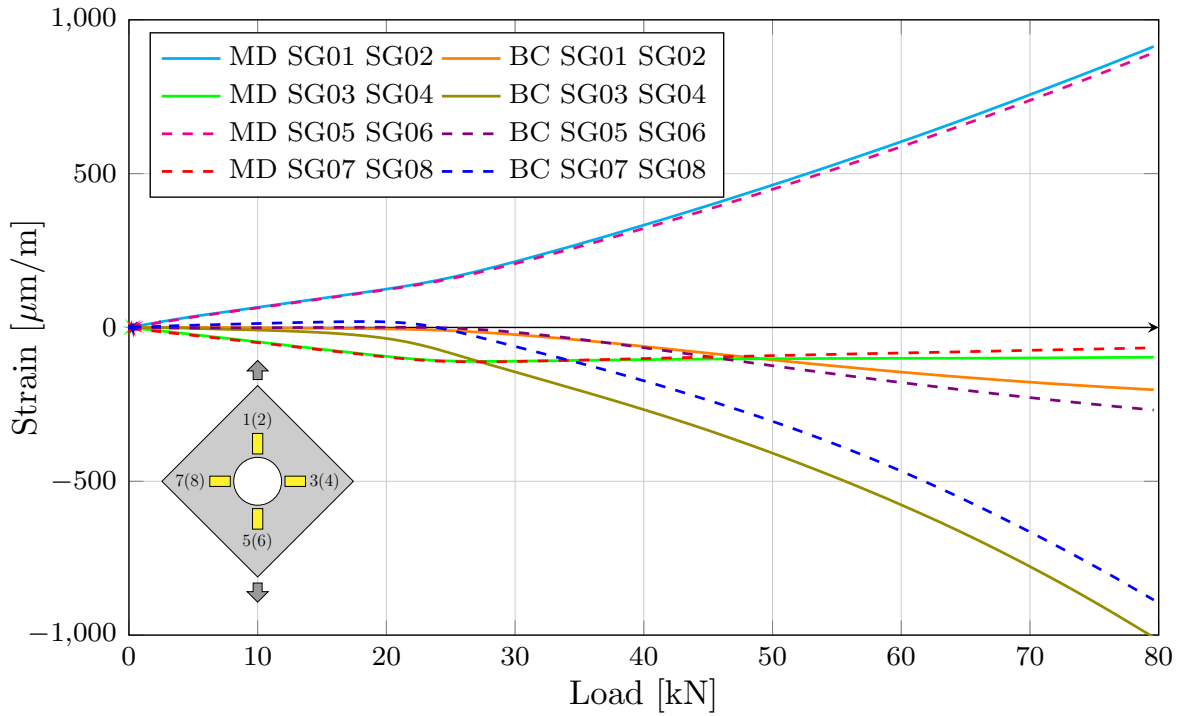
FIGURE 6.14 – Figure obtained through the calculation of membrane deformation and bending curvature from the deformation data derived from the strain gauges in the experiment involving the plate with a circular cutout.
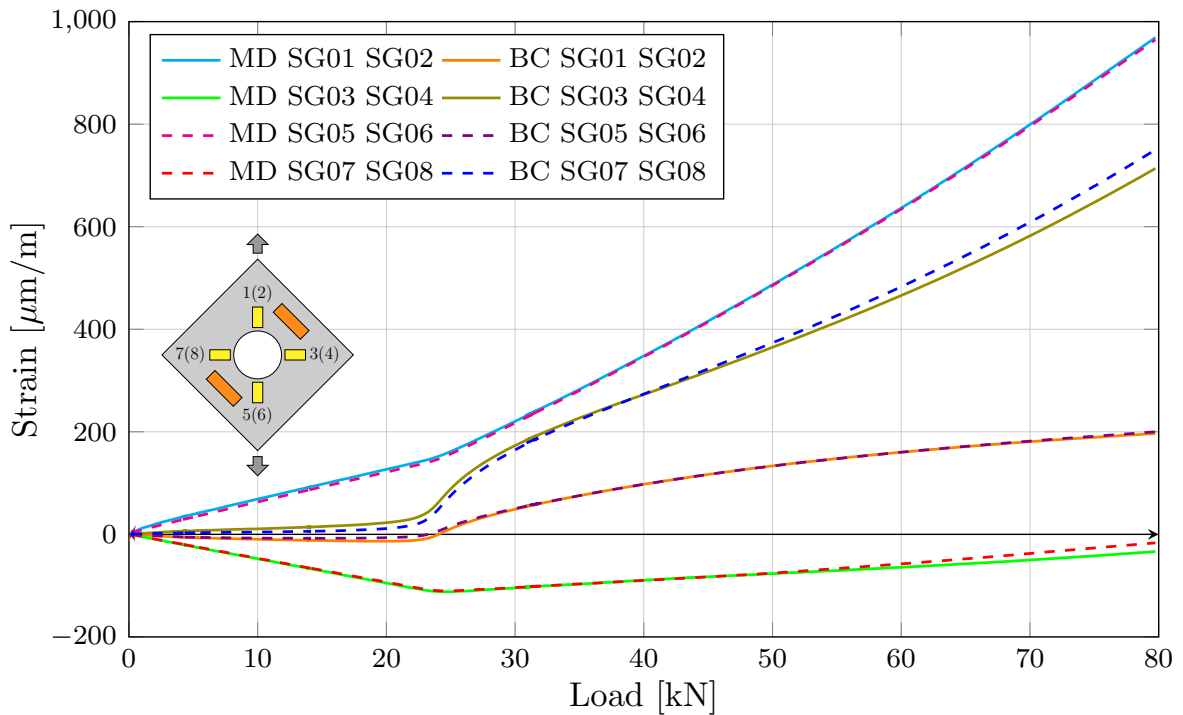
FIGURE 6.15 – Figure obtained through the calculation of membrane deformation and bending curvature from the deformation data derived from the strain gauges, in the experiment involving the stiffened plate with a circular cutout.

As noted by (SINGER *et al.*, 1998), accurately determining the critical stress in plate

buckling can be challenging due to the stable post-buckling behavior of plates. Conse-
quently, various methods have been employed to define buckling stress or load, as docu-
mented in the literature.

In this study, the inflection point method, as proposed by (SINGER *et al.*, 1998), was
selected to determine the critical load in all three experiments. This method identifies the
least slope on the load-deflection curve, which closely aligns with the theoretical buckling
load. For perfectly flat plates, this slope is zero at buckling. However, for imperfect
plates, the method yields a slightly higher buckling load than the top-of-the-knee method
and relies less on individual judgment (SINGER *et al.*, 1998). According to (SINGER *et al.*,
1998), the inflection point method produces satisfactory results if the initial imperfection
is not excessive. Additionally, it can be applied to load versus strain difference $(\varepsilon_1 - \varepsilon_2)$
curves. The procedure used in these experiments is illustrated in Figure 6.16.
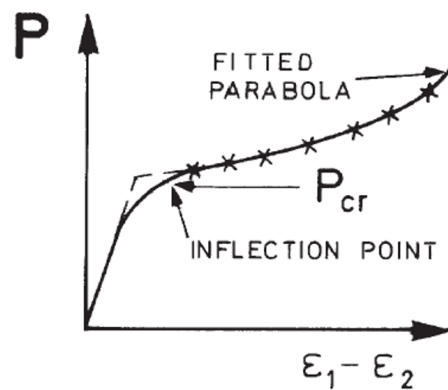
FIGURE 6.16 – Representative figure of the Inflection Point method. Source: (SINGER *et al.*, 1998).

The illustration of the inflection point method applied to bending curvature, in the
experiments involving the plate, the plate with a circular cutout, and the stiffened plate
with a circular cutout, can be verified in Figures 6.17, 6.18, and 6.19, respectively. The
figures below demonstrate that critical buckling occurs through the bending curvature
measured by strain gauges S03/S04 and S07/S08. For the plate, buckling was detected
only by strain gauges SG03/SG04, which was confirmed by DIC vertical displacement
data, showing characteristic buckling behavior at a load of 23.54 kN.

For the plate with cutout and stiffened plate with cutout cases, critical buckling values
were obtained from the bending curvature of strain gauges SG03/SG04 and SG07/SG08.
The final value was taken as the average of these measurements, considering their prox-
imity.
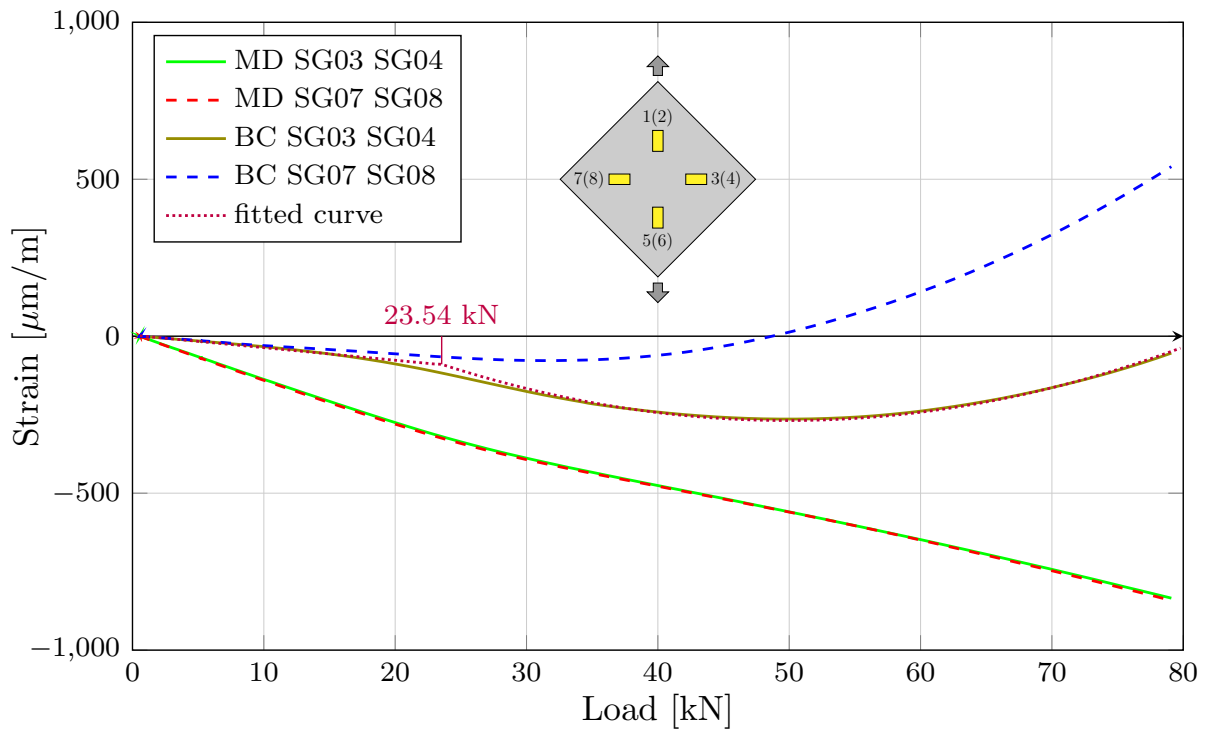
FIGURE 6.17 – Illustration of the inflection point method applied to bending curvature, concerning strain gauges SG03/SG04, in the experiment involving the plate.
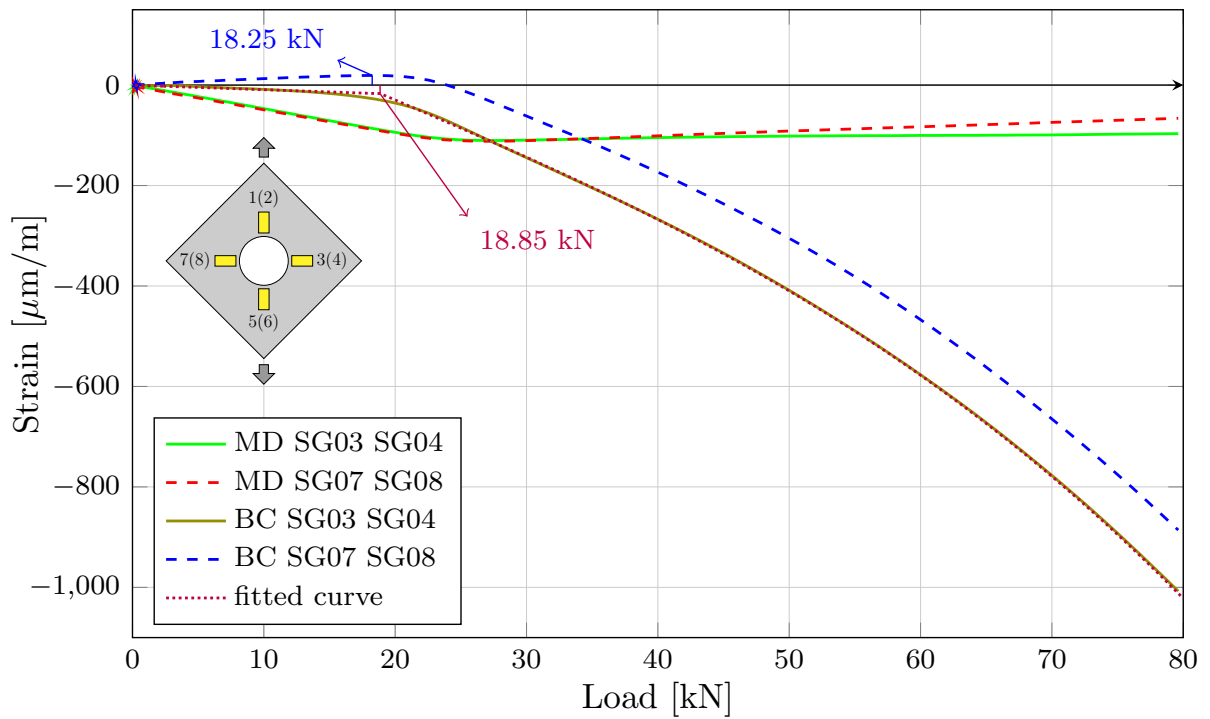
FIGURE 6.18 – Illustration of the inflection point method applied to bending curvature, concerning strain gauges SG03/SG04 and SG07/SG08, in the experiment involving the plate with a circular cutout.
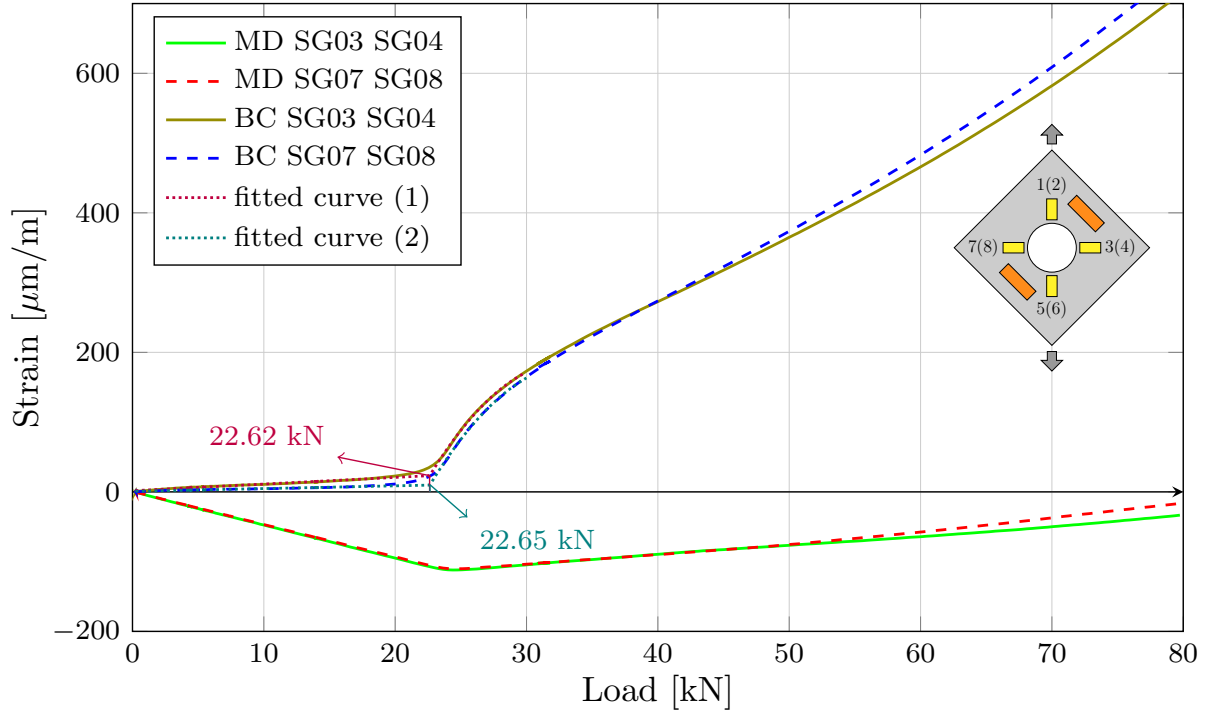
FIGURE 6.19 – Illustration of the inflection point method applied to bending curvature, concerning strain gauges SG03/SG04 and SG07/SG08, in the experiment involving the stiffened plate with a circular cutout.

The panel is subjected to shear loading N_{xy}, which correlates with P_{cr} according to Eq. 6.2 (SILVA, 2021). The experimental critical buckling values are shown in Table 6.3.

$$N_{xy} = P_{cr}\frac{\cos(45°)}{a} = \frac{P_{cr}}{a\sqrt{2}} \tag{6.2}$$

TABLE 6.3 – Results of critical buckling, obtained from the conducted experiments.

Experiment	P_{cr} SG-03/SG-04 [kN]	P_{cr} SG-07/SG-08 [kN]	P_{cr} [kN]	N_{xy} [kN/m]
Plate	23.54	-	23.54	39.17
Plate with circular cutout	18.85	18.25	18.55	30.86
Stiffened plate with circular cutout	22.62	22.65	22.64	37.67

Notably, the critical buckling load for the stiffened plate with a cutout was 22.64 kN, which is lower than the 23.54 kN for the plate. This suggests that the stiffener did not adequately compensate for the cutout's effect on the critical buckling load. Comparisons and observations related to FEM, the implemented model, and the experiment will be discussed in Chapter 7 (Results and Discussions).

7 Results and Discussions

7.1 Boundary Conditions for All Scenarios

Computational simulations of the semi-analytical model were conducted based on the idealization of a composite panel using a picture frame testing jig under pure shear loading, with all edges of the plates clamped (CCCC). These simulations correspond to the three configurations tested experimentally, as described in Chapter 6: the plate, the plate with a circular cutout, and the stiffened plate with a circular cutout. These simulations utilized the adopted semi-analytical model implemented in MATLAB®, with $I = J = 30$ terms and 292×292 Gauss points. Additionally, the simulations were implemented using FEM (Abaqus®). Subsequently, the results were compared, as will be presented throughout this chapter. The hierarchical polynomials used in these simulations are shown in Table 7.1.

TABLE 7.1 – Table showing the procedure adopted to obtain the CCCC solution. The polynomials indicated with a value of zero will not be used in the solution.

Variable	ξ				η			
	χ_1	χ_2	χ_3	χ_4	χ_1	χ_2	χ_3	χ_4
u	1	1	1	1	1	1	1	1
v	1	1	1	1	1	1	1	1
w	0	1	0	1	0	1	0	1
φ_u	0	1	0	1	0	1	0	1
φ_v	0	1	0	1	0	1	0	1

7.2 Plate

For the plate, a convergence study of the first four modes was conducted, as shown in Figure 7.1 and Table 7.2, and compared with the critical buckling load calculated using a finite element model, as shown in Figure 7.1. It is noted that for $I = J = 20$, the values

of the buckling modes stabilize.
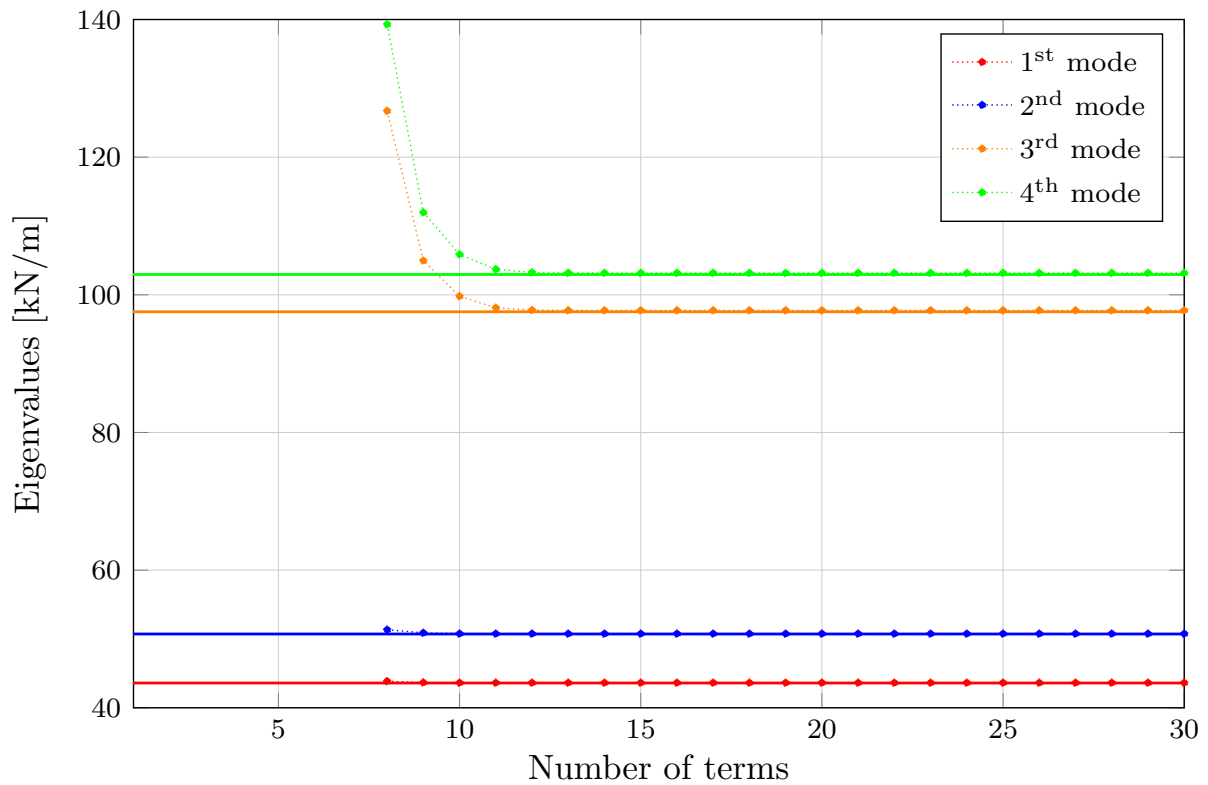
FIGURE 7.1 – Representative figure of the convergence analysis for the plate, using the obtained finite element model values as a reference.

TABLE 7.2 – Buckling loads for the first four modes, in kN/m for the plate as the number of Ritz terms increases.

$I = J$	Mode 1	Mode 2	Mode 3	Mode 4
6	54.5585	79.0902	10401.2963	10774.7727
7	44.4896	53.7530	788.6907	931.5081
8	43.8619	51.3430	126.7262	139.2986
9	43.6746	50.8896	104.9725	111.9621
10	43.6438	50.7764	99.7968	105.8761
11	43.6428	50.7697	98.1187	103.7155
12	43.6424	50.7692	97.7886	103.2491
13	43.6423	50.7691	97.7504	103.1873
14	43.6421	50.7690	97.7439	103.1776
15	43.6421	50.7690	97.7432	103.1764
16	43.6420	50.7690	97.7429	103.1760
17	43.6420	50.7689	97.7429	103.1760
18	43.6419	50.7689	97.7427	103.1758
19	43.6419	50.7689	97.7427	103.1757

$I = J$	Mode 1	Mode 2	Mode 3	Mode 4
20	43.6419	50.7689	97.7426	103.1756
21	43.6419	50.7689	97.7426	103.1756
22	43.6419	50.7688	97.7425	103.1755
23	43.6419	50.7688	97.7425	103.1755
24	43.6419	50.7688	97.7425	103.1755
25	43.6419	50.7688	97.7425	103.1755
26	43.6418	50.7688	97.7424	103.1754
27	43.6418	50.7688	97.7424	103.1754
28	43.6418	50.7688	97.7424	103.1754
29	43.6418	50.7688	97.7424	103.1754
30	43.6418	50.7688	97.7424	103.1754

Furthermore, a FEM analysis containing 20,164 elements was developed. To perform the convergence study, the first four buckling modes were analyzed, as shown in Table 7.3.

TABLE 7.3 – Table containing the convergence analysis of the Finite Element Model (FEM), implemented in the Abaqus® software, showing the buckling loads for the first four modes, in kN/m, for the plate configuration.

Mesh	Number of elements	Mode I	Mode II	Mode III	Mode IV
1	441	45.21	53.10	107.08	113.43
2	1849	43.98	51.28	99.73	105.36
3	7225	43.70	50.86	98.13	103.60
4	11236	43.67	50.81	97.94	103.39
5	20164	43.60	50.72	97.54	102.95

The obtained results are presented in Table 7.4. As shown in Table 7.4, the first four modes obtained through the implemented model showed good agreement with those obtained via FEM, with an error of 0.09% for the first mode and 0.22% for the fourth mode. It is also observed that the error increases for higher modes, as expected. Additionally, both the FEM results and those from the implemented model exhibited errors of 11.31% and 11.41% from the experimental results, respectively.

TABLE 7.4 – Results for the present model with $I = J = 30$ terms and 292×292 Gauss points, and comparisons between the implemented model, FEM and experimental test of the first four buckling modes for the plate. The error with respect to FEM is calculated as $\text{Error}_{\text{FEM}} = (\lambda_{cr} - \lambda_{FEM})/\lambda_{FEM}$. The error with respect to experimental result is calculated as $\text{Error}_{\text{exp}} = (\lambda_{cr} - \lambda_{exp})/\lambda_{exp}$.

Mode	Present [kN/m]	FEM [kN/m]	$\text{Error}_{\text{FEM}}$ [%] (Present)	Experimental [kN/m]	$\text{Error}_{\text{exp}}$ [%] (Present)	$\text{Error}_{\text{exp}}$ [%] (FEM)
1	43.64	43.60	0.09	39.17	11.41	11.31
2	50.77	50.72	0.10	-	-	-
3	97.74	97.54	0.21	-	-	-
4	103.18	102.95	0.22	-	-	-

In Figure 7.2, the behavior of the normalized vertical displacement can be observed, showcasing results from the implemented model, FEM, and the experimental data collected through Digital Image Correlation (DIC). As can be seen, there is an asymmetry in the experimental vertical displacement curve, which may have been caused by an imperfection in the plate, related to the panel assembly or load level imbalances.
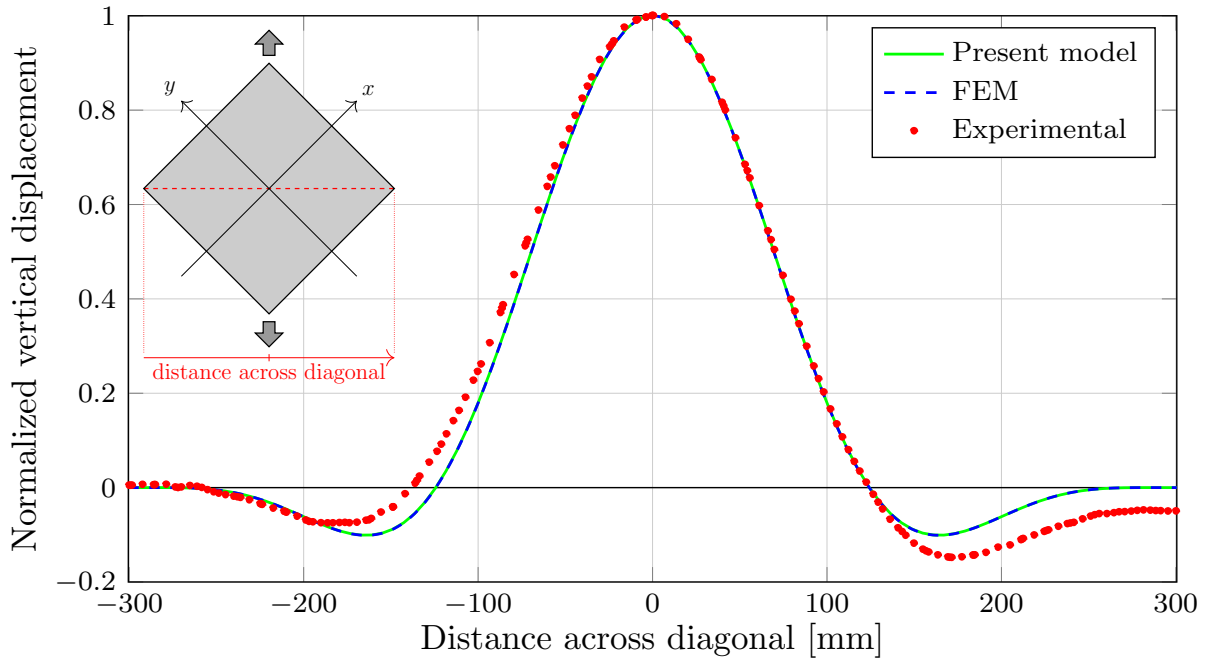
FIGURE 7.2 – Normalized vertical displacement along the diagonal of the plate.

In Figure 7.3, a graphical comparison of the modes obtained through the three adopted methodologies can be observed. The buckling mode exhibits a consistent half-wave behavior, which could already be readily evidenced through DIC.

It is noteworthy that, despite the differences in critical buckling values obtained from the experimental test compared to FEM and the implemented model, the results from

normalized vertical displacements showed good agreement. Furthermore, the DIC technique provides valuable information on critical buckling. Based on the characteristics of the vertical displacement curve, the buckling mode can be promptly estimated. Additionally, DIC offers valuable insights into the post-buckling behavior, displaying the vertical displacement behavior for various load levels, which provides richer information and, consequently, a more accurate analysis.

(a) FEM (Abaqus®).   (b) Present.   (c) Experimental test.
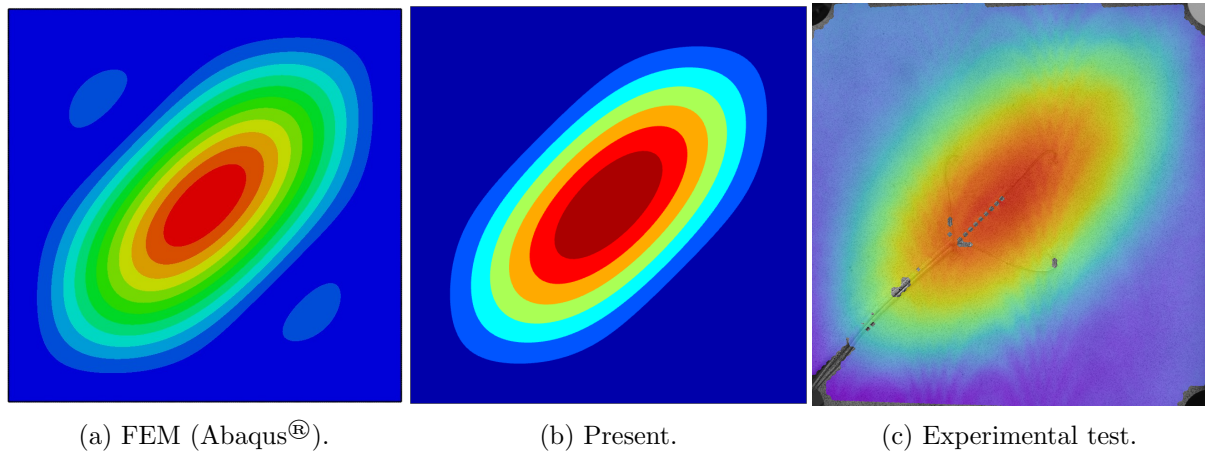
FIGURE 7.3 – Normalized absolute out-of-plane displacements, CCCC boundary condition, under pure shear loading. First mode (plate).

Furthermore, the behavior of the second, third, and fourth buckling modes are represented in Figures 7.4, 7.5, and 7.6. Once again, there was an excellent correlation in the number of half-waves between the implemented model and the FEM.

(a) FEM (Abaqus®).   (b) Present.
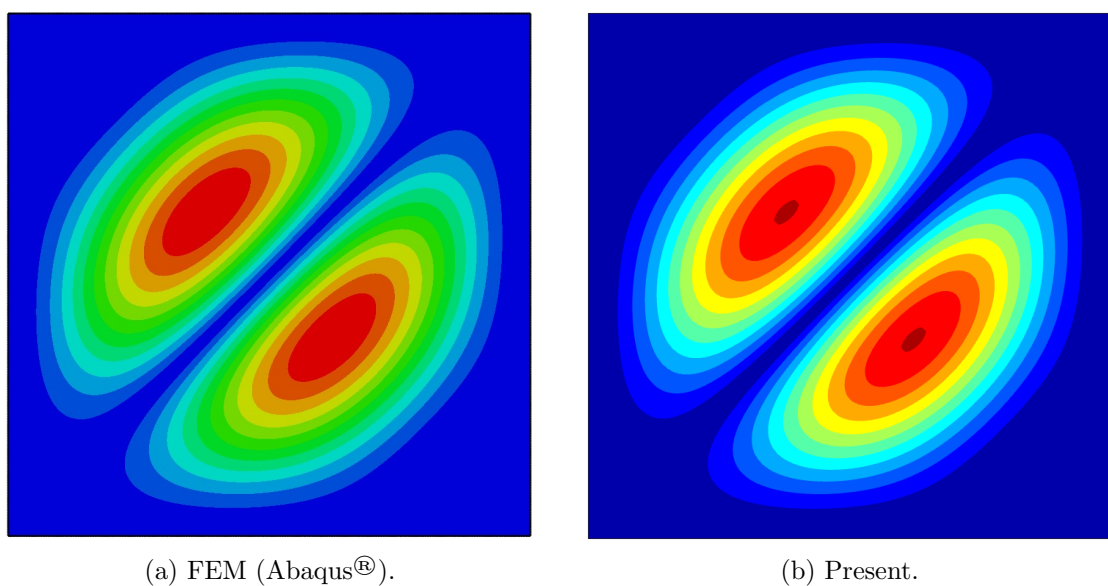
FIGURE 7.4 – Normalized absolute out-of-plane displacements, CCCC boundary condition, under pure shear loading. Second mode (plate).
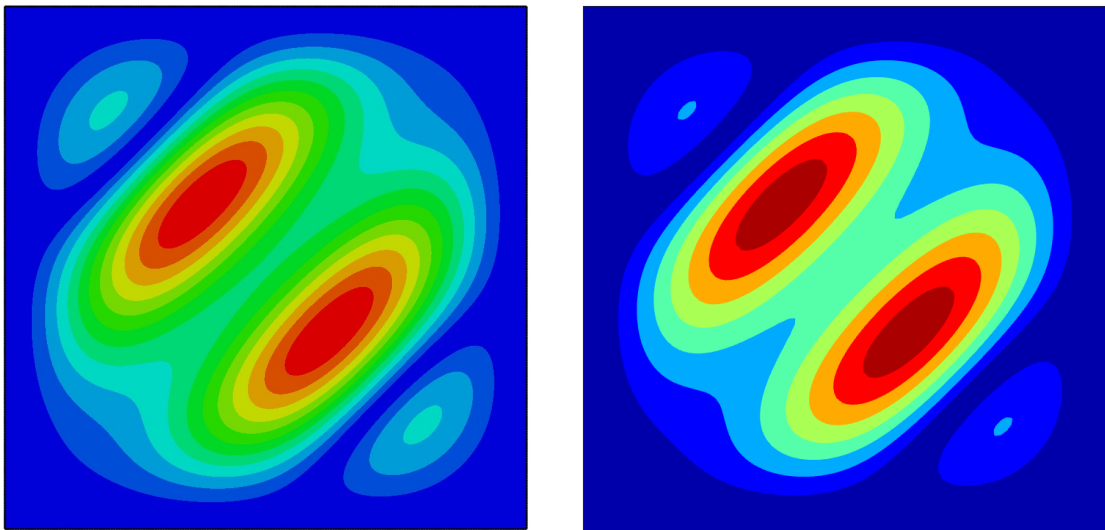
(a) FEM (Abaqus®).   (b) Present.

FIGURE 7.5 – Normalized absolute out-of-plane displacements, CCCC boundary condition, under pure shear loading. Third mode (plate).
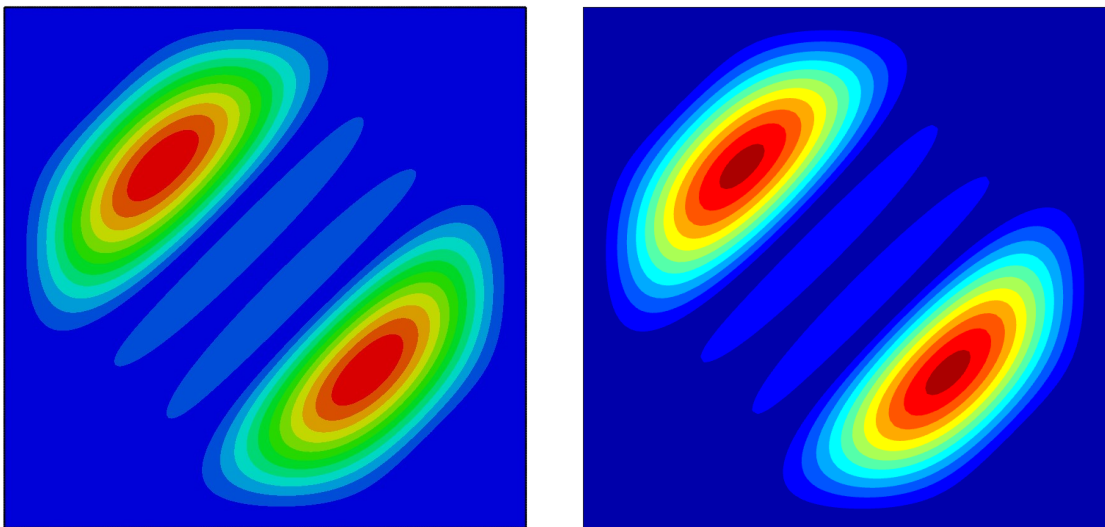
(a) FEM (Abaqus®).   (b) Present.

FIGURE 7.6 – Normalized absolute out-of-plane displacements, CCCC boundary condition, under pure shear loading. Fourth mode (plate).

7.3   Plate with a Circular Cutout

For the case of the plate with a cutout, a convergence study for the first four modes was conducted, similar to the previous case, as shown in Table 7.5 and Figure 7.7. It is noted that for $I = J = 30$, the values of the buckling modes stabilize.

TABLE 7.5 – Loads for the first four modes, in kN/m for the plate with cutout as the number of Ritz terms increases.

$I = J$	Mode 1	Mode 2	Mode 3	Mode 4
6	46.6898	106.0528	6821.4360	11852.6588
7	38.4113	56.3856	383.0877	829.9133
8	37.0016	54.4018	112.7545	139.9772
9	36.4156	53.1147	95.3524	111.5508
10	35.9249	52.6898	86.1859	105.9910
11	35.5780	52.3991	83.4217	101.3151
12	35.3314	52.1469	81.0042	98.6154
13	34.9824	51.9629	80.4121	97.7457
14	34.8133	51.8294	79.2458	97.1291
15	34.4911	51.6595	79.0291	96.8329
16	34.3674	51.5168	78.0452	96.5952
17	34.1070	51.3533	77.9274	96.4047
18	34.0095	51.1564	76.8790	96.2689
19	33.8217	50.9936	76.7825	96.1004
20	33.7408	50.7396	75.5962	96.0019
21	33.6154	50.5833	75.4939	95.8376
22	33.5443	50.2946	74.1878	95.7525
23	33.4643	50.1468	74.0703	95.5787
24	33.3990	49.8583	72.7390	95.4927
25	33.3484	49.7311	72.6133	95.3039
26	33.2837	49.4798	71.3679	95.2147
27	33.2505	49.3841	71.2493	95.0179
28	33.1814	49.1908	70.1748	94.9479
29	33.1588	49.1248	70.0809	94.7517
30	33.0880	48.9865	69.2308	94.7077
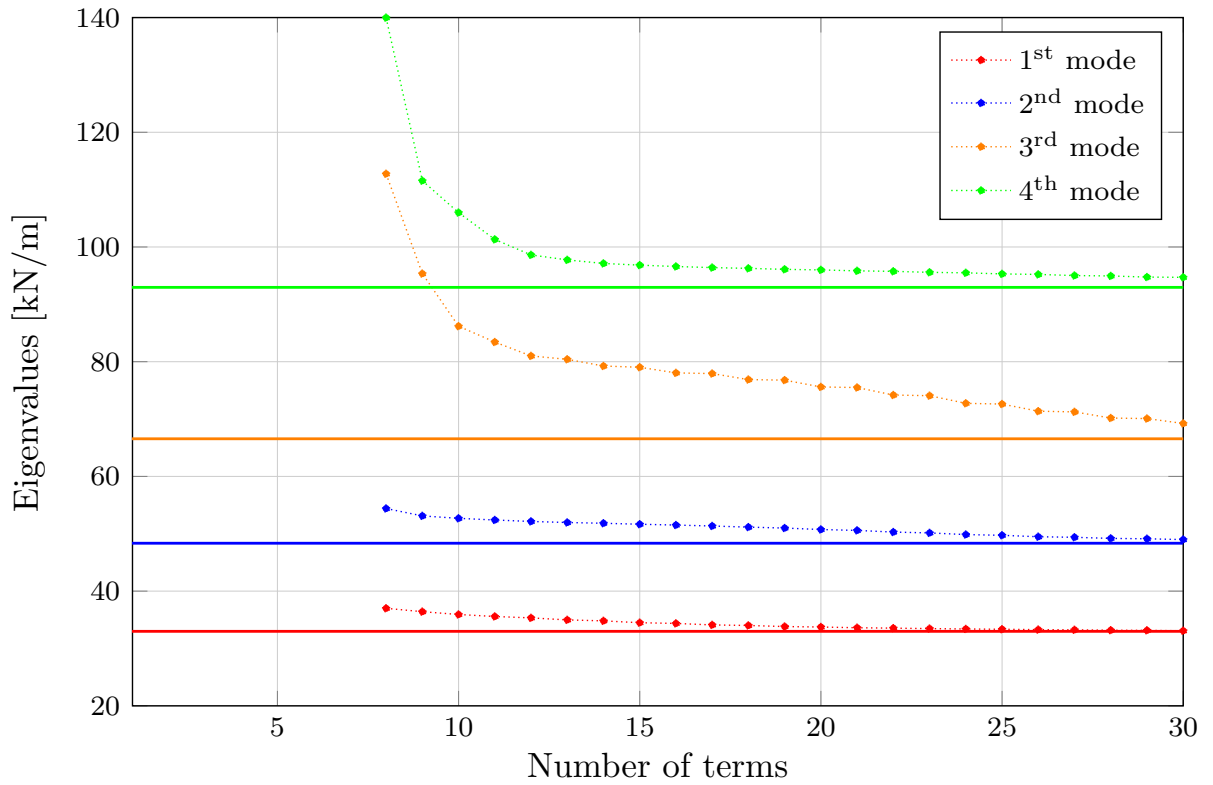
FIGURE 7.7 – Representative figure of the convergence analysis for the plate with a cutout, using the obtained finite element model values as a reference.

According to (JING; DUAN, 2023), when the cutout size is relatively small, more terms are required in the DRM to achieve convergence. Specifically, it was observed that for a cutout dimension of $R/a = 40/425 \approx 0.0941$, more terms were necessary compared to larger R/a ratios in a model containing the same stacking configuration, material properties, and type of loading. This is because a finer discretization of the plate is needed to accurately represent the cutout. Additionally, as the number of terms increases, the number of integration points required also increases. Higher mode shapes generally demand more terms for convergence due to the increased complexity of deformation. Moreover, there is a minimum number of integration points required for a given $I = J$ for the numerical integrals to converge, which in this work was found to be variable, depending on the cutout size as well as the complexity of the laminate configuration, boundary condition, and loading configuration.

Additionally, a finite element model was developed and its convergence study was conducted, as shown in Table 7.6.

TABLE 7.6 – Table containing the convergence analysis of the Finite Element Model (FEM), implemented in the Abaqus© software, showing the buckling loads for the first four modes, in kN/m, for the plate with a circular cutout configuration.

Mesh	Number of elements	Mode I	Mode II	Mode III	Mode IV
1	9265	32.94	48.50	66.45	92.76
2	15838	32.93	48.46	66.38	92.60
3	34273	32.93	48.44	66.33	92.49

Similar to the previous case involving the plate, the vertical displacements were obtained through the implemented methodology, FEM, and experimentally, as shown in Figure 7.8.
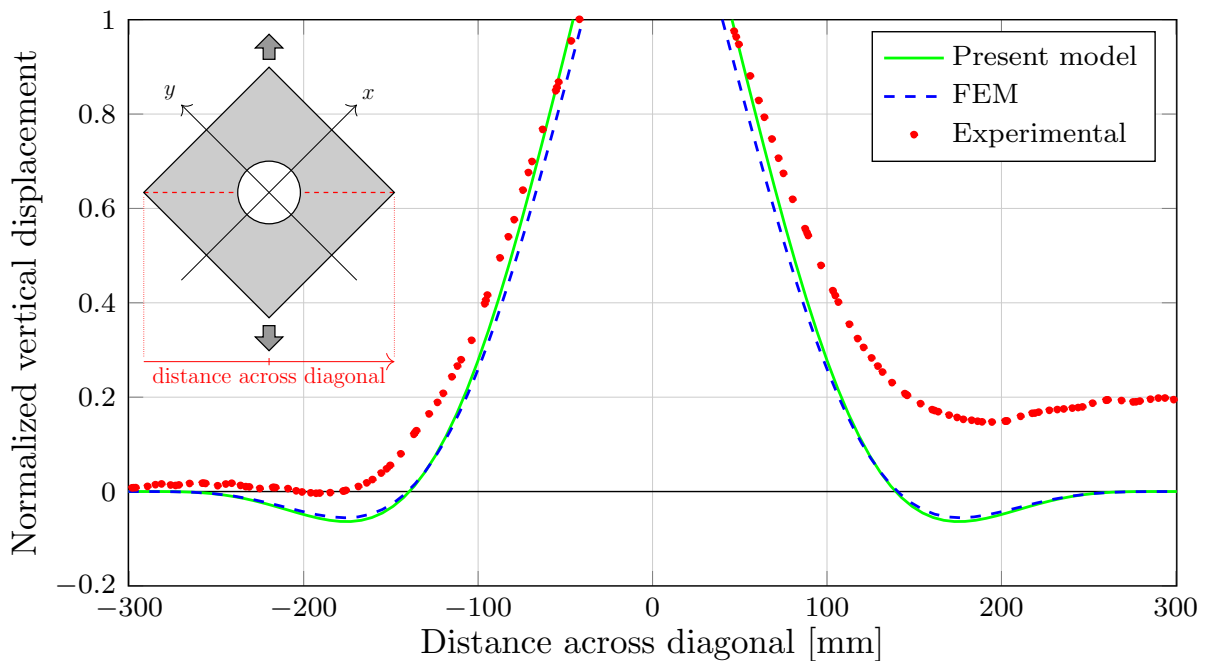
FIGURE 7.8 – Normalized vertical displacement along the diagonal of the plate with a cutout.

The obtained results are presented in Table 7.7. As shown in Table 7.7, the implemented model presented deviations ranging from 0.49% in the first mode to 4.37% in the third mode relative to the finite element model. Additionally, the adopted methodology and the FEM showed deviations of 7.23% and 6.71% relative to the experimentally obtained buckling value. There was excellent agreement between the results obtained through the implemented model and the FEM. It is worth noting that, in this case, the deviation from the experimental results was smaller than that for the plate. As can be observed, although the deviation in critical buckling between the experimental results and the others was smaller compared to the plate case, the agreement in terms of vertical displacement was not as good, yet it still showed a satisfactory correlation.

TABLE 7.7 – Results for the present model with $I = J = 30$ terms and 292×292 Gauss points, and comparisons between the implemented model, FEM and experimental test of the first four buckling modes for the plate with a circular cutout. The error with respect to FEM is calculated as $\text{Error}_{\text{FEM}} = (\lambda_{cr} - \lambda_{FEM})/\lambda_{FEM}$. The error with respect to experimental result is calculated as $\text{Error}_{\text{exp}} = (\lambda_{cr} - \lambda_{exp})/\lambda_{exp}$.

Mode	Present [kN/m]	FEM [kN/m]	Error$_{\text{FEM}}$ [%] (Present)	Experimental [kN/m]	Error$_{\text{exp}}$ [%] (Present)	Error$_{\text{exp}}$ [%] (FEM)
1	33.09	32.93	0.49	30.86	7.23	6.71
2	48.99	48.44	1.14	-	-	-
3	69.23	66.33	4.37	-	-	-
4	94.71	92.49	2.40	-	-	-

Regarding the behavior of out-of-plane displacements related to the critical buckling mode, they exhibited consistent patterns, as shown in Figure 7.9.
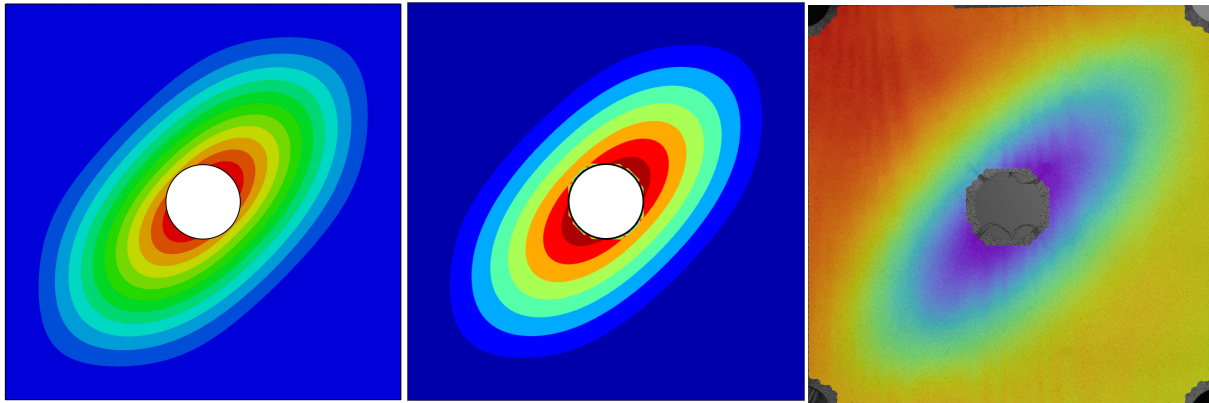
(a) FEM (Abaqus©).   (b) Present.   (c) Experimental test.

FIGURE 7.9 – Normalized absolute out-of-plane displacements, CCCC boundary condition, under pure shear loading. First mode (plate with cutout).

The behavior of the modes obtained in the second, third, and fourth modes, as well as their comparison with FEM, are represented in Figures 7.10, 7.11, and 7.12. By examining Figures 7.11 and 7.12, related to the third and fourth modes, it can be observed that these mode shapes have changed compared to the plate case. When attempting to obtain these modes without conducting a prebuckling analysis, they exhibited the same behavior as the plate but with a lower buckling load due to the presence of the cutout.
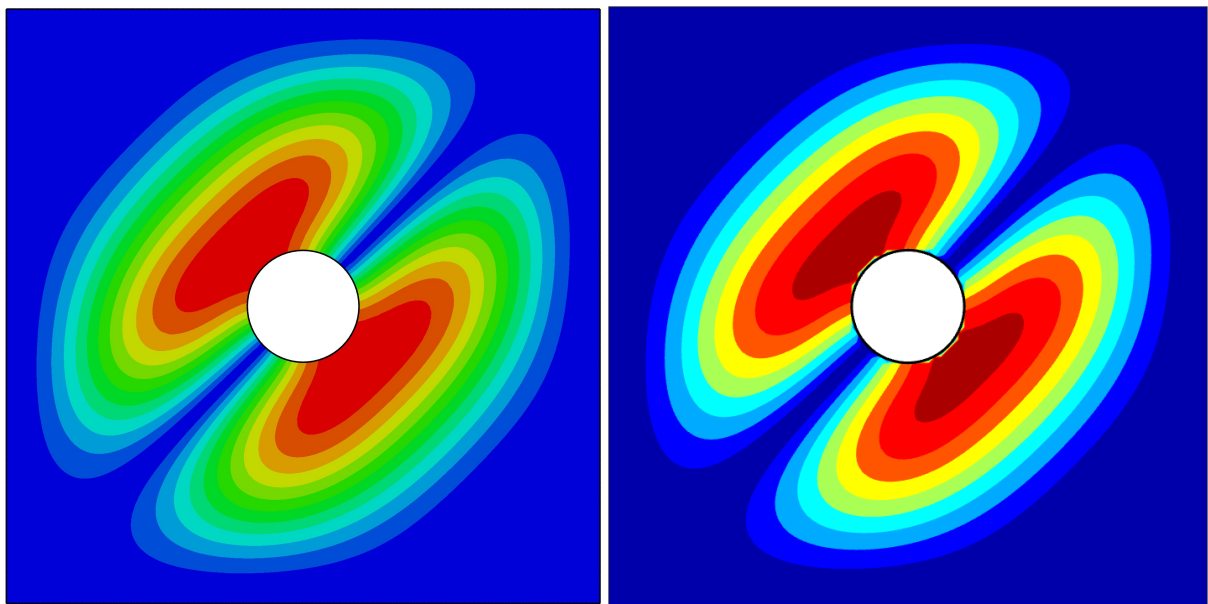
(a) FEM (Abaqus©).   (b) Present.

FIGURE 7.10 – Normalized absolute out-of-plane displacements, CCCC boundary condition, under pure shear loading. Second mode (plate with cutout).
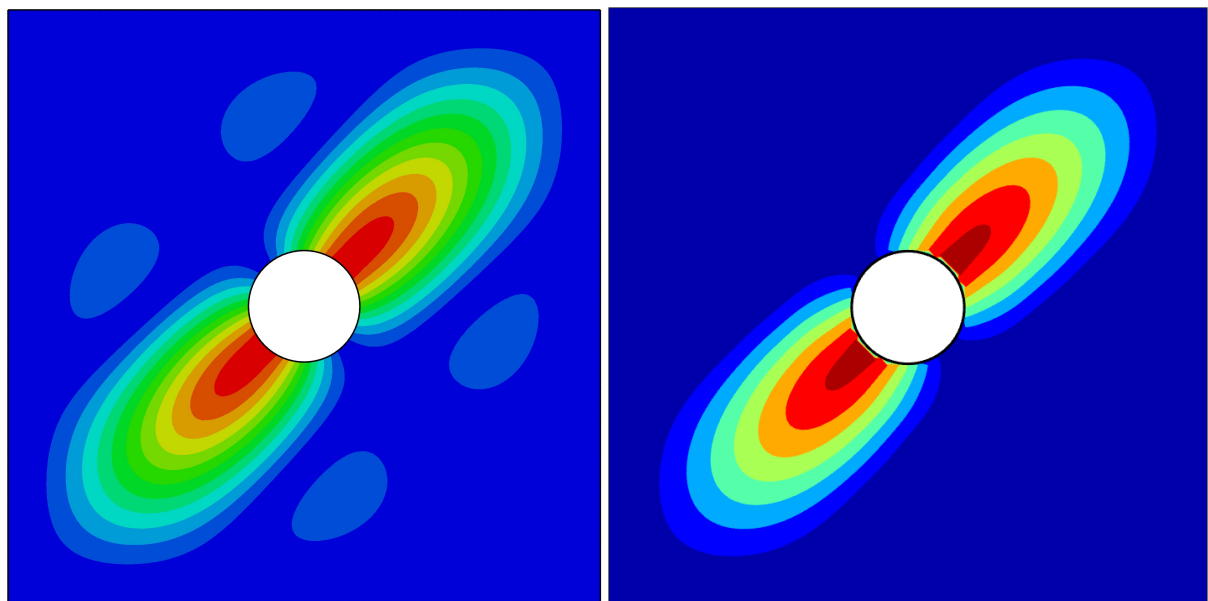
(a) FEM (Abaqus©).   (b) Present.

FIGURE 7.11 – Normalized absolute out-of-plane displacements, CCCC boundary condition, under pure shear loading. Third mode (plate with cutout).
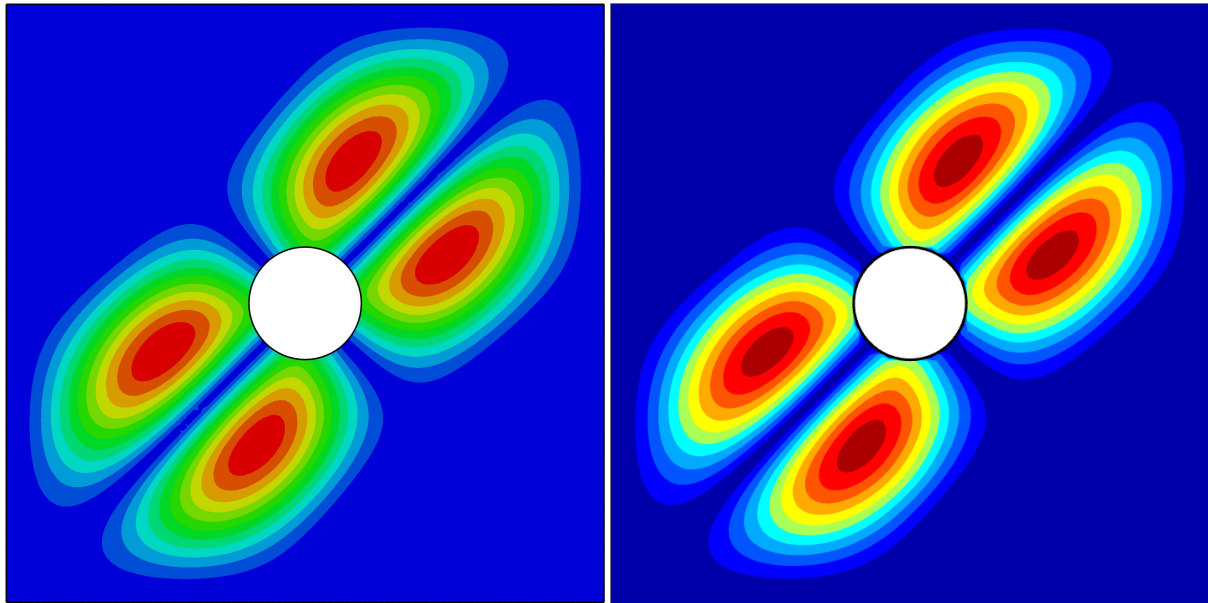
(a) FEM (Abaqus©).   (b) Present.

FIGURE 7.12 – Normalized absolute out-of-plane displacements, CCCC boundary condition, under pure shear loading. Fourth mode (plate with cutout).

7.4 Stiffened Plate with a Circular Cutout

For the case of the stiffened plate with a circular cutout, similar procedures to those used for the plate with only a circular cutout were adopted, with the addition of two longitudinal stiffeners along the plate. This increased the complexity of the finite element analysis, as it became necessary to simulate the interaction between the stiffeners and the plate. A convergence study for the first four modes was carried out, similar to the previous case, as shown in Tab. 7.8 and Fig. 7.13. It was noted that for $I = J = 30$, the values of the buckling modes stabilized.

TABLE 7.8 – Loads for the first four modes, in kN/m for the stiffened plate with cutout as the number of Ritz terms increases.

$I = J$	Mode 1	Mode 2	Mode 3	Mode 4
6	334.5657	502.6223	7425.0018	12273.7496
7	125.0830	145.0477	996.3069	1359.6358
8	54.3636	107.7544	176.2125	242.0077
9	50.6923	98.7794	139.9283	167.8439
10	47.3402	88.4539	115.4712	135.1420
11	45.6413	79.9930	111.4413	124.8801
12	43.4741	77.5296	105.6246	120.4318

$I = J$	Mode 1	Mode 2	Mode 3	Mode 4
13	42.8123	74.1909	103.3334	117.1432
14	41.1928	73.1298	101.4650	115.4011
15	40.8470	72.5480	100.4920	114.2794
16	40.3137	71.7715	98.4882	112.8654
17	39.8435	70.1833	97.8513	112.1248
18	39.7155	69.8126	95.9637	111.7363
19	39.3505	68.5031	95.1711	111.2681
20	38.9049	67.9418	93.6511	110.7055
21	38.7235	67.6401	93.1413	110.4762
22	38.2651	66.8823	91.7154	109.5445
23	38.1102	66.5196	91.3728	109.3229
24	37.9272	65.8400	89.9742	108.6488
25	37.7681	65.0747	89.4125	108.4313
26	37.6540	64.5322	87.9512	107.9405
27	37.5594	63.9850	87.4018	107.7663
28	37.3158	63.5545	85.9711	107.0987
29	37.2790	63.4249	85.7169	106.9228
30	37.0583	63.1056	84.6254	106.2876
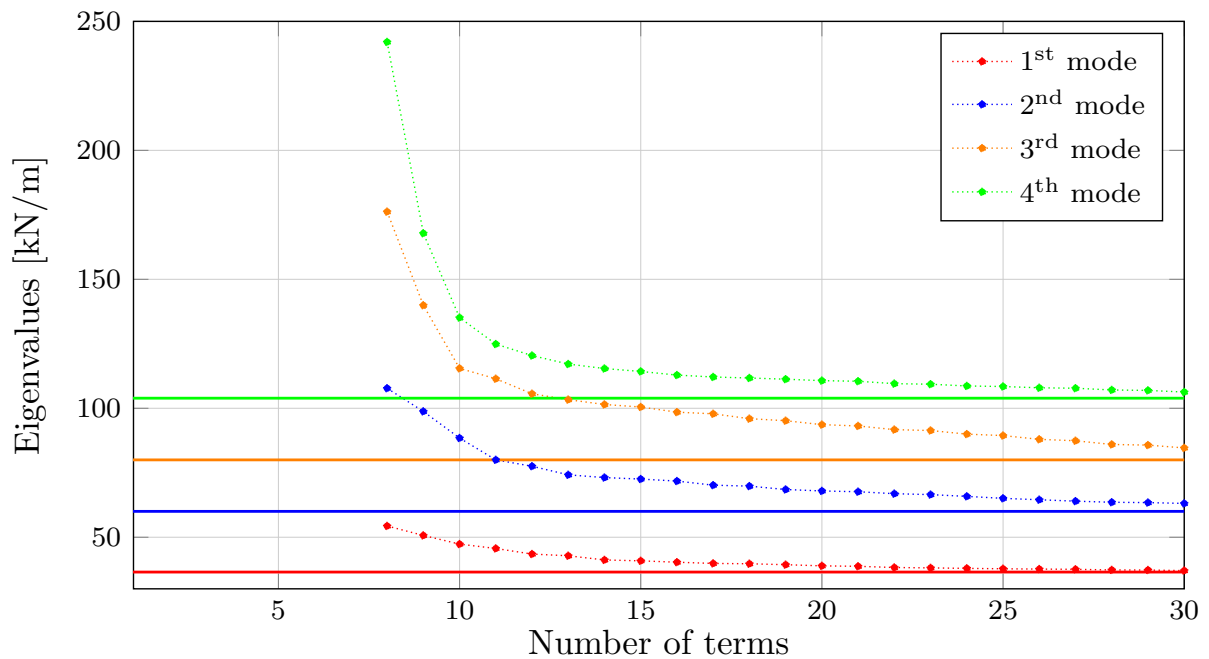
FIGURE 7.13 – Representative figure of the error analysis for the stiffened plate with cutout, using the obtained finite element model values as a reference.

As previously mentioned, more elements were required in this case compared to the

previous ones in the FEM, resulting in the use of 94,391 elements. The FEM results can
be seen in Table 7.9.

TABLE 7.9 – Table containing the convergence analysis of the Finite Element Model (FEM), implemented
in the Abaqus© software, showing the buckling loads for the first four modes, in kN/m, for the stiffened
plate with a circular cutout.

Mesh	Number of elements	Mode I	Mode II	Mode III	Mode IV
1	13039	36.61	60.30	80.46	104.39
2	23311	36.56	60.17	80.25	104.16
3	52733	36.52	60.08	80.07	103.98
4	94391	36.50	60.03	79.99	103.91

The behavior of the vertical displacement using three methodologies is illustrated in
Figure 7.14. The DIC results showed consistency with the other methodologies, despite
some deviations. These deviations may be attributed to experimental conditions, such
as variations in manufacturing, including temperature and pressure during fabrication,
which result in different microstructures of the composite material. Additionally, the
torque applied to the bolts could cause discrepancies in the theoretical model of the
clamped boundary condition.
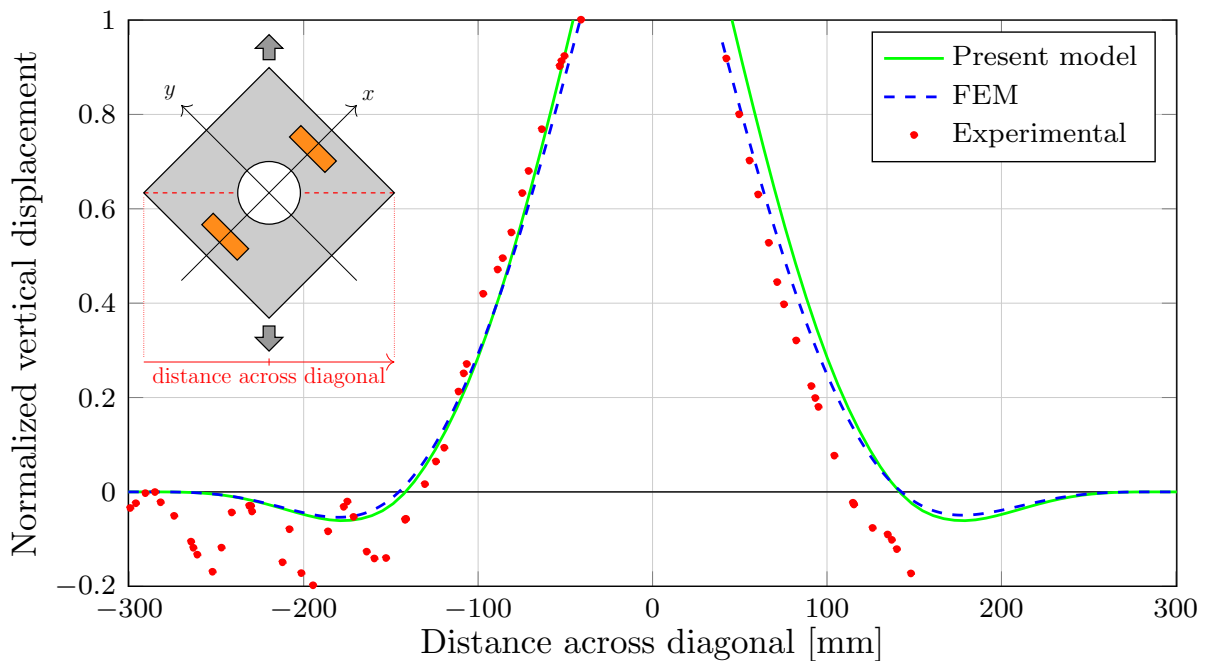
FIGURE 7.14 – Normalized vertical displacement along the diagonal of the stiffened plate with cutout.

Additionally, the final results were compared between the values obtained from the
implemented model, FEM, and the experiment, as shown in Table 7.10. As can be seen in
Table 7.10, the implemented model presented an error of 1.53% for the first mode and up

to 5.80% for the third mode relative to the FEM. Furthermore, the experimental results showed excellent correlation with the implemented model and FEM, with errors of 1.62% and 3.11%, respectively.

TABLE 7.10 – Results for the present model with $I = J = 30$ terms and 292×292 Gauss points, and comparisons between the implemented model, FEM and experimental test of the first four buckling modes for the stiffened plate with circular cutout. The error with respect to FEM is calculated as $\text{Error}_{\text{FEM}} = (\lambda_{cr} - \lambda_{FEM})/\lambda_{FEM}$. The error with respect to experimental result is calculated as $\text{Error}_{\text{exp}} = (\lambda_{cr} - \lambda_{exp})/\lambda_{exp}$.

Mode	Present [kN/m]	FEM [kN/m]	$\text{Error}_{\text{FEM}}$ [%] (Present)	Experimental [kN/m]	$\text{Error}_{\text{exp}}$ [%] (Present)	$\text{Error}_{\text{exp}}$ [%] (FEM)
1	37.06	36.50	1.53	37.67	-1.62	-3.11
2	63.11	60.03	5.13	-	-	-
3	84.63	79.99	5.80	-	-	-
4	106.29	103.91	2.29	-	-	-

Moreover, as can be seen in Figure 7.15, consistent out-of-plane displacements behavior was obtained between the FEM, the implemented model, as well as the experimental results, demonstrating the reliability of the proposed model.

(a) FEM (Abaqus©).   (b) Present.   (c) Experimental test.

FIGURE 7.15 – Normalized absolute out-of-plane displacements, CCCC boundary condition, under pure shear loading. First mode (stiffened plate with cutout).

By examining Figures 7.16, 7.17, and 7.18, related to the second, third, and fourth buckling modes, respectively, it can be observed that these modes were more influenced by the presence of the stiffeners compared to the case of the plate with a circular cutout. In the second and third modes, the inclusion of the stiffeners resulted in more sinuous shapes. The fourth mode, however, exhibited a more significant change compared to the others. It is also worth noting that, despite the complexity of the fourth mode's behavior, the

adopted semi-analytical model produced results consistent with those simulated through FEM.

(a) FEM (Abaqus©).   (b) Present.

FIGURE 7.16 – Normalized absolute out-of-plane displacements, CCCC boundary condition, under pure shear loading. Second mode (stiffened plate with cutout).

(a) FEM (Abaqus©).   (b) Present.

FIGURE 7.17 – Normalized absolute out-of-plane displacements, CCCC boundary condition, under pure shear loading. Third mode (stiffened plate with cutout).

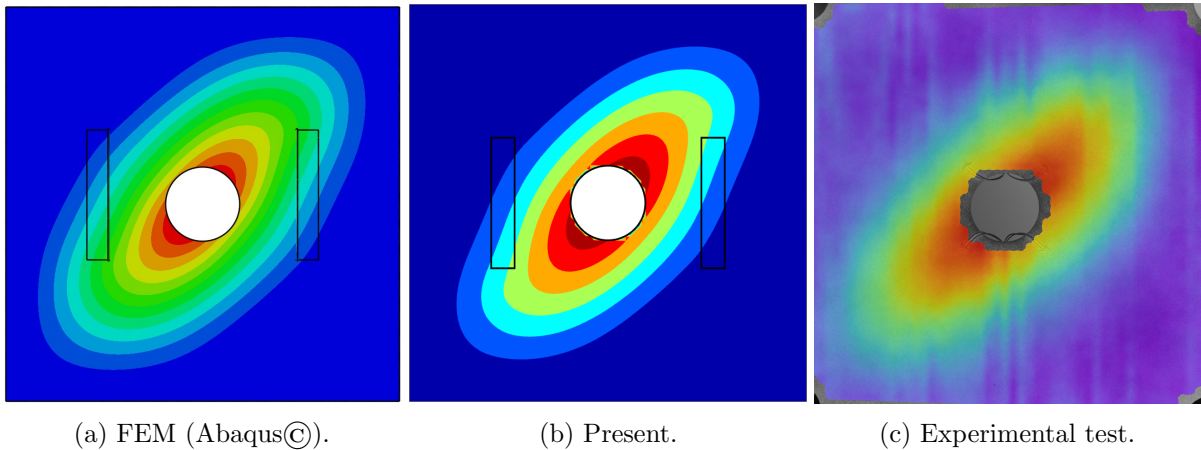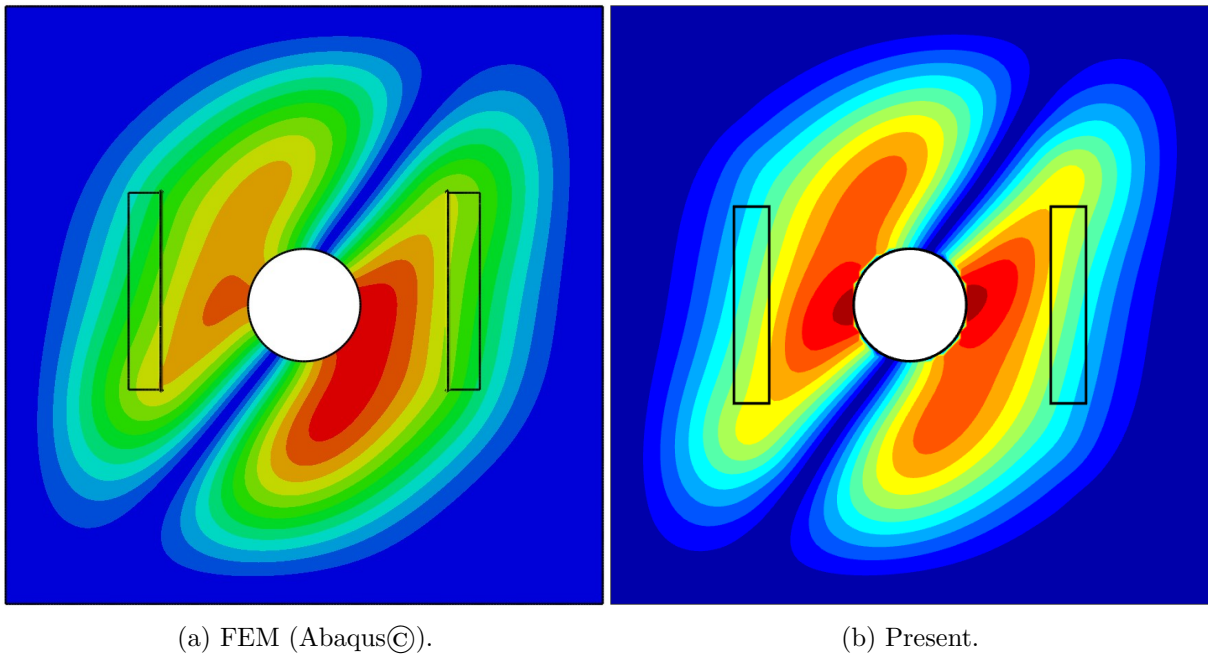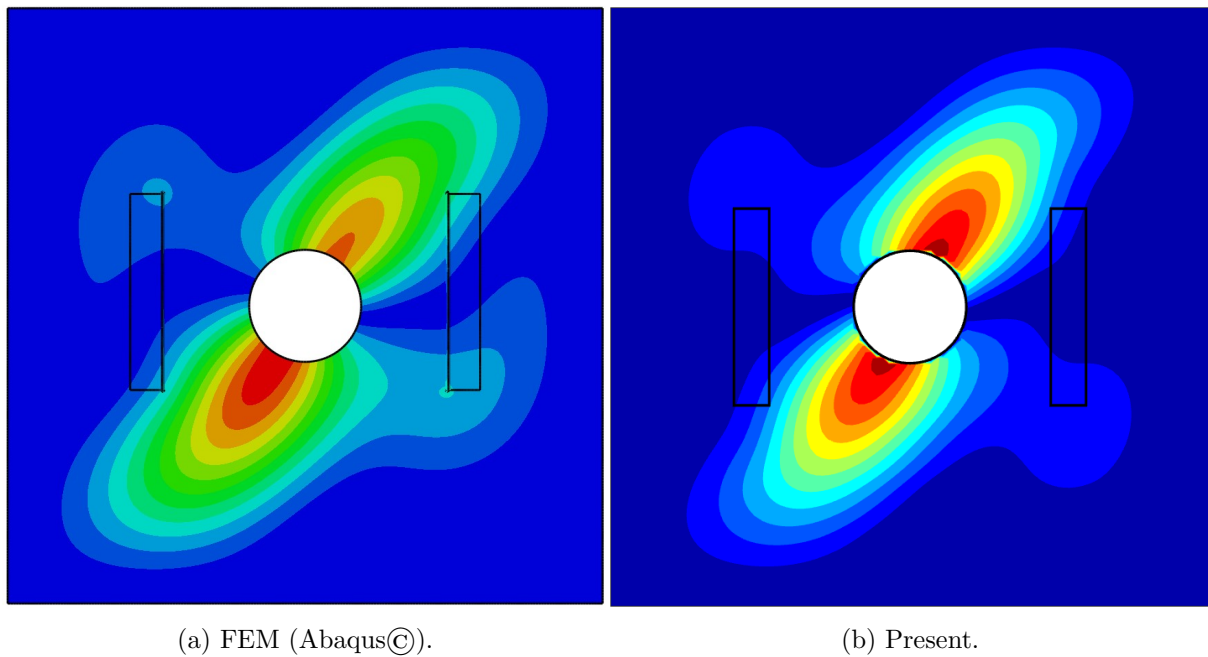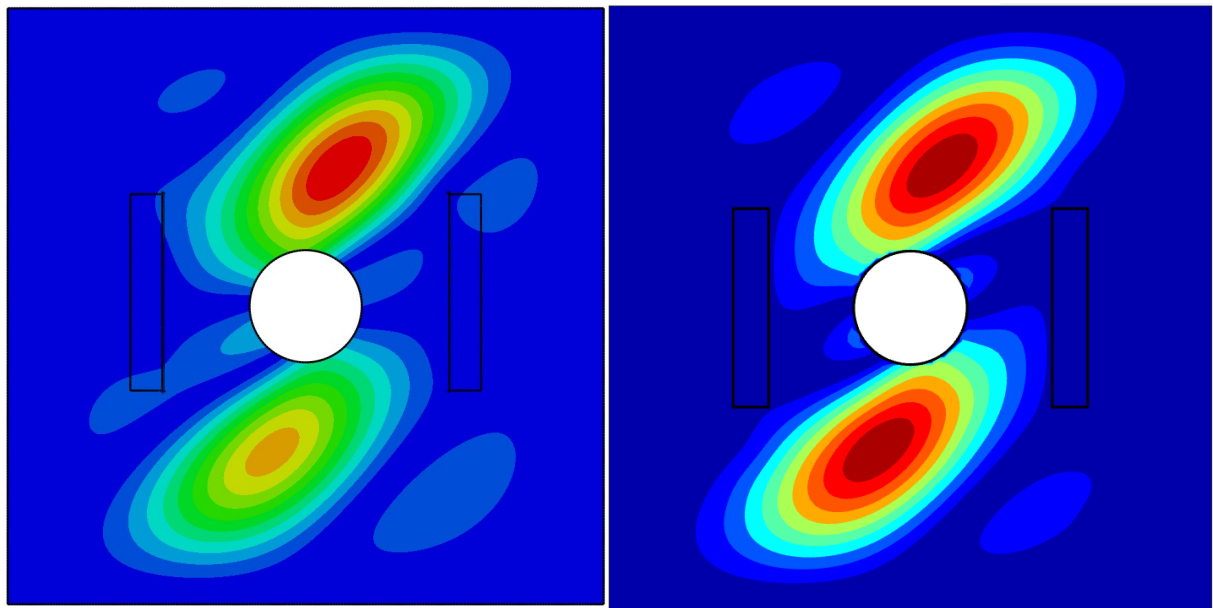(a) FEM (Abaqus©).   (b) Present.

FIGURE 7.18 – Normalized absolute out-of-plane displacements, CCCC boundary condition, under pure shear loading. Fourth mode (stiffened plate with cutout).

8 Conclusions

Throughout this theoretical and experimental research, the following key conclusions were drawn:

A semi-analytical model was developed using the Discrete Ritz Method (DRM) and the principle of stationary total potential energy to analyze the prebuckling behavior and determine the critical buckling load of plates with circular cutouts and stiffeners under various loading conditions. The research effectively implemented the DRM along with hierarchical polynomials as trial shape functions.

The semi-analytical model was rigorously verified against existing literature and finite element analysis (FEA). The results for the plates exhibited a deviation ranging from 0.15% to 0.23% in relation to FEM, in addition to presenting results consistent with those predicted in (NARITA, 1990). For the case of plates with cutouts, the model showed an error of 0.045% to 0.362% in relation to FEM, and also consistent results with those predicted in the literature in (NIMA; GANESAN, 2021) and (JING; DUAN, 2023).

The developed method demonstrated superior computational efficiency compared to traditional approaches. The utilization of hierarchical polynomials and numerical integration via Gauss-Legendre quadrature significantly reduced the computational time and effort required. Specifically, the methodology maximized the use of limited computational resources by allowing the calculation of critical buckling for lower indices of hierarchical polynomials with the same number of integration points, eliminating the need for additional sets of integration. This approach not only enhanced computational efficiency but also facilitated a reliable convergence study by verifying the convergence trend.

An improvement on the simulation performance was developed to minimize the number of simulations required for various edge boundary conditions. This improvement on the simulation performance resulted in reduced computational effort while maintaining high accuracy in the buckling load predictions. Similarly, by reducing the necessary sets of integration for lower indices of hierarchical polynomials, this methodology allows for the execution of $3^4 - 1$ simulations with various boundary conditions using only a single set of integration for a given loading mode. Furthermore, considering that initially all the first four hierarchical polynomials are always integrated, an additional improvement was

performed by verifying the symmetry of certain matrices derived from the multiplication of partial derivatives in both the prebuckling and buckling analyses, resulting in faster simulations.

Experimental tests were conducted involving three idealized configurations of a typical horizontal stabilizer rib: in the case considering only the plate, the semi-analytical model presented an error of 0.09% in relation to FEM, as well as an error of 11.41% in relation to the experimentally obtained value. In the case of the plate with a circular cutout, an error of 0.49% was obtained in relation to FEM, as well as 7.23% in relation to the experimental result. Finally, considering a stiffened plate with a cutout, an error of 1.53% was obtained in relation to FEM and 1.62% in relation to the experimental result.

The differences between the experimental and numerical results obtained using the proposed semi-analytical model could be attributed to limitations in the semi-analytical model, as well as variations in the experimental setup, such as the modeling of clamping conditions, since the torque applied to the bolts may cause differences. Additionally, these discrepancies may be related to manufacturing differences, including temperature and pressure conditions during fabrication, and possible geometric imperfections of the plates.

The semi-analytical model successfully identified the change in behavior of the out-of-plane displacements in the third and fourth modes with the inclusion of the cutout, as well as the interaction between the cutout and the stiffener, exhibiting behavior similar to that predicted by FEM.

Ultimately, both experimentally and numerically, the stiffened plate with a cutout presented a lower critical buckling load compared to the plate. The plate exhibited a critical buckling load of 43.64 kN/m (implemented model) and 39.17 kN/m (experimentally), while the stiffened panel showed a critical buckling load of 37.06 kN/m (implemented model) and 37.67 kN/m (experimentally). This indicates that the stiffeners were not sufficient to compensate for the inclusion of the cutout and maintain the same critical buckling load.

8.1   Future Works

Building upon the findings of this research, several areas warrant further investigation to enhance the semi-analytical model and expand its applicability:

First, it is crucial to investigate the model's performance under more complex loading scenarios, such as combined shear and compression, cyclic loading, and dynamic loading conditions. This will help assess the robustness of the model in real-world applications.

Second, expanding the study to include various cutout shapes (e.g., elliptical, square) and different stiffener configurations is necessary. This would demonstrate the model's versatility and provide insights into optimal design strategies for different applications.

Third, integrating the effects of temperature changes and environmental conditions (e.g., humidity, corrosion) on the buckling behavior is particularly relevant for aerospace and marine applications where such factors are critical.

Fourth, exploring the integration of machine learning algorithms to predict buckling loads and optimize design parameters could enhance the model's predictive capabilities and streamline the design process.

Fifth, conducting extensive experimental validation using a wider range of materials, including advanced composites and smart materials, will help verify the model's accuracy and adaptability across different material systems.

Sixth, integrating optimization algorithms to identify the most effective stiffener configurations and cutout shapes that maximize buckling resistance while minimizing weight and material usage is essential.

Finally, investigating the model's sensitivity to manufacturing imperfections such as misalignments, residual stresses, and material defects will enhance its reliability for practical engineering applications.

Addressing these areas will significantly contribute to the advancement of semi-analytical modeling techniques and their application in engineering practice, ensuring more robust and versatile solutions for future challenges.

Bibliography

ABOLGHASEMI, S.; EIPAKCHI, H.; SHARIATI, M. An analytical solution for buckling of plates with circular cutout subjected to non-uniform in-plane loading. **Archive of Applied Mechanics**, v. 89, 12 2019.

BARDELL, N. Free vibration analysis of a flat plate using the hierarchical finite element method. **Journal of Sound and Vibration**, v. 151, n. 2, p. 263–289, 1991. ISSN 0022-460X. Available at: https://www.sciencedirect.com/science/article/pii/0022460X9190855E.

BESLIN, O.; NICOLAS, J. A hierarchical functions set for predicting very high order plate bending modes with any boundary conditions. **Journal of Sound and Vibration**, v. 202, n. 5, p. 633–655, 1997. ISSN 0022-460X. Available at: https://www.sciencedirect.com/science/article/pii/S0022460X9690797X.

CASTRO, S. G.; DONADON, M. V. Assembly of semi-analytical models to address linear buckling and vibration of stiffened composite panels with debonding defect. **Composite Structures**, v. 160, p. 232–247, 2017. ISSN 0263-8223. Available at: https://www.sciencedirect.com/science/article/pii/S026382231631008X.

CHO, D. S.; VLADIMIR, N.; CHOI, T. M. Numerical procedure for the vibration analysis of arbitrarily constrained stiffened panels with openings. **International Journal of Naval Architecture and Ocean Engineering**, v. 6, n. 4, p. 763–774, 2014. ISSN 2092-6782. Available at: https://www.sciencedirect.com/science/article/pii/S2092678216302527.

CISC. **Torsional Section Properties of steel shapes**. Canadian Institute of Steel Construction, 2002. Available at: http://www.labciv.eng.uerj.br/pgeciv/files/Torsion%20Properties-.pdfhttp://www.labciv.eng.uerj.br/pgeciv/files/Torsion%20Properties.pdf.

CSA. **Limit States Design of Steel Structures. CSA Standard S16.1-94**. Rexdale, Ont.: Standards Association, 1994.

DARVIZEH, M.; DARVIZEH, A.; ANSARI, R.; SHARMA, C. Buckling analysis of generally laminated composite plates (generalized differential quadrature rules versus Rayleigh–Ritz method). **Composite Structures**, v. 63, n. 1, p. 69–74, 2004. ISSN 0263-8223. Available at: https://www.sciencedirect.com/science/article/pii/S0263822303001338.

DEHGHANI, M. Finite plate with circular and square hole under partial loading.
International Journal of Engineering, Transactions A: Basics, v. 31, p. 1109–1116, 07
2018.

DHURIA, M.; GROVER, N.; GOYAL, K. Review of solution methodologies for
structural analysis of composites. **European Journal of Mechanics - A/Solids**, v. 103,
2024. ISSN 0997-7538. Available at:
https://www.sciencedirect.com/science/article/pii/S0997753823002498.

GHANNADPOUR, S.; MEHRPARVAR, M. Energy effect removal technique to model
circular/elliptical holes in relatively thick composite plates under in-plane compressive
load. **Composite Structures**, v. 202, p. 1032–1041, 2018. ISSN 0263-8223. Available at:
https://www.sciencedirect.com/science/article/pii/S0263822318302253.

HALEY, S. **Design Optimization and Verification of a Horizontal Stabilizer for the
SeaStryder600 Wing-in-ground-Effect (WIG) Aircraft**. 109 p. Dissertation (Mestrado)
— University of Toronto, Canada, 2012.

HUANG, C.; LEISSA, A.; LI, R. Accurate vibration analysis of thick, cracked
rectangular plates. **Journal of Sound and Vibration**, v. 330, n. 9, p. 2079–2093, 2011.
ISSN 0022-460X. Available at:
https://www.sciencedirect.com/science/article/pii/S0022460X10007522.

JANSSENS, T. A. **Semi-Analytical Modelling of VAT Laminates with Cut-Outs**. 115 p.
Dissertation (Mestrado) — Delft University of Technology, The Netherlands, 2020.

JING, Z.; DUAN, L. Discrete Ritz method for buckling analysis of arbitrarily shaped
plates with arbitrary cutouts. **Thin-Walled Structures**, v. 193, 2023. ISSN 0263-8231.
Available at: https://www.sciencedirect.com/science/article/pii/S0263823123007723.

JONES, R. **Mechanics Of Composite Materials**. Taylor & Francis, 1998. (500 Tips).
ISBN 9781560327127. Available at:
https://books.google.com.br/books?id=oMph2kNG3yAC.

KASSAPOGLOU, C. Composite plates with two concentric layups under compression.
Composites Part A: Applied Science and Manufacturing, v. 39, n. 1, p. 104–112, 2008.
ISSN 1359-835X. Available at:
https://www.sciencedirect.com/science/article/pii/S1359835X07001650.

KUKRETI, A.; CHERAGHI, E. Analysis procedure for stiffened plate systems using an
energy approach. **Computers Structures**, v. 46, n. 4, p. 649–657, 1993. ISSN 0045-7949.
Available at: https://www.sciencedirect.com/science/article/pii/004579499390393R.

KUMAR, Y. V. S. The Rayleigh–Ritz method for linear dynamic, static and buckling
behavior of beams, shells and plates: A literature review. **Journal of Vibration and
Control**, v. 24, p. 1205 – 1227, 2018. Available at:
https://api.semanticscholar.org/CorpusID:126101341.

LEVY NETO, F.; PARDINI, L. **Compósitos estruturais: ciência e tecnologia**. 2. ed.
Editora Blucher, 2018. 418 p. ISBN 9788521210795. Available at:
https://books.google.com.br/books?id=DS1dDwAAQBAJ.

LUCENA NETO, E. **Fundamentos da mecânica das estruturas**. Florianópolis, SC: Orsa Maggiore, 2021. 523 p. ISBN 978-65-993681-2-7.

MORENO-GARCÍA, P.; SANTOS, J. V. D.; LOPES, H. A review and study on Ritz method admissible functions with emphasis on buckling and free vibration of isotropic and anisotropic beams and plates. **Archives of Computational Methods in Engineering**, v. 25, 03 2017.

NARITA, A. W. L. Y. Buckling studies for simply supported symmetrically laminated rectangular plates. **International Journal of Mechanical Sciences**, v. 32, n. 11, p. 909–924, 1990.

NI, Q.-Q.; XIE, J.; IWAMOTO, M. Buckling analysis of laminated composite plates with arbitrary edge supports. **Composite Structures**, v. 69, n. 2, p. 209–217, 2005. ISSN 0263-8223. Available at: https://www.sciencedirect.com/science/article/pii/S026382230400220X.

NIMA, S. J.; GANESAN, R. Buckling analysis of symmetrically laminated composite plates including the effect of variable pre-stress field using the Ritz method. **European Journal of Mechanics - A/Solids**, v. 90, 2021. ISSN 0997-7538. Available at: https://www.sciencedirect.com/science/article/pii/S0997753821000954.

REDDY, J. N. **Mechanics of Laminated Composite Plates and Shells: Theory and Analysis**. 2. ed. CRC Press, 2003. (Applied and Computational Mechanics). ISBN 9780203502808. Available at: https://books.google.com.br/books?id=eeUr_AJiGRcC.

SHOJAEE, T.; MOHAMMADI, B.; MADOLIAT, R. Experimental and numerical investigation of stiffener effects on buckling strength of composite laminates with circular cutout. **Journal of Composite Materials**, v. 54, 09 2019.

SILVA, D. **A semi-analytical model for shear buckling analysis of stiffened composite panel with debonding defect**. 97 p. Dissertation (Mestrado) — Instituto Tecnológico de Aeronáutica, São José dos Campos, 2021.

SINGER, J.; ARBOCZ, J.; WELLER, T. **Buckling Experiments: Experimental Methods in Buckling of Thin-Walled Structures, Volume 1: Basic Concepts, Columns, Beams and Plates**. Wiley, 1998. (Buckling Experiments). ISBN 9780471956617. Available at: https://books.google.com.br/books?id=JcoaNP24bP8C.

STAMATELOS, D.; LABEAS, G.; TSERPES, K. Analytical calculation of local buckling and post-buckling behavior of isotropic and orthotropic stiffened panels. **Thin-Walled Structures**, v. 49, n. 3, p. 422–430, 2011. ISSN 0263-8231. Available at: https://www.sciencedirect.com/science/article/pii/S0263823110002107.

STAMATELOS, D. G.; LABEAS, G. N. Buckling analysis of laminated stiffened plates with material anisotropy using the Rayleigh–Ritz approach. **Computation**, v. 11, n. 6, 2023. ISSN 2079-3197. Available at: https://www.mdpi.com/2079-3197/11/6/110.

WANG, Y.; QIAO, P. Improved buckling analysis of stiffened laminated composite plates by spline finite strip method. **Composite Structures**, v. 255, 2021. ISSN 0263-8223. Available at: https://www.sciencedirect.com/science/article/pii/S0263822320328622.

YOO, C.; LEE, S. **Stability of Structures: Principles and Applications**. Elsevier
Science, 2011. ISBN 9780123851239. Available at:
https://books.google.com.br/books?id=z63LseRitIcC.

YSHII, L. N.; NETO, E. L.; MONTEIRO, F. A. C.; SANTANA, R. C. Accuracy of the
buckling predictions of anisotropic plates. **Journal of Engineering Mechanics**, v. 144, n.
Issue 8, 2018. Available at:
https://ascelibrary.org/doi/abs/10.1061/%28ASCE%29EM.1943-7889.0001498.

ZHANG, C.; BAI, R.; LEI, Z.; SUN, Z.; SU, K. Buckling analysis of composite
laminates with a circular hole. **Journal of Physics: Conference Series**, v. 1699, 11 2020.

ZWEBEN, C.; BEAUMONT, P. **Comprehensive Composite Materials II**. Elsevier
Science, 2017. ISBN 9780081005347. Available at:
https://books.google.com.br/books?id=fxR2DQAAQBAJ.

Appendix A - Stiffeners' parameters

A.1 Calculating the Stiffeners' Parameters

In this section, the methodology employed to determine the associated energies related to a stiffener will be presented, including the calculation of its geometric and stiffness parameters. Figure A.1 provides an xz view of the setup, depicting the stiffeners' dimensions and the total thickness of the plate. For clarity, these dimensions are exaggerated compared to those in the actual tested scenario.
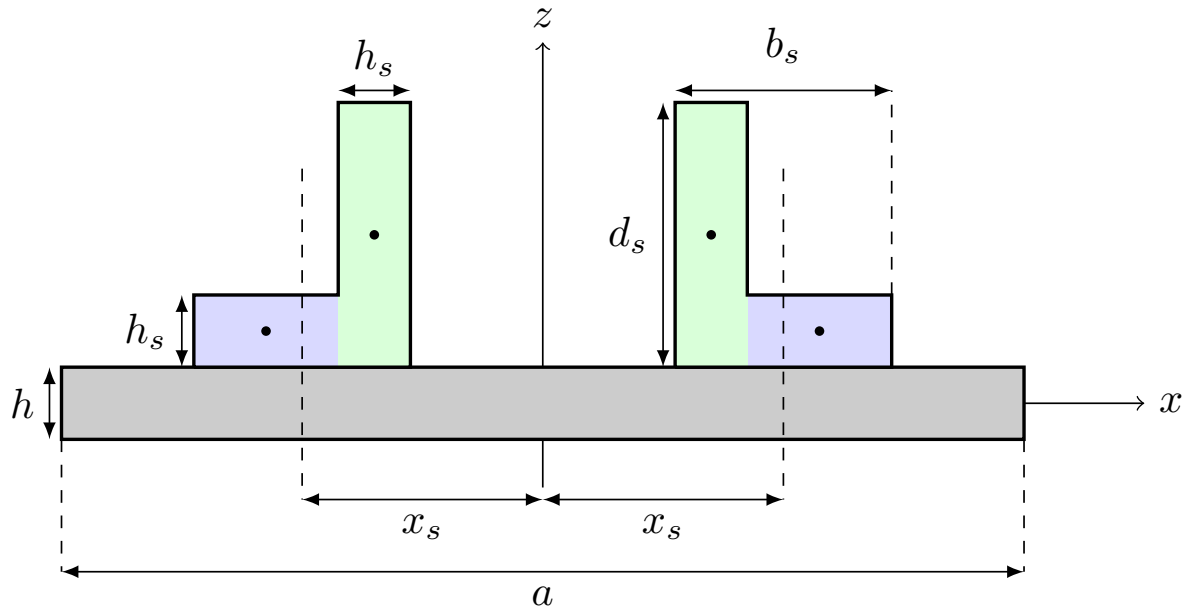
FIGURE A.1 – Representative figure of the geometric parameters related to the stiffeners in the implemented model.

The stiffeners feature an L-shaped cross-section with area $A_{st} = d_s h_s + b_s h_s - h_s^2$, which can be divided into two rectangles: one with dimensions $(b_s - h_s) \times h_s$, shown in blue in Figure A.1, and another with dimensions $h_s \times d_s$, shown in green in Figure A.1. Each area has a black dot indicating its centroid.

The moments of inertia of each area with respect to the laminate's mid-plane are calculated as follows:

$$I_{xx}^{\text{blue}} = \frac{h_s^3(b_s - h_s)}{12} + h_s(b_s - h_s)\left(\frac{h_s}{2} + \frac{h}{2}\right)^2 \tag{A.1}$$

$$I_{xx}^{\text{green}} = \frac{h_s d_s^3}{12} + h_s d_s \left(\frac{d_s}{2} + \frac{h}{2}\right)^2 \tag{A.2}$$

$$I_{zz}^{\text{blue}} = \frac{h_s(b_s - h_s)^3}{12} + h_s(b_s - h_s)\left(x_s + \frac{h_s}{2}\right)^2 \tag{A.3}$$

$$I_{zz}^{\text{green}} = \frac{h_s^3 d_s}{12} + h_s d_s \left(x_s - \frac{b_s}{2} + \frac{h_s}{2}\right)^2 \tag{A.4}$$

Thus, the moments of inertia of the whole cross section are:

$$I_{xx} = I_{xx}^{\text{blue}} + I_{xx}^{\text{green}} \tag{A.5}$$

$$I_{zz} = I_{zz}^{\text{blue}} + I_{zz}^{\text{green}} \tag{A.6}$$

As described by (CISC, 2002), the Saint-Venant torsional constant, J, is a geometric characteristic of the cross section that quantifies a structural member's resistance to pure or uniform torsion. This constant is essential for determining the buckling moment resistance of beams without lateral support and for assessing the torsional-flexural buckling of compression members, as outlined in CSA Standard S16.1-94 (CSA, 1994).

Similarly, the warping torsional constant, Γ, represents the resistance to nonuniform or warping torsion. It is also crucial for calculating the buckling moment resistance of laterally unsupported beams and the torsional-flexural buckling of compression members, according to CSA Standard S16.1-94 (CSA, 1994). The values for J and Γ are provided by (CISC, 2002):

$$J = \frac{(d_s' + b_s')h_s^3}{3} \tag{A.7}$$

$$\Gamma = \frac{(d_s'^3 + b_s'^3)h_s^3}{36} \tag{A.8}$$

where

$$d_s' = d_s - \frac{h_s}{2} \text{ and } b_s' = b_s - \frac{h_s}{2} \tag{A.9}$$

To calculate the parameters E_y^s and G_{xz}^s for each stiffener, it is necessary to calculate the stiffness matrices of their flanges and perform their weighted averages. For the parameter E_y^s, it was chosen to weight by the moment of inertia, I_{xx}. In the case of G_{xz}^s, it

was weighted by the Saint-Venant torsional constant, J. Since both flanges of the stiffener have stacking oriented with a difference of 90° in relation to the skin laminate, their 0° stacking reference was rotated to match the same reference axis as the skin, as shown in Fig. A.2.
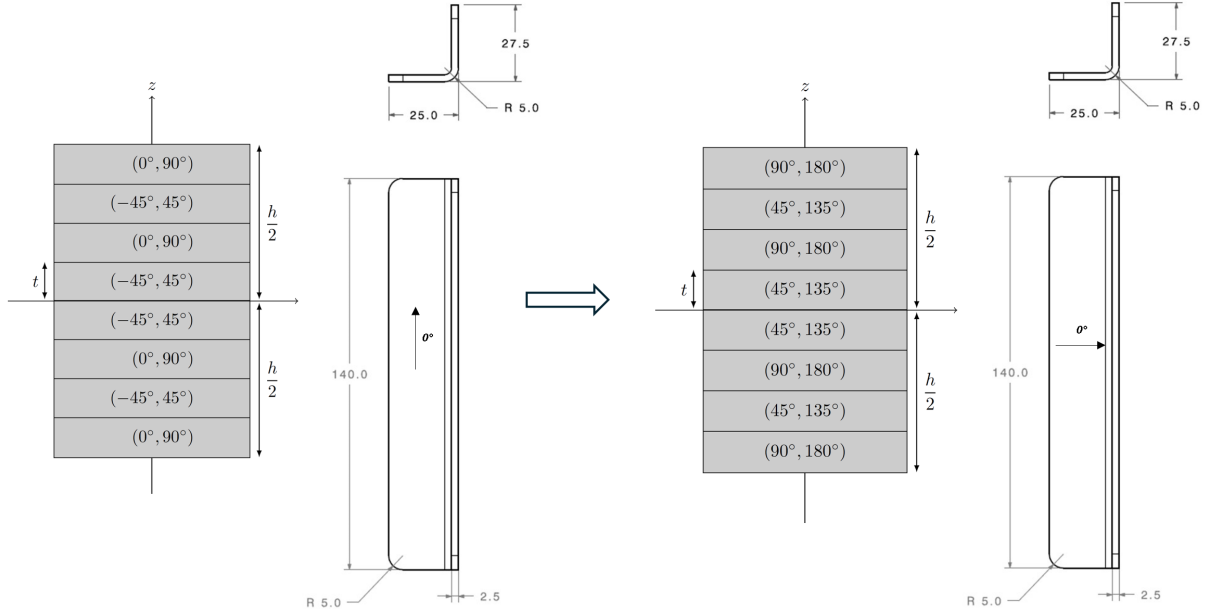

FIGURE A.2 – Representative figure showing the change in reference axes for the quasi-isotropic stacking sequence configuration of the stiffeners.

The constitutive relationship for laminated composite in each flange is:

$$\begin{Bmatrix} \mathbf{N} \\ \mathbf{M} \\ \mathbf{S} \end{Bmatrix} = \begin{bmatrix} \mathbf{A_s} & \mathbf{B_s} & 0 \\ \mathbf{B_s} & \mathbf{D_s} & 0 \\ 0 & 0 & \mathbf{H_s} \end{bmatrix} \begin{Bmatrix} \varepsilon^0 \\ \kappa \\ \gamma \end{Bmatrix} \tag{A.10}$$

One way to obtain the stiffness parameters of each flange is by considering a tensile test with $\mathbf{M} = \mathbf{0}$. Thus, by applying this methodology, the previous equation can be described as:

$$\begin{Bmatrix} \mathbf{N} \\ \mathbf{0} \\ \mathbf{S} \end{Bmatrix} = \begin{bmatrix} \mathbf{A_s} & \mathbf{B_s} & 0 \\ \mathbf{B_s} & \mathbf{D_s} & 0 \\ 0 & 0 & \mathbf{H_s} \end{bmatrix} \begin{Bmatrix} \varepsilon^0 \\ \kappa \\ \gamma \end{Bmatrix} \tag{A.11}$$

From Equation A.11, it is obtained that:

$$(\mathbf{B_s})\varepsilon^0 + \mathbf{D_s}\kappa = \mathbf{0} \Rightarrow \kappa = -(\mathbf{D_s})^{-1}(\mathbf{B_s})\varepsilon^0 \tag{A.12}$$

By applying Equation A.12 to Equation A.11, it is obtained that:

$$\mathbf{N} = \mathbf{A_s}\varepsilon^0 - \mathbf{B_s}(\mathbf{D_s})^{-1}(\mathbf{B_s})\varepsilon^0 = [\mathbf{A_s} - \mathbf{B_s}(\mathbf{D_s})^{-1}(\mathbf{B_s})]\varepsilon^0 \tag{A.13}$$

The value of $\boldsymbol{\sigma}$ can be obtained from Equation A.13, as shown in the Equation below:

$$\boldsymbol{\sigma} = \frac{\mathbf{N}}{h_s} = \frac{1}{h_s}[\mathbf{A_s} - \mathbf{B_s}(\mathbf{D_s})^{-1}(\mathbf{B_s})]\varepsilon^0 \tag{A.14}$$

Thus, the stiffness tensor $\overline{\mathbf{C}}$ can be obtained as shown in the equation below:

$$\boldsymbol{\sigma} = \overline{\mathbf{C}}\varepsilon^0 \Rightarrow \overline{\mathbf{C}} = \frac{1}{h_s}[\mathbf{A_s} - \mathbf{B_s}(\mathbf{D_s})^{-1}(\mathbf{B_s})] \tag{A.15}$$

For a symmetric laminate, it is found that $\mathbf{B_s} = \mathbf{0}$. Thus, the stiffness tensor $\overline{\mathbf{C}}$ can be represented by the following equation:

$$\overline{\mathbf{C}} = \frac{1}{h_s}\mathbf{A_s} \tag{A.16}$$

Therefore, the compliance tensor $\overline{\mathbf{S}}$ can be represented as shown in the equation below.

$$\varepsilon = \overline{\mathbf{S}}\boldsymbol{\sigma} \tag{A.17}$$

where $\overline{\mathbf{S}} = (\overline{\mathbf{C}})^{-1}$.

The stress-strain relationships in terms of engineering constants under plane stress can be represented by the equation below:

$$\begin{Bmatrix} \varepsilon_x \\ \varepsilon_y \\ \gamma_{xy} \end{Bmatrix} = \begin{bmatrix} \frac{1}{\overline{E}_x} & -\frac{\nu_{yx}}{\overline{E}_y} & \frac{\eta_{sx}}{\overline{G}_{xy}} \\ -\frac{\nu_{xy}}{\overline{E}_x} & \frac{1}{\overline{E}_y} & \frac{\eta_{sy}}{\overline{G}_{xy}} \\ \frac{\eta_{xs}}{\overline{E}_x} & \frac{\eta_{ns}}{\overline{E}_y} & \frac{1}{\overline{G}_{xy}} \end{bmatrix} \begin{Bmatrix} \sigma_x \\ \sigma_y \\ \tau_{xy} \end{Bmatrix} \tag{A.18}$$

where

$$\overline{E}_x = \frac{1}{\overline{S}_{11}} \tag{A.19}$$

$$\overline{E}_y = \frac{1}{\overline{S}_{22}} \tag{A.20}$$

$$\overline{G}_{xy} = \frac{1}{\overline{S}_{66}} \tag{A.21}$$

To characterize the transverse shear forces, the following constitutive relation is ap-

plied:

$$\begin{Bmatrix} \tau_{yz} \\ \tau_{xz} \end{Bmatrix} = \frac{1}{h_s} \begin{Bmatrix} S_{yz} \\ S_{xz} \end{Bmatrix} = \frac{1}{h_s} \mathbf{H_s} \begin{Bmatrix} \gamma_{yz} \\ \gamma_{xz} \end{Bmatrix} \tag{A.22}$$

Therefore, the stiffness tensor $\overline{\mathbf{C_t}}$, related to transverse shear forces, can be represented by the following equation:

$$\overline{\mathbf{C_t}} = \frac{1}{h_s} \mathbf{H_s} \tag{A.23}$$

Thus, the compliance tensor $\overline{\mathbf{S_t}}$, related to transverse shear forces, can be represented as shown in the equation below:

$$\boldsymbol{\gamma} = \overline{\mathbf{S_t}} \boldsymbol{\tau} \tag{A.24}$$

where $\overline{\mathbf{S_t}} = (\overline{\mathbf{C}}_t)^{-1}$.

The stress-strain relationships for transverse shear forces, expressed in terms of engineering constants, can be represented by the equation below:

$$\begin{Bmatrix} \gamma_{yz} \\ \gamma_{xz} \end{Bmatrix} = \begin{bmatrix} \frac{1}{\overline{G}_{yz}} & \frac{\eta_{yz,xz}}{\overline{G}_{xz}} \\ \frac{\eta_{xz,yz}}{\overline{G}_{yz}} & \frac{1}{\overline{G}_{xz}} \end{bmatrix} \begin{Bmatrix} \tau_{yz} \\ \tau_{xz} \end{Bmatrix} \tag{A.25}$$

where

$$\overline{G}_{yz} = \frac{1}{\overline{S}_{t_{44}}} \tag{A.26}$$

$$\overline{G}_{xz} = \frac{1}{\overline{S}_{t_{55}}} \tag{A.27}$$

$$\tag{A.28}$$

The effective elastic properties of each stiffener are defined as follows:

$$E_y^s = \frac{\sum_{i=1}^{N_{\text{flange}}} (\overline{E}_y I_{xx})^{\text{flange}_i}}{\sum_{i=1}^{N_{\text{flange}}} (I_{xx})^{\text{flange}_i}} \tag{A.29}$$

$$G_{xz}^s = \frac{\sum_{i=1}^{N_{\text{flange}}} (\overline{G}_{xz} J)^{\text{flange}_i}}{\sum_{i=1}^{N_{\text{flange}}} (J)^{\text{flange}_i}} \tag{A.30}$$

FOLHA DE REGISTRO DO DOCUMENTO

^{1.} CLASSIFICAÇÃO/TIPO DM	^{2.} DATA 11 de julho de 2024	^{3.} DOCUMENTO Nº DCTA/ITA/DM-051/2024	^{4.} Nº DE PÁGINAS 129

^{5.} TÍTULO E SUBTÍTULO:

Buckling analysis of stiffened composite panels with cutouts using the discrete Ritz method

^{6.} AUTOR(ES):

Lucas Garcia de Sampaio Lobianco

^{7.} INSTITUIÇÃO(ÕES)/ÓRGÃO(S) INTERNO(S)/DIVISÃO(ÕES):

Instituto Tecnológico de Aeronáutica – ITA

^{8.} PALAVRAS-CHAVE SUGERIDAS PELO AUTOR:

Composites; Buckling; Prebuckling; Semi-analytical model; Panels with cutouts; Stiffened panel; Discrete Ritz method; Hierarchical polynomials.

^{9.} PALAVRAS-CHAVE RESULTANTES DE INDEXAÇÃO:

Painéis; Placas reforçadas; Materiais compósitos; Flambagem; Método de Rayleigh-Ritz; Método de elementos finitos; Ensaios de materiais; Engenharia de materiais; Engenharia estrutural.

^{10.} APRESENTAÇÃO: **(X) Nacional**   **( ) Internacional**

ITA, São José dos Campos. Curso de Mestrado. Programa de Pós-Graduação em Engenharia Aeronáutica e Mecânica. Área de Projeto Aeronáutico, Estruturas e Sistemas Aeroespaciais. Orientador: Prof. Dr. Maurício Vicente Donadon. Defesa em 28/06/2024. Publicada em 2024.

^{11.} RESUMO:

The idealization of the critical section of a structural component of an aircraft is a strategic approach in aerospace engineering, balancing the need for detailed analysis, addressing particular issues related to the engineering design and improvement on numerical performance of the model. Thus, it is possible to focus efforts on the most crucial aspects of aircraft design, ensuring safety, performance, and efficiency in the final product. In this context, this work presents the development of a semi-analytical model using MATLAB® software and employing the Discrete Ritz Method and the principle of stationary total potential energy to conduct prebuckling analyses and determine the critical buckling load of plates with circular cutouts and stiffeners. A methodology is proposed to minimize the computational effort required by the model. Additionally, with the use of hierarchical polynomials, various edge boundary conditions can be simulated with only one set of integrations. The developed model is validated through comparisons with existing literature, finite element analysis using Abaqus® software, and experimental tests involving the buckling of panels of an aircraft's horizontal stabilizer under pure shear loading conditions, using a picture frame testing jig, as outlined in (SINGER *et al.*, 1998). The numerical and experimental results demonstrate excellent agreement, indicating the robustness and accuracy of the model. The research highlights the efficiency of the proposed method in reducing computational cost while maintaining high precision, making it a valuable tool for analyzing buckling behavior in aerospace, naval, mechanical engineering applications, among others. The findings presented herein suggest that the combination of hierarchical polynomials and numerical integration via Gauss-Legendre quadrature offers significant advantages in terms of computational efficiency and precision. Despite minor discrepancies observed between experimental and numerical correlations, mainly due to variations in clamping conditions and material manufacturing processes, the study provides a comprehensive framework for future research and practical implementation.

^{12.} GRAU DE SIGILO:

    (X) OSTENSIVO   **( ) RESERVADO**   **( ) SECRETO**